EXTENDED KALMAN FILTER BASED MULTI-PURPOSE INERTIAL
SENSOR FIELD CALIBRATION ALGORITHM

A THESIS SUBMITTED TO
THE GRATUATE SCHOOL OF NATURAL AND APPLIED SCIENCES
OF
THE MIDDLE EAST TECHNICAL UNIVERSITY

BY

LİSAN OZAN YAMAN

IN PARTIAL FULFILLMENT OF THE REQUIREMENTS
FOR
THE DEGREE OF MASTER OF SCIENCE
IN
MECHANICAL ENGINEERING

DECEMBER 2017

Approval of the thesis:

EXTENDED KALMAN FILTER BASED MULTI-PURPOSE INERTIAL SENSOR FIELD CALIBRATION ALGORITHM

Submitted by **LİSAN OZAN YAMAN** in partial fulfillment of the requirements for the degree of **Master of Science in Mechanical Engineering Department, Middle East Technical University by,**

Prof. Dr. Gülbin Dural ÜNVER \
Dean, Graduate School of **Natural and Applied Sciences**   _____

Prof. Dr. M. A. Sahir ARIKAN \
Head of the Department, **Mechanical Engineering Dept.**   _____

Assist. Prof. Dr. Kıvanç AZGIN \
Supervisor, **Mechanical Engineering Dept., METU**   _____

Examining Committee Members:

Assoc. Prof. Dr.Yiğit YAZICIOĞLU \
Mechanical Engineering Dept., METU   _____

Assist. Prof. Dr. Kıvanç AZGIN \
Mechanical Engineering Dept., METU   _____

Assist. Prof. Dr. Kerem BAYAR \
Mechanical Engineering Dept., METU   _____

Assist. Prof. Dr. Ali Emre TURGUT \
Mechanical Engineering Dept., METU   _____

Assist. Prof. Dr. Kutluk Bilge ARIKAN \
Mechanical Engineering Dept., TED University   _____

Date: _____

I hereby declare that all information in this document has been obtained and presented in accordance with academic rules and ethical conduct. I also declare that, as required by these rules and conduct, I have fully cited and referenced all material and results that are not original to this work.

Name, Last Name   : LİSAN OZAN YAMAN

Signature   :

ABSTRACT

EXTENDED KALMAN FILTER BASED MULTI-PURPOSE INERTIAL SENSOR FIELD CALIBRATION ALGORITHM

YAMAN, LİSAN OZAN

M.S., Department of Mechanical Engineering

Supervisor: Assist. Prof. Dr. Kıvanç AZGIN

December 2017, 140 pages

The Global Satellite Navigation System (GNSS) is widely adopted for common positioning system due to its precision, cost and effectiveness. Despite its advantages, GNSS receivers are susceptible to signal degradation both intentional cases such as jamming/spoofing and unintentional cases like signal blockage in urban environment due to tall buildings. On the other hand, dead reckoning navigation system such as Inertial Navigation System (INS) is immune to external interferences and it can supply continuous navigation solution. However, the immunity comes with a price of unbounded positioning error growth with time due to mainly the Inertial Measurement Unit (IMU) sensor errors which continuously integrated into INS mechanization process. In order to bound inertial navigation system stand-alone navigation precision below some threshold, commonly GNSS or any other navigation aiding systems can be integrated with INS. Moreover, the IMU sensor errors are the crucial source of INS performance degradation factors and extensive laboratory tests are held by IMU manufacturers to calibrate inertial sensors for various types of application where the precision is critical. Even IMU is calibrated in laboratory environment, inertial sensors commonly have residual error

terms left from calibration process. In mass production inertial sensor facilities such as MEMS products, manufacturers may not calibrate via laboratory processes due to necessary extensive labor and cost. That is, many low cost inertial sensors especially belong to automotive grade IMU, born uncalibrated and suffer from error terms. Therefore, robust algorithms and procedures for calibrating inertial measurement units especially low cost-low grade group of sensors in the field without need of precision laboratory equipments are promising.

In this thesis, the development of integrated navigation algorithm that can be used for multi purpose including inertial sensor field calibration algorithm is carried out. First of all, the fundamental aspects of inertial navigation system, and its integration with GNSS receiver is exploited. The idea of calibrating the inertial sensor without use of extensive laboratory equipment is blended with Extended Kalman Filter (EKF) based INS/GNSS integration filter. Furthermore, for land vehicle navigation purpose Zero Velocity Update (ZUPT) and Non-Holonomic motion Constraints (NHCs) also integrated in the developed algorithm. Single and multi-run simulation studies are carried out together with static and dynamic field tests to show the performance of the integration filter. The dynamic calibration procedure deduced by the simulation study is applied to various MEMS inertial measurement units. The full verification of modular integrated algorithm is studied via land vehicle dynamic tests with sub 100 $ IMU and GPS receiver combination.

Keywords: Inertial sensors, Inertial Measurement Unit, Inertial Navigation System, Global Navigation Satellite System, Kalman filter, Field calibration, Accelerometer, Gyroscope

ÖZ

GENİŞLETİLMİŞ KALMAN FİLTRESİ TABANLI ÇOK AMAÇLI ATALETSEL SENSÖR SAHA KALİBRASYON ALGORİTMASI

YAMAN, LİSAN OZAN

Yüksek Lisans, Makina Mühendisliği Bölümü

Tez Yöneticisi: Assist. Prof. Dr. Kıvanç AZGIN

Aralık 2017, 140 sayfa

Konum belirleme sistemleri arasında performans hassasiyeti, maliyet etkinliği ve verimlilik konularında en yaygın kullanıma sahip sistem Küresel Konumlanma Sistemidir (KKS). Küresel konumlanma sistemi, avantajlarına rağmen şehirlerde yüksek binalar nedeniyle veya bilinçli sinyal karıştırma/sahte sinyal basma gibi etkenlerden dolayı sinyal erişiminin engellenmesi durumları ile karşı karşıyadır. Diğer bir yandan, Ataletsel Navigasyon Sistemi (ANS) gibi gözü kapalı tahmine dayanan konum hesabı yöntemleri küresel konumlama sisteminin aksine dış girişimlerden etkilenmemektedir ve kesintisiz navigasyon çıktıları üretebilmektedir. Fakat, dış etkilere olan duyarsızlık özelliği Ataletsel Ölçüm Birimi (AÖB) sensör hatalarının devamlı ataletsel navigasyon sistemi mekanizasyon sürecine entegre edilmesiyle zaman içerisinde sınırsız konum hatasını beraberinde getirmektedir. Ataletsel navigasyon sistemi saf ataletsel navigasyon çözümünün belirli doğruluk seviyelerinin altında tutabilmek için farklı navigasyon destek sistemleriyle genellikle de küresel konumlama sistemi alıcısı ile entegrasyonu gerçekleştirilir. Ek olarak, ataletsel ölçüm birimi sensör hataları ataletsel navigasyon sistemi performansının azalmasında ki en önemli kaynağı

oluşturmakta olup, performansın önemli olduğu birçok uygulamada ataletsel sensörlerin kalibre edilmesine yönelik olarak ataletsel ölçüm birimi üreticileri tarafından laboratuvar ortamında kapsamlı kalibrasyon testleri gerçekleştirilmektedir. Her ne kadar ataletsel sensörler laboratuvar ortamında kalibre edilselerde, hem kullanılan test prosedüründen hem de kalibre edilen sensör tiplerine bağlı olarak kalibrasyondan artan sensör hataları kalmaktadır. Mikro Elektro Mekanik Sistemler (MEMS) gibi yüksek yoğunlukta sensör seri üretim tesislerinde üreticiler kapsamlı prosedürler ve iş gücü ihtiyacından dolayı laboratuvar kalibrasyonu testleri ve prosedürlerini gerçekleştirmeyebilirler. Bu da özellikle otomotif sınıfı ataletsel sensörleri gibi birçok düşük maliyetli sensörlerin hiçbir kalibrasyon sürecine girmeden yüksek sensör hataları ile üretilmesi ile sonuçlanmaktadır. Bu sebeple, özellikle düşük maliyetli ve düşük performanslı ataletsel sensörler için hassas laboratuvar ekipmanları ve süreçlerine bağımlı olmadan sensörleri sahada kalibre etmeye yönelik gürbüz algoritmalar ile süreçler büyük umut vadetmektedir.

Bu tezde, sahada ataletsel sensör kalibrasyonu özelliğini içerisinde bulunduran ve birden fazla amaca hizmet eden tümleşik navigasyon algoritmasının geliştirilmesine yer verilmiştir. Öncelikle ataletsel navigasyon sisteminin önemli noktaları ve küresel konumlanma sistemi alıcısı ile entegrasyonu gibi konular ele alınmıştır. Kapsamlı laboratuvar ekipmanlarına ihtiyaç duymadan ataletsel sensörleri kalibre etme fikri Genişletilmiş Kalman Filtresi (EKF) yapısı içerisinde ataletsel navigasyon sistemi/küresel konumlama sistemi entegrasyon algoritması ile tümleştirilmiştir. Ayrıca, kara uygulamalarına yönelik olarak Sıfır Hız Algılama (ZUPT) ve uygulama platformu hareket sınırlarının algılanması (NHCs) gibi algoritma tabanlı navigasyon destek bilgileri geliştirilen tümleşik algoritma yapısına entegre edilmiştir. Tümleşik navigasyon algoritmasının performansını test etmek amacıyla simülasyon ortamında tekli ve çoklu simülasyon çalışmaları ile durağan ve hareketli saha testleri gerçekleştirilmiştir. Simülasyon çalışmalarında elde edilen hareketli kalibrasyon süreci MEMS tabanlı çeşitli ataletsel ölçüm birimleri üzerinde test edilmiştir. Modüler mimaride oluşturulan tümleşik algoritma

yapısı, 100 dolar seviyesi altında ataletsel ölçüm birimi ve küresel konumlanma sistemi alıcısı kombinasyonu ile kara uygulamasına yönelik saha testlerinde doğrulanmıştır.

Anahtar kelimeler: Ataletsel sensörler, Ataletsel Ölçüm Birimi, Ataletsel Navigasyon Sistemi, Kalman filtresi, Saha Kalibrasyonu, İvmeölçer, Dönüölçer

To Yasemin...
Nothing else matters

ACKNOWLEDGMENTS

TABLE OF CONTENTS

LIST OF TABLES

LIST OF FIGURES

LIST OF SYMBOLS AND ABBREVIATIONS

Operators

$\dot{r}$, $D(r)$	The time derivative of variable r
$\tilde{r}$	INS indicated quantity of variable r
x	Cross product
$\vec{r}$	Vector r
T	Matrix transpose
$\underline{r}$	3x1 matrix r
$ssm(\underline{r})$	Skew-symmetric form of matrix r
δr	Error of variable r
$\left|r\right|$	Absolute value or magnitude of variable r
$f(r)$	Is function of variable r

Symbols

L	Geodetic latitude
λ	Geodetic longitude
h	Ellipsoid height
R_0	Equatorial radius of ellipsoid
R_p	Polar radius of ellipsoid
f	Flattening of ellipsoid
e	Eccentricity of ellipsoid
Ω_{ie}	Angular rate of the Earth
$\underline{\omega}$	Angular rate vector
C	Direction cosine matrix
R	Rotation matrix or Measurement error covariance matrix
$\underline{r}$	Linear position vector
$\underline{v}$	Linear velocity vector
$\underline{a}$	Linear acceleration vector

$\underline{\alpha}$	Angular acceleration vector
$\underline{f}$	Specific force vector
$\underline{\gamma}$	Gravitational force vector
$\underline{g}$	Total gravity vector
$\underline{\Psi}$	Euler attitude vector
F	System matrix
U	System input matrix
$\underline{b}$	Bias error vector
M	Scale factor and misalignment (cross-coupling) error matrix
$\underline{w}$	System noise vector
G	Acceleration dependent bias error matrix
ρ	Pseudorange
δt	Time offset
H	Measurement design matrix
P	System state covariance matrix
Q_k	System noise covariance matrix
x	X axis
y	Y axis
$\underline{z}$	Measurement vector or Z axis
c	Speed of light
$\underline{\eta}$	Measurement noise vector
σ	Standard deviation
μ	Mean value

Acronyms

2D/3D	Two Dimensional/Three Dimensional
CZM	Conventional Zero Meridian
DCM	Direction Cosine Matrix
DOF	Degree of Freedom

xxiii

DR	Dead (Deduced) Reckoning
ECEF	Earth Centered Earth Fixed
ECI	Earth Centered Inertial
EKF	Extended Kalman Filter
GLONASS	Globalnaya Navigatsionnaya Sputnikovaya Sistema
GM	Gauss Markow
GNSS	Global Navigation Satellite System
GPS	Global Positioning System
HOT	High Order Terms
ICD	Interface Control Document
IMU	Inertial Measurement Unit
INS	Inertial Navigation System
ITRF	International Terrestrial Reference Frame
LC	Loosely Coupled
LOS	Line of Sight
LVN	Land Vehicle Navigation
MEMS	Micro-Electro-Mechanical System
NED	North-East-Down
NG	Non GPS (GNSS) aid modes
NHCs	Non Holonomic Constraints
PVT	Position Velocity Time
RC	Random Constant
PR	Pseudo Range
PRR	Pseudo Range Rate
RW	Random Walk
SPP	Single Point Positioning
TC	Tightly Coupled
WGS	World Geodetic System
ZUPT	Zero Velocity Update

CHAPTER 1

INTRODUCTION

1.1   Background

Navigation is quite an old skill and defined in The Concise Oxford Dictionary [1] as "any of several methods of determination or planning a ship's or aircraft's position and course by geometry, astronomy, radio signals, etc." In the name of positioning and building navigation system, various kinds of technologies are used but two of them are used very commonly. "The first is Inertial Navigation Systems (INS), which are self-contained Dead Reckoning (DR) navigation systems provide dynamic information through direct measurements from an Inertial Measurement Unit (IMU)" [2]. The second is Global Positioning System (GPS), which uses passive ranging radio navigation technique.

Since INS is self-contained system, it has an advantage of being used in any kind of environment without minding external inteferences. Besides that, INS provides continuous position, velocity and attitude information to users by using measurements from three orthogonal placed accelerometers and gyroscopes triads with initial conditions. However, the performance of INS is time dependent and its accuracy is degraded due to IMU sensors deterministic and stochastic errors. In order to endure reasonable accuracy, it is crystal clear to see the necessity of high performance INS. However, high performance INS is quite costly, bigger in size and confronted to government export regulations. Therefore, many researches are based on low cost IMUs to develop accurate navigation system. The most common use is aiding INS with external sources to aid and bound its time dependent characteristics. Satellite navigation system is the most popular way of aiding INS

due to its time-invariant accuracy. Receiver of satellite navigation system requires direct line of sight to satellite to provide navigation solution and thus, signal blockage in urban environment occurs frequently. Besides that, satellite navigation system is susceptible to electromagnetic signals which make it jammed in some tactical uses.

During last few decades, Micro-Electro-Mechanical Systems (MEMS) technology has proven its potential in navigation field. Important advantages of this technology are low cost, small size and mass. Many researchers are exploited those benefits of MEMS IMU on their studies. Due to mass production, inappropriate factory calibration and run to run error variations of MEMS inertial sensors force their users to recalibrate them before using or estimating inertial sensor errors during the system is operational. Recent studies show that field calibration methods are quite beneficial for remedying MEMS IMU sensor errors without worrying about how they are calibrated in factory.

Shin and El-Sheimy (2002) [3] developed a calibration method which can be carried out on field without requiring any laboratory equipment. Since magnitudes of local gravity and the earth rate are nearly constant on an arbitrary location of the earth, those quantities are forming the constraints for what inertial sensors measure. This calibration method can be used for determination of bias, scale factor and cross-coupling errors for an accelerometer triad but due to weak signal characteristics of the earth rotation rate, only biases of gyroscopes can be realistically estimated.

Syed et al. (2007) [4] points out that use of the earth rotation rate as a reference for gyroscope calibration is causing unrealistic scale factor and cross-coupling error estimations. Therefore, he claims that instead of using the earth rotation rate, using single axes turn table aids the calibration of the terms that cannot be estimated with Shin and El-Sheimy's method.

Since the method proposed by Syed requires single axis turn table, it's still not a pure field calibration method that is independent of any precise mechanical devices or costly lab equipment. Fong, Ong and Nee (2008) [5] propose that the gravity vector measurement via calibrated accelerometers must be equal to the computed gravity vector from the orientation integration algorithm which is using gyroscopes angular velocity measurements. It is indicated that the proposed method can be used for determination of scale factor and cross-coupling errors of a gyroscope triad. For short operation time, bias terms of gyroscopes are assumed to be approximately constant and the change is insignificant. Therefore, long static time window is proposed for figuring out bias terms of gyroscope triad and required length of time is found by drawing the Allan variance plot.

Later, Pretto and Grisetti (2014) [6] developed a semi-automatic IMU calibration algorithm that extend the study stated by Skog and Handel (2006) [9] and based on the previous work of Fong, Ong and Nee (2008) [5]. Variance based stationarity detection filter is used in the calibration algorithm to detect static conditions to enable algorithm to gain so called automatic detection ability.

1.2   Research Objective

This study focuses on the enhancement of low cost INS/GNSS integrated navigation system by online calibration of inertial sensor errors. The aim of this study is to develop, analyze and test the multi-purpose moduler integrated navigation algorithm which can be also used for calibrating inertial sensors. Therefore, the major objectives of this research study are as follows;

1. **To develop extended Kalman filter (EKF) based INS/GNSS algorithm.** Complete derivation of inertial navigation system (INS) mechanization equations and EKF based INS/GNSS integration algorithms are carried out. Aforementioned integration algorithm is developed in MATLAB environment.

2. **To extend the developed algorithm to cover motion based navigation aid modes for land vehicle apllications.**

   Mainly for land vehicle navigation (LVN); the non-holonomic constraints (NHCs), and zero velocity update (ZUPT) are considered and implemented in the developed algorithm.

3. **To develop inertial sensors field calibration algorithm and form a blended moduler integrated navigation algorithm.**

   Absolute value of local gravity signal and local gravity vector signals are taken as reference signals to develop inertial sensor field calibration algorithm mode of the blended integration filter. In order to analyze the developed algorithm, single and multi run simulation analysis are carried out to observe the performance of calibration algorithm for two different grade of inertial measurement units.

4. **To implement the whole analysis to field test.**

   Field tests consist of static and dynamic tests are carried out to highlight both the inertial sensor calibration and navigation performance of the blended multi-purpose integration filter. Low cost inertial measurement unit and GPS receiver are used to build hardwares for testing the developed algorithm for land vehicle navigation application. In order to test the effectiveness and accuracy of the field calibration test, positioning accuracy is compared with the map. In addition to the proposed field calibration method, implemented motion based non GNSS aid methods are tested in the field. During the tests, intentional GNSS outages created and the positioning accuracy again is compared with the reference.

1.3   Thesis Outline

This thesis contains seven chapters.

Chapter 2 gives main overview of the inertial navigation systems. The fundamentals of inertial navigation systems are highlighted and discussed, including reference frames, earth shape, and gravity model. After defining aforementioned terms, inertial navigation mechanization equations are derived and provided in details. To develop trajectory generator for pseudo signal generation purpose, inverse mechanization is carried out and provided in appendix as well. Later on, the mechanization equations are perturbed to derive and formulate the error dynamics equations which are later used for system modeling of extended Kalman filter. Finally, inertial sensor error model is introduced which is based on dominant deterministic and stochastic properties.

Chapter 3 provides an overview of global satellite navigation system (GNSS). In this chapter the single point positioning (SPP) via pseudorange and pseudorange rate model is reviewed. Moreover, complementary nature of INS and GNSS are illuminated and needs for integration is discussed as well.

In Chapter 4, the detailed derivation and model of the targetted integration navigation filter is exploited. In other words, the integration algorithm modeling structure and details for inertial sensors field calibration procedure are taken into consideration. First, system model and algorithm working flow is highlighted. Then, the measurement model for INS/GNSS, ZUPT, NHCs, and inertial sensor field calibration aiding modes are detailly discussed. Moreover, stationary detection filter used during the study is covered as well.

In Chapter 5, simulation analysis covering single and multi-runs are carried out for both automotive grade and tactical grade inertial measurement units. Single simulation run is analyzed in detail to observe the convergence of inertial sensor error parameter estimate during the calibration procedure. To form a statistical

results indicating the performance of the calibration algorithm, multi run simulations with gaussian shape distributed inertial sensor errors carried out.

Chapter 6 holds the results of the field tests. The test equipment, logged data, and the trajectories of field is given. The logged IMU and GPS data are post processed and the aforementioned field calibration method is applied. In addition to this, implemented non GNSS aids methods are tested by using the logged data. The accuracy of developed algorithm is compared with reference and the main behaviors of the system are tested in GNSS degraded environment.

Finally, Chapter 7 draws the major conclusions of this study and indicates the recommended topics requiring further analysis.

CHAPTER 2

INERTIAL NAVIGATION

The fundamental operation of inertial navigation systems (INS) govern by the laws of classical mechanics. If the linear acceleration and angular rotation rate of a body are measured, those measurement can be used together with mathematical integration to calculate the change in velocity, position and orientation. What an inertial navigation system does is exactly the same thing indicated above. Inertial navigation systems calculate the position, velocity and attitude of a body in space with respect to some reference system. In other words, inertial navigation system keeps track of a body orientation, its position and velocity via integration of acceleration and angular rate measurements together with initial known conditions. The main component of INS is inertial measurement unit (IMU) which typically consists of three mutually orthogonal placed accelerometers and gyroscopes.

In this chapter, reference frames are introduced first. Then, parameters related to the Earth shape and gravity models are provided. Vector rotation concept is briefly touched and this chapter ends with detailed derivation of mechanization equations and their perturbed error counterparts.

2.1 Reference Frames

In this study, four different reference frames are used and thus introduced here.

The inertial frame (i-frame) "has its origin at the center of the Earth and axes which are non-rotating with respect to the fixed stars with its z-axis parallel to spin axis of the Earth, x-axis pointing towards the mean vernal equinox, and y-axis completing a right-handed orthogonal frame" [11] which is shown in Figure 2.1. The inertial frame is commonly referenced as Earth centered inertial (ECI) frame.
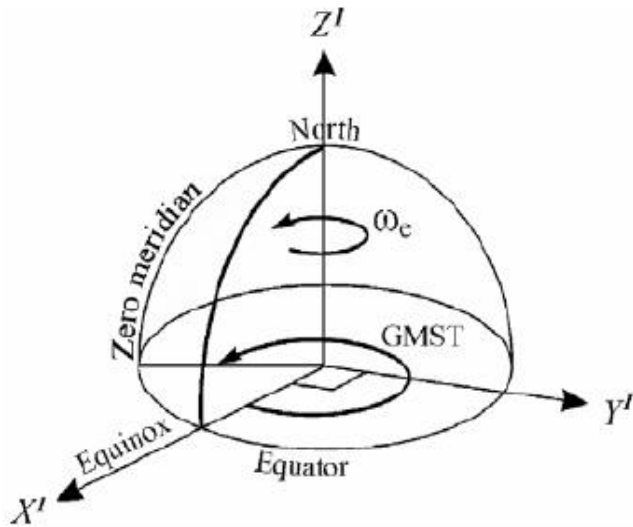
Figure 2.1 The Inertial Frame [(Adopted from [12])]

The Earth frame (e-frame) is originated at the mass center of the Earth and its axes are rotating with the Earth. Z-axis is parallel to spin axis of the Earth like the inertial frame, x-axis points along the intersection of the equator with conventional zero meridian (CZM), and y-axis completing a right-handed orthogonal frame which is shown in Figure 2.2. The Earth frame is commonly referenced as Earth centered Earth fixed (ECEF) frame.
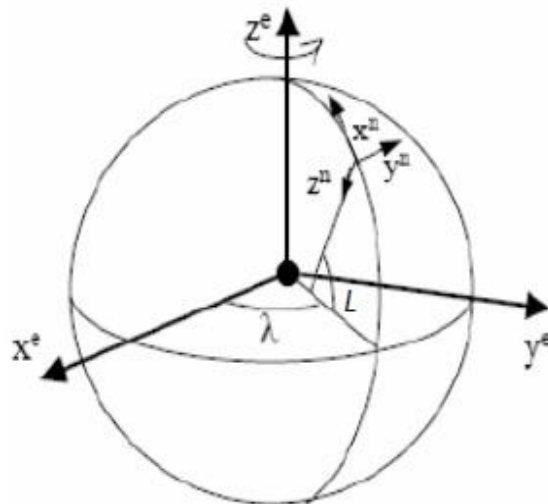
Figure 2.2 The Earth Frame and Navigation Frame [(Adopted from [12])]

The navigation frame (n-frame) is a local geodetic frame and centered in the navigation system origin. North, east and down (NED) is commonly used form of local geodetic frame and it will be used in this study as well. X-axis is toward true north direction which is increasing latitude direction, y-axis is toward east direction which is increasing longitude direction, and z-axis is completing a right-handed orthogonal frame which is shown in Figure 2.2. Throughout this study the navigation frame axes are aligned with the directions of the WGS-84 Earth ellipsoid north, east and down directions. The position of a body is represented with geodetic latitude denoted as $L_{b/e}$, geodetic longitude denoted as $\lambda_{b/e}$, and geodetic height denoted as $h_{b/e}$.

The body frame (b-frame) has its origin which is coincident with the navigation frame. The body frame is also known as vehicle frame and axes are remained fix with the body or vehicle. X-axis is commonly defined in the forward axis of the vehicle, z-axis is defined in the vertical down direction, and y-axis is completing a right-handed orthogonal frame which is shown in Figure 2.3. If the angular rotations are concerned, x-y-z axes of body frame are equivalent to roll-pitch-yaw axes respectively.
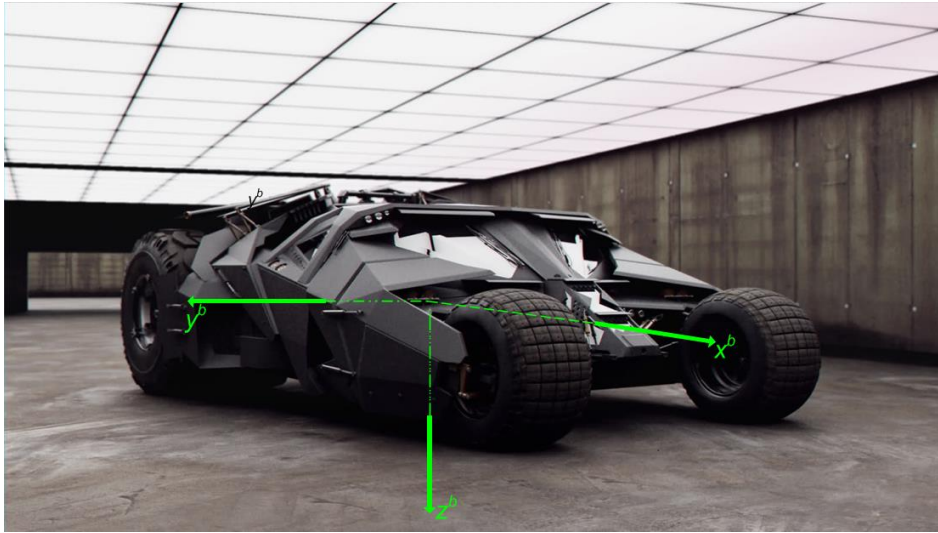
Figure 2.3 The Body Frame ^(Bare figure is taken from [13])

The sensor frame (s-frame) has its origin which is coincident with inertial measurement unit origin that is commonly center point of accelerometer triad. The sensor frame is right-handed orthogonal frame and its schematic view is shown in Figure 2.4. During manufacturing of inertial measurement unit, inertial sensors including accelerometers and gyroscopes cannot exactly aligned with the sensor frame. Inertial sensor calibration procedures generally carried out in laboratory environment to find out the cross-coupling error terms of both accelerometer and gyroscope triad from the sensor frame.
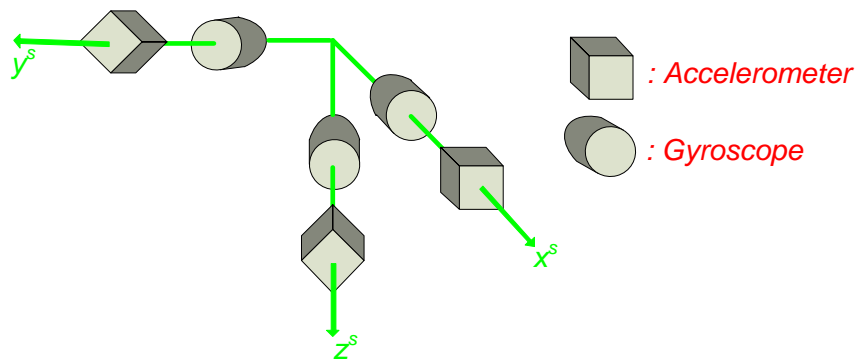
Figure 2.4 The Sensor Frame

2.2 The Earth Ellipsoidal Model

The model that is representing the Earth surface is quite crucial for navigation purpose since the navigation solutions especially position are generally desired relative to the Earth's surface. Therefore, two main standards namely World Geodetic System 1984 (WGS-84) [14] and the international terrestrial reference frame (ITRF) [15] are emerged. Both of those datums are based upon an ellipsoidal model and their origin is located at the center of mass of the Earth.

"The ellipsoid is commonly defined in terms of the equatorial radius and either (primary or major) eccentricity of the ellipsoid, e, or the flattening of the ellipsoid, f." [16]. Figure 2.5 indicates the cross-section of the Earth's surface which is exaggeratedly drawn for better visualization. Definitions of whole parameters shown in Figure 2.5 are well described in [16].
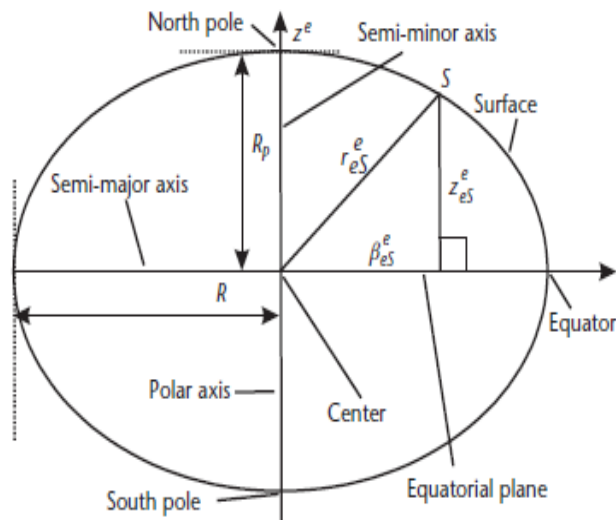
Figure 2.5 Cross-Section of the Earth Ellipsoidal Surface (Adopted from [16])

According to WGS-84, fundamental constants defining the ellipsoid and more are listed in Table 2.1.

Table 2.1 WGS-84 Ellipsoid Constants

Name	Symbol	Value	Units
Equatorial radius	R_0	6378137.0	m
Polar radius	R_P	6356752.3142	m
Flattening	f	1/298.257223563	-
Eccentricity	e	0.0818191908425	-
Angular rate	Ω_{ie}	7.292115 x 10^{-5}	rad/s
Gravitational constant	GM	3.986004418 x 10^{14}	m^3/s^2

For any point on the Earth surface, the meridian radius of curvature is defined as the radius a circle that is osculating in the north-south direction. The transverse radius of curvature is defined as the radius of the prime vertical. The meridian and transverse radii are denoted as R_N and R_E respectively.

$$R_N = \frac{R_0(1-e^2)}{(1-e^2\sin^2(L_{b/e}))^{3/2}} \qquad \text{2-1}$$

$$R_E = \frac{R_0}{\sqrt{1-e^2\sin^2(L_{b/e})}} \qquad \text{2-2}$$

As seen from Figure 2.1, the Earth is rotating around its z-axis with approximately constant angular speed of Ω_{ie}. Using column matrix notation:

$$\underline{\omega}_{e/i}^{(e)} = \begin{bmatrix} 0 \\ 0 \\ \Omega_{ie} \end{bmatrix} \qquad \text{2-3}$$

The Earth rotation rate matrix can be represented in the navigation frame by using the direction cosine matrix (DCM) from the Earth frame to the navigation frame.

$$\underline{\omega}_{e/i}^{(n)} = C_e^n \underline{\omega}_{e/i}^{(e)} \qquad \text{2-4}$$

The detailed derivation and explanations related to vector rotation well presented in the references [16], [17], [18], [19] and [20]

From Figure 2.2, it's clear that the Earth frame can be transformed to the navigation frame by two successive simple rotations. The first one is to rotate the earth frame around its z-axis by the geodetic longitude $\lambda_{b/e}$, then rotate the obtained intermediate frame around its y-axis by $-(\pi/2 + L_{b/e})$.

$$C_n^e = R_3(\lambda_{b/e})R_2(-(\pi/2 + L_{b/e}))$$

2-5

Where

$$R_3(\lambda_{b/e}) = \begin{bmatrix} \cos(\lambda_{b/e}) & -\sin(\lambda_{b/e}) & 0 \\ \sin(\lambda_{b/e}) & \cos(\lambda_{b/e}) & 0 \\ 0 & 0 & 1 \end{bmatrix}$$

2-6

$$R_2(-(\pi/2 + L_{b/e})) = \underbrace{\begin{bmatrix} \cos(-(\pi/2 + L_{b/e})) & 0 & \sin(-(\pi/2 + L_{b/e})) \\ 0 & 1 & 0 \\ -\sin(-(\pi/2 + L_{b/e})) & 0 & \cos(-(\pi/2 + L_{b/e})) \end{bmatrix}}_{\begin{bmatrix} -\sin(L_{b/e}) & 0 & -\cos(L_{b/e}) \\ 0 & 1 & 0 \\ \cos(L_{b/e}) & 0 & -\sin(L_{b/e}) \end{bmatrix}}$$

2-7

Expression (2.5) can be written as:

$$C_n^e = \begin{bmatrix} -\cos(\lambda_{b/e})\sin(L_{b/e}) & -\sin(\lambda_{b/e}) & -\cos(\lambda_{b/e})\cos(L_{b/e}) \\ -\sin(\lambda_{b/e})\sin(L_{b/e}) & \cos(\lambda_{b/e}) & -\sin(\lambda_{b/e})\cos(L_{b/e}) \\ \cos(L_{b/e}) & 0 & -\sin(L_{b/e}) \end{bmatrix}$$

2-8

Since DCM is orthonormal by definition, substitute transpose of expression (2.8) into (2.4).

$$\underline{\omega}_{e/i}^{(n)} = (C_n^e)^T \underline{\omega}_{e/i}^{(e)}$$

2-9

$$\underline{\omega}_{e/i}^{(n)} = \begin{bmatrix} \Omega_{ie}\cos(L_{b/e}) \\ 0 \\ -\Omega_{ie}\sin(L_{b/e}) \end{bmatrix}$$

2-10

The turn rate of the navigation frame with respect to the Earth frame is commonly called as the transport rate in the literature. By using the expression in the references [16], [20] and [21] the skew symmetry matrix form of transport rate is expressed as follow:

$$ssm(\underline{\omega}_{n/e}^{(n)}) = C_e^n \dot{C}_n^e$$

2-11

The rotation matrix can be expressed in an exponential form and expression (2.5) can be written as: [21]

$$C_n^e = e^{ssm(\underline{u_3})\lambda_{b/e}} e^{-ssm(\underline{u_2})(\pi/2 + L_{b/e})}$$

2-12

where $u_i \quad i = 1,2,3$ are unit basis vectors. Time derivative of the above expression is:

$$\dot{C}_n^e = e^{ssm(\underline{u_3})\lambda_{b/e}}\dot{\lambda}_{b/e}ssm(\underline{u_3})e^{-ssm(\underline{u_2})(\pi/2+L_{b/e})} - e^{ssm(\underline{u_3})\lambda_{b/e}}e^{-ssm(\underline{u_2})(\pi/2+L_{b/e})}\dot{L}_{b/e}ssm(\underline{u_2}) \qquad \textbf{2-13}$$

Substitution of (2.13) and transpose of (2.8) into expression (2.11) yields:

$$C_e^n = (C_n^e)^T \Rightarrow\Rightarrow\Rightarrow C_e^n = e^{ssm(\underline{u_2})(\pi/2+L_{b/e})}e^{-ssm(\underline{u_3})\lambda_{b/e}}$$

$$ssm(\underline{\omega_{n/e}^{(n)}}) = e^{ssm(\underline{u_2})(\pi/2+L_{b/e})}\dot{\lambda}_{b/e}ssm(\underline{u_3})e^{-ssm(\underline{u_2})(\pi/2+L_{b/e})} - \dot{L}_{b/e}ssm(\underline{u_2}) \qquad \textbf{2-14}$$

The column matrix form of the expression (2.14) is obtained as:

$$\underline{\omega_{n/e}^{(n)}} = e^{ssm(\underline{u_2})(\pi/2+L_{b/e})}\dot{\lambda}_{b/e}\underline{u_3} - \dot{L}_{b/e}\underline{u_2} \qquad \textbf{2-15}$$

$$\underline{\omega_{n/e}^{(n)}} = \dot{\lambda}_{b/e}(\underbrace{\cos(\pi/2 + L_{b/e})}_{-\sin(L_{b/e})}\underline{u_3} + \underbrace{\sin(\pi/2 + L_{b/e})}_{\cos(L_{b/e})}\underline{u_1}) - \dot{L}_{b/e}\underline{u_2} \qquad \textbf{2-16}$$

$$\underline{\omega_{n/e}^{(n)}} = \begin{bmatrix} \dot{\lambda}_{b/e}\cos(L_{b/e}) \\ -\dot{L}_{b/e} \\ -\dot{\lambda}_{b/e}\sin(L_{b/e}) \end{bmatrix} \qquad \textbf{2-17}$$

As explained earlier, the meridian and the transverse radii are hypothetic osculating circles that are intersecting the Earth surface. The meridian radii can be visualized as the trajectory where the circular motion in the north-south direction takes place. In the same manner, cosine latitude of the transverse radii can be visualized as the similar motion in the east-west direction. respectively. Therefore, the rate of change of geodetic latitude and longitude can be taken into consideration as two circular motions with the radii are mentioned above.

$$\dot{L}_{b/e} = \frac{v_{b/e,N}^{(n)}}{R_N + h_{b/e}} \qquad \textbf{2-18}$$

$$\dot{\lambda}_{b/e} = \frac{v_{b/e,E}^{(n)}}{(R_E + h_{b/e})\cos(L_{b/e})} \qquad \textbf{2-19}$$

$$\dot{h}_{b/e} = -v_{b/e,D}^{(n)} \qquad \textbf{2-20}$$

where $v_{b/e,i}^{(n)}$ $i = N, E, D$ are the velocity components of the body with respect to the Earth frame which is resolved in the navigation frame. N,E,D are abbreviated as north, south and down respectively.

Finally substitute (2.18), (2.19) and (2.20) into expression (2.17) yields:

$$\underline{\omega}_{n/e}^{(n)} = \begin{bmatrix} \dfrac{v_{b/e,E}^{(n)}}{(R_E + h_{b/e})} \\ \dfrac{-v_{b/e,N}^{(n)}}{(R_N + h_{b/e})} \\ \dfrac{-v_{b/e,E}^{(n)} \tan(L_{b/e})}{(R_E + h_{b/e})} \end{bmatrix}$$

2-21

2.3 Inertial Navigation Mechanization Equations

Throughout this study the navigation frame is commonly used for both being the reference frame and the resolution frame. Therefore, mainly the n-frame definitions and derivations of navigation equations are given in the following pages. The inertial frame, the Earth frame, and the Wander-Azimuth frame representations are well presented in [16], [22] and [24]

2.3.1 Attitude Equation

The attitude of a body with respect to any reference frame can be represented by several means including direction cosine matrix, euler angles, quaternion etc. The detailed explanations of mentioned attitude representations are given in the references [16], [25] and [26]. Direction cosine matrix representation is mainly used throughout this study.

Derivative of the coordinate transformation matrix between body and navigation frame can be obtained by using the expression (2.11).

$$\dot{C}_b^n = C_b^n ssm(\underline{\omega}_{b/n}^{(b)})$$

2-22

where $\underline{\omega}_{b/n}^{(b)}$ is matrix form of $\vec{\omega}_{b/n}$ which is angular velocity vector of a body with respect to the navigation frame. $\underline{\omega}_{b/n}^{(b)}$ matrix can be written as follow:

$$\underline{\omega}_{b/n}^{(b)} = \underline{\omega}_{b/i}^{(b)} - \underline{\omega}_{n/e}^{(b)} - \underline{\omega}_{e/i}^{(b)}$$

2-23

Substitute expression (2.23) into (2.22):

$$\dot{C}_b^n = C_b^n ssm(\underline{\omega}_{b/i}^{(b)} - \underline{\omega}_{n/e}^{(b)} - \underline{\omega}_{e/i}^{(b)})$$ 2-24

$$\dot{C}_b^n = C_b^n ssm(\underline{\omega}_{b/i}^{(b)}) - C_b^n ssm(\underline{\omega}_{n/e}^{(b)} + \underline{\omega}_{e/i}^{(b)})\underbrace{C_n^b C_b^n}_{I_{3x3}}$$ 2-25

$$\dot{C}_b^n = C_b^n ssm(\underline{\omega}_{b/i}^{(b)}) - \underbrace{C_b^n ssm(\underline{\omega}_{n/e}^{(b)} + \underline{\omega}_{e/i}^{(b)})C_n^b}_{ssm(\underline{\omega}_{n/e}^{(n)}+\underline{\omega}_{e/i}^{(n)})} C_b^n$$ 2-26

$$\dot{C}_b^n = C_b^n ssm(\underline{\omega}_{b/i}^{(b)}) - ssm(\underline{\omega}_{n/e}^{(n)} + \underline{\omega}_{e/i}^{(n)})C_b^n$$ 2-27

where $\underline{\omega}_{b/i}^{(b)}$ is representing the gyroscope triad readings, $\underline{\omega}_{e/i}^{(n)}$ and $\underline{\omega}_{n/e}^{(n)}$ are given in expressions (2.10) and (2.21) respectively.

According to [16], the expression (2.27) can be integrated with truncating the power series expansion of the exponential terms to first order as follows.

$$C_b^n(t+dt) = C_b^n(t)(I_3 + ssm(\underline{\omega}_{b/i}^{(b)})dt) - ssm(\underline{\omega}_{n/e}^{(n)}(t) + \underline{\omega}_{e/i}^{(n)}(t))C_b^n(t)dt$$ 2-28

2.3.2 Velocity and Position Equations

Any point on the Earth can be represented by a position vector $\vec{r}_{b/e}$ which is originated at the Earth center. The rate of change of position of any point in terms of latitude, longitude and height above ellipsoid surface is given in the expression (2.18), (2.19) and (2.20) respectively. For deducing the velocity equation, the inertial frame derivative of the position vector can be formulated via Coriolis theorem as follow:

$$D_i \vec{r}_{b/e} = D_e \vec{r}_{b/e} + \vec{\omega}_{e/i} \times \vec{r}_{b/e}$$ 2-29

Taking the second derivative of the above equation yields:

$$D_i(D_i\vec{r}_{b/e}) = D_e(D_i\vec{r}_{b/e}) + \vec{\omega}_{e/i} \times (D_i\vec{r}_{b/e})$$ 2-30

$$D_i^2\vec{r}_{b/e} = D_e(D_e\vec{r}_{b/e} + \vec{\omega}_{e/i} \times \vec{r}_{b/e}) + \vec{\omega}_{e/i} \times (D_e\vec{r}_{b/e} + \vec{\omega}_{e/i} \times \vec{r}_{b/e})$$ 2-31

$$D_i^2\vec{r}_{b/e} = D_e^2\vec{r}_{b/e} + \vec{\alpha}_{e/i} \times \vec{r}_{b/e} + \vec{\omega}_{e/i} \times D_e\vec{r}_{b/e} + \vec{\omega}_{e/i} \times D_e\vec{r}_{b/e} + \vec{\omega}_{e/i} \times \vec{\omega}_{e/i} \times \vec{r}_{b/e})$$ 2-32

The Earth rotation rate vector $\vec{\omega}_{e/i}$ is approximately constant, and thus the rate of change of the Earth rotation rate $\vec{\alpha}_{e/i}$ is assumed negligible. Therefore, the equation (2.32) becomes:

16

$$\vec{\alpha}_{e/i} \approx \vec{0}$$

$$D_i^2 \vec{r}_{b/e} = D_e^2 \vec{r}_{b/e} + \underbrace{2\vec{\omega}_{e/i} \times D_e \vec{r}_{b/e}}_{Coriolis\,Acceleration} + \underbrace{\vec{\omega}_{e/i} \times \vec{\omega}_{e/i} \times \vec{r}_{b/e}}_{Centrifugal\,Acceleration})$$ 2-33

Resolve the above expression in ECEF reference frame:

$$D_i^2 \underline{r}_{b/e}^{(e)} = \underbrace{D_e^2 \underline{r}_{b/e}^{(e)}}_{\ddot{r}_{b/e}^{(e)}} + 2ssm(\underline{\omega}_{e/i}^{(e)}) \underbrace{D_e \underline{r}_{b/e}^{(e)}}_{\dot{r}_{b/e}^{(e)}} + ssm(\underline{\omega}_{e/i}^{(e)})^2 \underline{r}_{b/e}^{(e)})$$ 2-34

$$D_i^2 \underline{r}_{b/e}^{(e)} = \ddot{r}_{b/e}^{(e)} + 2ssm(\underline{\omega}_{e/i}^{(e)}) \dot{r}_{b/e}^{(e)} + ssm(\underline{\omega}_{e/i}^{(e)})^2 \underline{r}_{b/e}^{(e)})$$ 2-35

For ease of convenience and sustaining readability, the following notation changes are made.

$$D_i^2 \underline{r}_{b/e}^{(e)} = \underline{a}_{b/i}^{(e)}$$

$$\dot{r}_{b/e}^{(e)} = \underline{v}_{b/e}^{(e)}$$

$$\ddot{r}_{b/e}^{(e)} = \underline{a}_{b/e}^{(e)}$$

To relate the expression (2.35) to accelerometers reading, it is necessary to point out what an accelerometer measures. The answer is straightforwardly a specific force. Specific force is a non-gravitational force sensed with respect to inertial frame and it is actually the force what people and accelerometers sense. Therefore, specific force $\vec{f}_{b/i}$ is:

$$\vec{f}_{b/i} = \vec{a}_{b/i} - \vec{\gamma}_b$$ 2-36

where $\vec{\gamma}_b$ is the acceleration due to gravitational force which does not involve any centripetal term. The gravitational acceleration can be decomposed as:

$$\vec{\gamma}_b = \vec{g}_b + \vec{\omega}_{e/i} \times \vec{\omega}_{e/i} \times \vec{r}_{b/e}$$ 2-37

In this case, $\vec{g}_b$ is the well-known total gravity and it consists of both centrifugal component and the gravitational component. Now, substitute the specific force and the gravity into the expression (2.35):

$$\underline{a}_{b/i}^{(e)} = \underline{a}_{b/e}^{(e)} + 2ssm(\underline{\omega}_{e/i}^{(e)}) \underline{v}_{b/e}^{(e)} + ssm(\underline{\omega}_{e/i}^{(e)})^2 \underline{r}_{b/e}^{(e)})$$ 2-38

$$\underline{a}_{b/e}^{(e)} = \underline{f}_{b/i}^{(e)} + \underbrace{\underline{g}_b^{(e)} + ssm(\underline{\omega}_{e/i}^{(e)})^2 \underline{r}_{b/e}^{(e)}}_{\gamma_b^{(e)}} - 2ssm(\underline{\omega}_{e/i}^{(e)}) \underline{v}_{b/e}^{(e)} - ssm(\underline{\omega}_{e/i}^{(e)})^2 \underline{r}_{b/e}^{(e)})$$ 2-39

$$\underline{a}_{b/e}^{(e)} = \underline{f}_{b/i}^{(e)} + \underline{g}_b^{(e)} - 2ssm(\underline{\omega}_{e/i}^{(e)}) \underline{v}_{b/e}^{(e)}$$ 2-40

In order to obtain the navigation frame resolution of the linear acceleration term, the transformation matrix from the Earth frame to the navigation frame can be used.

$$\underline{v}_{b/e}^{(n)} = C_e^n \underline{v}_{b/e}^{(e)} \qquad \text{2-41}$$

The time derivative of the above expression:

$$\underline{a}_{b/e}^{(n)} = \dot{C}_e^n \underline{v}_{b/e}^{(e)} + C_e^n \underline{a}_{b/e}^{(e)} \qquad \text{2-42}$$

The expression (2.11) can be written as:

$$\dot{C}_e^n = ssm(\underline{\omega}_{e/n}^{(n)})C_e^n \qquad \text{2-43}$$

Substitute (2.43) and (2.38) into (2.42) yields:

$$\underline{a}_{b/e}^{(n)} = ssm(\underline{\omega}_{e/n}^{(n)})C_e^n \underline{v}_{b/e}^{(e)} + C_e^n \{\underline{a}_{b/i}^{(e)} - 2ssm(\underline{\omega}_{e/i}^{(e)})\underline{v}_{b/e}^{(e)} - ssm(\underline{\omega}_{e/i}^{(e)})^2 \underline{r}_{b/e}^{(e)}\} \qquad \text{2-44}$$

$$\underline{a}_{b/e}^{(n)} = \underbrace{ssm(\underline{\omega}_{e/n}^{(n)})}_{-ssm(\underline{\omega}_{n/e}^{(n)})}\underline{v}_{b/e}^{(n)} + \underline{a}_{b/i}^{(n)} - 2C_e^n ssm(\underline{\omega}_{e/i}^{(e)})\underbrace{C_n^e C_e^n}_{I_{3x3}}\underline{v}_{b/e}^{(e)} \cdots$$

$$- C_e^n ssm(\underline{\omega}_{e/i}^{(e)})\underbrace{C_n^e C_e^n}_{I_{3x3}} ssm(\underline{\omega}_{e/i}^{(e)})\underbrace{C_n^e C_e^n}_{I_{3x3}}\underline{r}_{b/e}^{(e)} \qquad \text{2-45}$$

$$\underline{a}_{b/e}^{(n)} = -ssm(\underline{\omega}_{n/e}^{(n)})\underline{v}_{b/e}^{(n)} + \underline{a}_{b/i}^{(n)} - 2\underbrace{C_e^n ssm(\underline{\omega}_{e/i}^{(e)})C_n^e}_{ssm(\underline{\omega}_{e/i}^{(n)})}\underbrace{C_e^n \underline{v}_{b/e}^{(e)}}_{\underline{v}_{b/e}^{(n)}} \cdots$$

$$- \underbrace{C_e^n ssm(\underline{\omega}_{e/i}^{(e)})C_n^e}_{ssm(\underline{\omega}_{e/i}^{(n)})}\underbrace{C_e^n ssm(\underline{\omega}_{e/i}^{(e)})C_n^e}_{ssm(\underline{\omega}_{e/i}^{(n)})}\underbrace{C_e^n \underline{r}_{b/e}^{(e)}}_{\underline{r}_{b/e}^{(n)}} \qquad \text{2-46}$$

$$\underline{a}_{b/e}^{(n)} = -ssm(\underline{\omega}_{n/e}^{(n)})\underline{v}_{b/e}^{(n)} + \{\underline{f}_{b/i}^{(n)} + \underline{g}_b^{(n)} + ssm(\underline{\omega}_{e/i}^{(n)})ssm(\underline{\omega}_{e/i}^{(n)})\underline{r}_{b/e}^{(n)}\} \cdots$$

$$- 2ssm(\underline{\omega}_{e/i}^{(n)})\underline{v}_{b/e}^{(n)} - ssm(\underline{\omega}_{e/i}^{(n)})ssm(\underline{\omega}_{e/i}^{(n)})\underline{r}_{b/e}^{(n)} \qquad \text{2-47}$$

$$\underline{a}_{b/e}^{(n)} = \underline{f}_{b/i}^{(n)} + \underline{g}_b^{(n)} - \{ssm(\underline{\omega}_{n/e}^{(n)}) + 2ssm(\underline{\omega}_{e/i}^{(n)})\}\underline{v}_{b/e}^{(n)} \qquad \text{2-48}$$

The expression (2.48) can be integrated as follows.

$$\underline{v}_{b/e}^{(n)}(t+dt) = \underline{v}_{b/e}^{(n)}(t) + (\underline{f}_{b/i}^{(n)} + \underline{g}_b^{(n)}(t) - \{ssm(\underline{\omega}_{n/e}^{(n)}(t)) + 2ssm(\underline{\omega}_{e/i}^{(n)}(t))\}\underline{v}_{b/e}^{(n)}(t))dt \qquad \text{2-49}$$

For especially low dynamic applications, the position update shown below can be done via integrating the expressions (2.18), (2.19) and (2.20) respectively.

$$L_{b/e}(t+dt) = L_{b/e}(t) + \frac{dt}{2}\left(\frac{v_{b/e,N}^n(t) + v_{b/e,N}^n(t+dt)}{R_N(t) + h_{b/e}(t)}\right) \qquad \text{2-50}$$

$$\lambda_{b/e}(t+dt) = \lambda_{b/e}(t) + \frac{dt}{2}\left(\frac{v_{b/e,E}^n(t) + v_{b/e,E}^n(t+dt)}{(R_E(t) + h_{b/e}(t))\cos(L_{b/e}(t))}\right) \qquad \text{2-51}$$

$$h_{b/e}(t+dt) = h_{b/e}(t) - \frac{dt}{2}\left(v_{b/e,D}^n(t) + v_{b/e,D}^n(t+dt)\right) \qquad \text{2-52}$$

The flow chart of navigation frame mechanization is shown in the following figure.
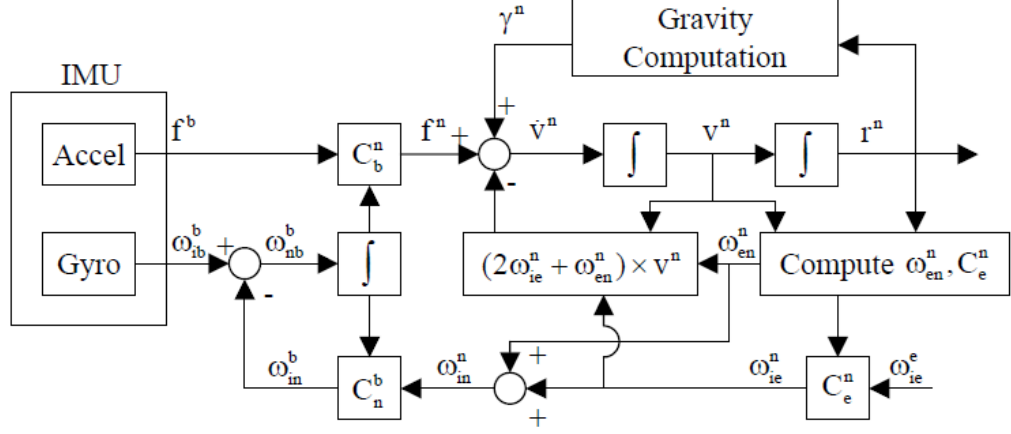
Figure 2.6 Navigation Frame Mechanization (Adopted from [11])

2.4   Inertial Navigation System Error Dynamics

The mechanization equations derived in expressions (2.18), (2.19), (2.20), (2.27), (2.48) basically utilize inertial data with the supplied initial conditions to obtain navigation solutions. Thus, only the mechanization does not imply any information related the error of the deduced solutions. In order to analyze the error feature of the method used, the perturbation analysis should be carried out. The perturbation of position, velocity and any other vector can be expressed as

Error = INS indicated quantity - True Counter Part

$$\delta r_{b/e}^{(n)} = \tilde{r}_{b/e}^{(n)} - r_{b/e}^{(n)}$$

2-53

Three components of the curvilinear position error are

$$\delta L_{b/e} = \tilde{L}_{b/e} - L_{b/e}$$

2-54

$$\delta \lambda_{b/e} = \tilde{\lambda}_{b/e} - \lambda_{b/e}$$

2-55

$$\delta h_{b/e} = \tilde{h}_{b/e} - h_{b/e}$$

2-56

The velocity and inertial data errors are

$$\delta v_{b/e}^{(n)} = \tilde{v}_{b/e}^{(n)} - v_{b/e}^{(n)}$$

2-57

$$\delta \underline{f}_{b/i}^{(i)} = \underline{\tilde{f}}_{b/i}^{(i)} - \underline{f}_{b/i}^{(i)} \qquad \text{2-58}$$

$$\underline{\delta \omega}_{b/i}^{(i)} = \underline{\tilde{\omega}}_{b/i}^{(i)} - \underline{\omega}_{b/i}^{(i)} \qquad \text{2-59}$$

Error in the coordinate transformation matrix can be defined as follow [16]

$$\delta C_b^{n,(n)} = \tilde{C}_b^n C_n^b \qquad \text{2-60}$$

2.4.1 Attitude Error

The coordinate transformation matrix between body and navigation frame can be written in terms of 3-2-1 Euler angles sequence as follow

$$C_b^n = R_3(\psi_{b/n}) R_2(\theta_{b/n}) R_1(\phi_{b/n}) \qquad \text{2-61}$$

$$C_b^n = \begin{bmatrix} \cos(\psi_{b/n}) & -\sin(\psi_{b/n}) & 0 \\ \sin(\psi_{b/n}) & \cos(\psi_{b/n}) & 0 \\ 0 & 0 & 1 \end{bmatrix} \begin{bmatrix} \cos(\theta_{b/n}) & 0 & \sin(\theta_{b/n}) \\ 0 & 1 & 0 \\ -\sin(\theta_{b/n}) & 0 & \cos(\theta_{b/n}) \end{bmatrix} \begin{bmatrix} 1 & 0 & 0 \\ 0 & \cos(\phi_{b/n}) & -\sin(\phi_{b/n}) \\ 0 & \sin(\phi_{b/n}) & \cos(\phi_{b/n}) \end{bmatrix} \qquad \text{2-62}$$

$$C_b^n = \begin{bmatrix} \cos(\psi_{b/n})\cos(\theta_{b/n}) & -\sin(\psi_{b/n})\cos(\phi_{b/n}) + \sin(\phi_{b/n})\cos(\psi_{b/n})\sin(\theta_{b/n}) \\ \cos(\theta_{b/n})\sin(\psi_{b/n}) & \cos(\psi_{b/n})\cos(\phi_{b/n}) + \sin(\psi_{b/n})\sin(\theta_{b/n})\sin(\phi_{b/n}) & \dots \\ -\sin(\theta_{b/n}) & \cos(\theta_{b/n})\sin(\phi_{b/n}) \end{bmatrix}$$

$$\begin{bmatrix} \sin(\psi_{b/n})\sin(\phi_{b/n}) + \cos(\phi_{b/n})\cos(\psi_{b/n})\sin(\theta_{b/n}) \\ \dots \quad -\cos(\psi_{b/n})\sin(\phi_{b/n}) + \sin(\psi_{b/n})\sin(\theta_{b/n})\cos(\phi_{b/n}) \\ \cos(\theta_{b/n})\cos(\phi_{b/n}) \end{bmatrix} \qquad \text{2-63}$$

For small angles

$$\underset{\substack{\sin(\delta x) \approx \delta x \\ \cos(\delta x) \approx 0}}{\overset{Small\,angle\,assumption}{\Rightarrow \Rightarrow \Rightarrow \Rightarrow \Rightarrow}} \quad \delta C_b^{n,(n)} = \begin{bmatrix} 1 & -\delta\psi_{b/n} & \delta\theta_{b/n} \\ \delta\psi_{b/n} & 1 & -\delta\phi_{b/n} \\ -\delta\theta_{b/n} & \delta\phi_{b/n} & 1 \end{bmatrix} \qquad \text{2-64}$$

$$\delta C_b^{n,(n)} = I_{3x3} + ssm(\underline{\delta \Psi}_{b/n}^{(n)}) \qquad \text{2-65}$$

Where $\underline{\delta \Psi}_{b/n}^{(n)} = \begin{bmatrix} \delta\psi_{b/n} \\ \delta\theta_{b/n} \\ \delta\phi_{b/n} \end{bmatrix}$

Taking time derivative of the expression (2.60)

$$\delta \dot{C}_b^{n,(n)} = \dot{\tilde{C}}_b^n C_n^b + \tilde{C}_b^n \dot{C}_n^b \qquad \text{2-66}$$

20

First differentiate the expression (2.65), and then substitute with expression (2.22) into (2.66) yields

$$ssm(\delta\dot{\underline{\Psi}}_{b/n}^{(n)}) = \tilde{C}_b^n \{\underbrace{ssm(\tilde{\underline{\omega}}_{b/n}^{(b)}) - ssm(\underline{\omega}_{b/n}^{(b)})}_{ssm(\delta\underline{\omega}_{b/n}^{(b)})}\}C_n^b \qquad \textbf{2-67}$$

$$ssm(\delta\underline{\omega}_{b/n}^{(b)}) = \{I_{3x3} - ssm(\delta\underline{\Psi}_{b/n}^{(n)})\}C_n^b ssm(\delta\dot{\underline{\Psi}}_{b/n}^{(n)})C_b^n \qquad \textbf{2-68}$$

$$ssm(\delta\underline{\omega}_{b/n}^{(b)}) = C_n^b ssm(\delta\dot{\underline{\Psi}}_{b/n}^{(n)})C_b^n - \underbrace{ssm(\delta\underline{\Psi}_{b/n}^{(n)})C_n^b ssm(\delta\dot{\underline{\Psi}}_{b/n}^{(n)})C_b^n}_{\approx 0 \,(multiplication\,of\,error\,terms)} \qquad \textbf{2-69}$$

$$ssm(\delta\dot{\underline{\Psi}}_{b/n}^{(n)}) = C_b^n ssm(\delta\underline{\omega}_{b/n}^{(b)})C_n^b \qquad \textbf{2-70}$$

$$\delta\dot{\underline{\Psi}}_{b/n}^{(n)} = C_b^n \delta\underline{\omega}_{b/n}^{(b)} \qquad \textbf{2-71}$$

Substitute the expression (2.23) into (2.71)

$$\delta\dot{\underline{\Psi}}_{b/n}^{(n)} = C_b^n \delta\underline{\omega}_{b/i}^{(b)} - C_b^n \delta\underline{\omega}_{e/i}^{(b)} - C_b^n \delta\underline{\omega}_{n/e}^{(b)}$$
$$\Rightarrow\Rightarrow\Rightarrow \delta\dot{\underline{\Psi}}_{b/n}^{(n)} = C_b^n \delta\underline{\omega}_{b/i}^{(b)} - C_b^n (\tilde{\underline{\omega}}_{e/i}^{(b)} - \underline{\omega}_{e/i}^{(b)}) - C_b^n (\tilde{\underline{\omega}}_{n/e}^{(b)} - \underline{\omega}_{n/e}^{(b)}) \qquad \textbf{2-72}$$

$$\delta\dot{\underline{\Psi}}_{b/n}^{(n)} = C_b^n \delta\underline{\omega}_{b/i}^{(b)} - \{C_b^n(\tilde{C}_n^b \tilde{\underline{\omega}}_{e/i}^{(n)} - C_n^b \underline{\omega}_{e/i}^{(n)}) + C_b^n(\tilde{C}_n^b \tilde{\underline{\omega}}_{n/e}^{(n)} - C_n^b \underline{\omega}_{n/e}^{(n)})\} \qquad \textbf{2-73}$$

Use the expression (2.60)

$$\delta\dot{\underline{\Psi}}_{b/n}^{(n)} = C_b^n \delta\underline{\omega}_{b/i}^{(b)} - \{C_b^n(\delta C_n^{b,(b)} C_n^b \tilde{\underline{\omega}}_{e/i}^{(n)} - C_n^b \underline{\omega}_{e/i}^{(n)}) \cdots$$
$$+ C_b^n(\delta C_n^{b,(b)} C_n^b \tilde{\underline{\omega}}_{n/e}^{(n)} - C_n^b \underline{\omega}_{n/e}^{(n)})\} \qquad \textbf{2-74}$$

Use the expression (2.65)

$$\delta\dot{\underline{\Psi}}_{b/n}^{(n)} = C_b^n \delta\underline{\omega}_{b/i}^{(b)} - \{C_b^n((I_{3x3} - ssm(\delta\underline{\Psi}_{b/n}^{(b)}))C_n^b \tilde{\underline{\omega}}_{e/i}^{(n)} - C_n^b \underline{\omega}_{e/i}^{(n)}) \cdots$$
$$+ C_b^n((I_{3x3} - ssm(\delta\underline{\Psi}_{b/n}^{(b)}))C_n^b \tilde{\underline{\omega}}_{n/e}^{(n)} - C_n^b \underline{\omega}_{n/e}^{(n)})\} \qquad \textbf{2-75}$$

$$\delta\dot{\underline{\Psi}}_{b/n}^{(n)} = C_b^n \delta\underline{\omega}_{b/i}^{(b)} - (\tilde{\underline{\omega}}_{e/i}^{(n)} - \underline{\omega}_{e/i}^{(n)}) + C_b^n ssm(\delta\underline{\Psi}_{b/n}^{(b)})C_n^b \tilde{\underline{\omega}}_{e/i}^{(n)} - (\tilde{\underline{\omega}}_{n/e}^{(n)} - \underline{\omega}_{n/e}^{(n)}) \cdots$$
$$+ C_b^n ssm(\delta\underline{\Psi}_{b/n}^{(b)})C_n^b \tilde{\underline{\omega}}_{n/e}^{(n)} \qquad \textbf{2-76}$$

$$\delta\dot{\underline{\Psi}}_{b/n}^{(n)} = C_b^n \delta\underline{\omega}_{b/i}^{(b)} - (\tilde{\underline{\omega}}_{e/i}^{(n)} - \underline{\omega}_{e/i}^{(n)}) - (\tilde{\underline{\omega}}_{n/e}^{(n)} - \underline{\omega}_{n/e}^{(n)}) + \underbrace{ssm(\delta\underline{\Psi}_{b/n}^{(n)})\underbrace{(\tilde{\underline{\omega}}_{e/i}^{(n)} + \tilde{\underline{\omega}}_{n/e}^{(n)})}_{\tilde{\underline{\omega}}_{n/i}^{(n)}}}_{-ssm(\tilde{\underline{\omega}}_{n/i}^{(n)})\delta\underline{\Psi}_{b/n}^{(n)}} \qquad \textbf{2-77}$$

Neglecting multiplication of error terms

$$\delta\dot{\underline{\Psi}}_{b/n}^{(n)} = C_b^n \delta\underline{\omega}_{b/i}^{(b)} - (\tilde{\underline{\omega}}_{e/i}^{(n)} - \underline{\omega}_{e/i}^{(n)}) - (\tilde{\underline{\omega}}_{n/e}^{(n)} - \underline{\omega}_{n/e}^{(n)}) - ssm(\underline{\omega}_{n/i}^{(n)})\delta\underline{\Psi}_{b/n}^{(n)} \qquad \textbf{2-78}$$

where

21

$$\underline{\widetilde{\omega}}_{e/i}^{(n)} - \underline{\omega}_{e/i}^{(n)} = \begin{bmatrix} \Omega_{e/i}\cos(\widetilde{L}_{b/e}) \\ 0 \\ -\Omega_{e/i}\sin(\widetilde{L}_{b/e}) \end{bmatrix} - \begin{bmatrix} \Omega_{e/i}\cos(L_{b/e}) \\ 0 \\ -\Omega_{e/i}\sin(L_{b/e}) \end{bmatrix}$$ **2-79**

The above expression can be represented as the first order taylor approximation as follow

$$e.g : \delta x = \widetilde{x} - x$$
$$\widetilde{x} = x + \delta x \Rightarrow\Rightarrow\Rightarrow f(\widetilde{x}) = f(x + \delta x) \Rightarrow\Rightarrow\Rightarrow f(\widetilde{x}) = f(x) + f'(x)\delta x$$ **2-80**

The expression (2.79) becomes

$$\underline{\widetilde{\omega}}_{e/i}^{(n)} - \underline{\omega}_{e/i}^{(n)} = -\Omega_{e/i}\begin{bmatrix} \sin(L_{b/e}) \\ 0 \\ \cos(L_{b/e}) \end{bmatrix}\delta L_{b/e}$$ **2-81**

And

$$\underline{\widetilde{\omega}}_{n/e}^{(n)} - \underline{\omega}_{n/e}^{(n)} = \begin{bmatrix} \dfrac{\widetilde{v}_{b/e,E}^{(n)}}{(\widetilde{R}_E + \widetilde{h}_{b/e})} \\ \dfrac{-\widetilde{v}_{b/e,N}^{(n)}}{(\widetilde{R}_N + \widetilde{h}_{b/e})} \\ \dfrac{-\widetilde{v}_{b/e,E}^{(n)}\tan(\widetilde{L}_{b/e})}{(\widetilde{R}_E + \widetilde{h}_{b/e})} \end{bmatrix} - \begin{bmatrix} \dfrac{v_{b/e,E}^{(n)}}{(R_E + h_{b/e})} \\ \dfrac{-v_{b/e,N}^{(n)}}{(R_N + h_{b/e})} \\ \dfrac{-v_{b/e,E}^{(n)}\tan(L_{b/e})}{(R_E + h_{b/e})} \end{bmatrix}$$ **2-82**

Variation of R_E and R_N due to latitude error is weak. Therefore their variations can be neglected.

$$\underline{\widetilde{\omega}}_{n/e}^{(n)} - \underline{\omega}_{n/e}^{(n)} = \begin{bmatrix} \dfrac{\delta v_{b/e,E}^{(n)}}{(R_E + h_{b/e})} \\ \dfrac{-\delta v_{b/e,N}^{(n)}}{(R_N + h_{b/e})} \\ \dfrac{-\delta v_{b/e,E}^{(n)}\tan(L_{b/e})}{(R_E + h_{b/e})} \end{bmatrix} - \begin{bmatrix} 0 \\ 0 \\ \dfrac{v_{b/e,E}^{(n)}}{(R_E + h_{b/e})\cos^2(L_{b/e})} \end{bmatrix}\delta L_{b/e} \cdots$$

$$+ \begin{bmatrix} \dfrac{-v_{b/e,E}^{(n)}}{(R_E + h_{b/e})^2} \\ \dfrac{v_{b/e,N}^{(n)}}{(R_N + h_{b/e})^2} \\ \dfrac{v_{b/e,E}^{(n)}\tan(L_{b/e})}{(R_E + h_{b/e})^2} \end{bmatrix}\delta h_{b/e}$$ **2-83**

2.4.2 Velocity Error

Perturbing the derived velocity mechanization equation (2.48) yields

$$\dot{\tilde{v}}_{b/e}^{(n)} - \dot{v}_{b/e}^{(n)} = (\underline{\tilde{f}}_{b/i}^{(n)} - \underline{f}_{b/i}^{(n)}) + (\underline{\tilde{g}}_{b}^{(n)} - \underline{g}_{b}^{(n)}) \cdots$$
$$- \{(ssm(\underline{\tilde{\omega}}_{n/e}^{(n)}) + 2ssm(\underline{\tilde{\omega}}_{e/i}^{(n)}))\tilde{v}_{b/e}^{(n)} - (ssm(\underline{\omega}_{n/e}^{(n)}) + 2ssm(\underline{\omega}_{e/i}^{(n)}))v_{b/e}^{(n)}\} \quad \textbf{2-84}$$

where

$$(\underline{\tilde{f}}_{b/i}^{(n)} - \underline{f}_{b/i}^{(n)}) = \underbrace{\tilde{C}_{b}^{n}}_{\delta \tilde{C}_{b}^{n,(n)} C_{b}^{n}} \underline{\tilde{f}}_{b/i}^{(b)} - C_{b}^{n} \underline{f}_{b/i}^{(b)} \quad \textbf{2-85}$$

$$(\underline{\tilde{f}}_{b/i}^{(n)} - \underline{f}_{b/i}^{(n)}) = \underbrace{\delta \tilde{C}_{b}^{n,(n)}}_{I_{3x3}+ssm(\delta\Psi_{b/n}^{(n)})} C_{b}^{n} \underline{\tilde{f}}_{b/i}^{(b)} - C_{b}^{n} \underline{f}_{b/i}^{(b)} \quad \textbf{2-86}$$

$$(\underline{\tilde{f}}_{b/i}^{(n)} - \underline{f}_{b/i}^{(n)}) = C_{b}^{n}(\underline{\tilde{f}}_{b/i}^{(b)} - \underline{f}_{b/i}^{(b)}) - ssm(C_{b}^{n} \underbrace{\underline{\tilde{f}}_{b/i}^{(b)}}_{f_{b/i}^{(b)}+\delta f_{b/i}^{(b)}})\delta\Psi_{b/n}^{(n)} \quad \textbf{2-87}$$

Neglecting multiplication of error terms

$$(\underline{\tilde{f}}_{b/i}^{(n)} - \underline{f}_{b/i}^{(n)}) = C_{b}^{n}(\underline{\tilde{f}}_{b/i}^{(b)} - \underline{f}_{b/i}^{(b)}) - ssm(C_{b}^{n} \underline{f}_{b/i}^{(b)})\delta\Psi_{b/n}^{(n)} \quad \textbf{2-88}$$

From gravity model given in Appendix A, the perturbed form of the local gravity vector can be written as follow. Since the dependency of $\delta L_{b/e}$ over $r_{s/e}^{e}$ is so weak, its variation can be neglected.

$$\underline{\tilde{g}}_{b}^{(n)} - \underline{g}_{b}^{(n)} = -\frac{2g_{0,D}^{(n)}}{\left|r_{s/e}^{e}\right|}\delta h_{b/e} \quad \textbf{2-89}$$

$$\{(ssm(\underline{\tilde{\omega}}_{n/e}^{(n)}) + 2ssm(\underline{\tilde{\omega}}_{e/i}^{(n)}))\tilde{v}_{b/e}^{(n)} - (ssm(\underline{\omega}_{n/e}^{(n)}) + 2ssm(\underline{\omega}_{e/i}^{(n)}))v_{b/e}^{(n)}\} =$$
$$\{(ssm(\underline{\tilde{\omega}}_{n/e}^{(n)}) + 2ssm(\underline{\tilde{\omega}}_{e/i}^{(n)}))(v_{b/e}^{(n)} + \delta v_{b/e}^{(n)}) - (ssm(\underline{\omega}_{n/e}^{(n)}) + 2ssm(\underline{\omega}_{e/i}^{(n)}))v_{b/e}^{(n)}\} \quad \textbf{2-90}$$

$$\{(ssm(\underline{\tilde{\omega}}_{n/e}^{(n)}) + 2ssm(\underline{\tilde{\omega}}_{e/i}^{(n)}))\tilde{v}_{b/e}^{(n)} - (ssm(\underline{\omega}_{n/e}^{(n)}) + 2ssm(\underline{\omega}_{e/i}^{(n)}))v_{b/e}^{(n)}\} =$$
$$- ssm(v_{b/e}^{(n)})(\underline{\tilde{\omega}}_{n/e}^{(n)} - \underline{\omega}_{n/e}^{(n)}) - 2ssm(v_{b/e}^{(n)})(\underline{\tilde{\omega}}_{e/i}^{(n)} - \underline{\omega}_{e/i}^{(n)}) \cdots$$
$$+ (ssm(\underbrace{\underline{\tilde{\omega}}_{n/e}^{(n)}}_{\omega_{n/e}^{(n)}+\delta\omega_{n/e}^{(n)}}) + 2ssm(\underbrace{\underline{\tilde{\omega}}_{e/i}^{(n)}}_{\omega_{e/i}^{(n)}+\delta\omega_{e/i}^{(n)}}))\delta v_{b/e}^{(n)} \quad \textbf{2-91}$$

Neglecting multiplication of error terms

$$\{(ssm(\underline{\widetilde{\omega}}_{n/e}^{(n)}) + 2ssm(\underline{\widetilde{\omega}}_{e/i}^{(n)}))\widetilde{v}_{b/e}^{(n)} - (ssm(\underline{\omega}_{n/e}^{(n)}) + 2ssm(\underline{\omega}_{e/i}^{(n)}))v_{b/e}^{(n)}\} =$$
$$- ssm(v_{b/e}^{(n)})(\underline{\widetilde{\omega}}_{n/e}^{(n)} - \underline{\omega}_{n/e}^{(n)}) - 2ssm(v_{b/e}^{(n)})(\underline{\widetilde{\omega}}_{e/i}^{(n)} - \underline{\omega}_{e/i}^{(n)}) \cdots$$
$$+ (ssm(\underline{\omega}_{n/e}^{(n)}) + 2ssm(\underline{\omega}_{e/i}^{(n)}))\delta v_{b/e}^{(n)}$$

2-92

where

$$2ssm(v_{b/e}^{(n)})(\underline{\widetilde{\omega}}_{e/i}^{(n)} - \underline{\omega}_{e/i}^{(n)}) =$$
$$2\begin{bmatrix} 0 & -v_{b/e,D}^{(n)} & v_{b/e,E}^{(n)} \\ v_{b/e,D}^{(n)} & 0 & -v_{b/e,N}^{(n)} \\ -v_{b/e,E}^{(n)} & v_{b/e,N}^{(n)} & 0 \end{bmatrix}\begin{bmatrix} \sin(L_{b/e}) \\ 0 \\ \cos(L_{b/e}) \end{bmatrix}(-\Omega_{e/i})\delta L_{b/e}$$

2-93

$$2ssm(v_{b/e}^{(n)})(\underline{\widetilde{\omega}}_{e/i}^{(n)} - \underline{\omega}_{e/i}^{(n)}) =$$
$$\begin{bmatrix} -2\Omega_{e/i}\cos(L_{b/e})v_{b/e,E}^{(n)} \\ -2\Omega_{e/i}\sin(L_{b/e})v_{b/e,D}^{(n)} + 2\Omega_{e/i}\cos(L_{b/e})v_{b/e,N}^{(n)} \\ 2\Omega_{e/i}\sin(L_{b/e})v_{b/e,E}^{(n)} \end{bmatrix}\delta L_{b/e}$$

2-94

$$(ssm(\underline{\omega}_{n/e}^{(n)}) + 2ssm(\underline{\omega}_{e/i}^{(n)}))\delta v_{b/e}^{(n)} = \begin{bmatrix} 0 & \frac{v_{b/e,E}^{(n)}\tan(L_{b/e})}{(R_E+h_{b/e})} & \frac{-v_{b/e,N}^{(n)}}{(R_N+h_{b/e})} \\ \frac{-v_{b/e,E}^{(n)}\tan(L_{b/e})}{(R_E+h_{b/e})} & 0 & \frac{-v_{b/e,E}^{(n)}}{(R_E+h_{b/e})} \\ \frac{v_{b/e,N}^{(n)}}{(R_N+h_{b/e})} & \frac{v_{b/e,E}^{(n)}}{(R_E+h_{b/e})} & 0 \end{bmatrix}\cdots$$
$$+ \begin{bmatrix} 0 & 2\Omega_{e/i}\sin(L_{b/e}) & 0 \\ -2\Omega_{e/i}\sin(L_{b/e}) & 0 & -2\Omega_{e/i}\cos(L_{b/e}) \\ 0 & 2\Omega_{e/i}\cos(L_{b/e}) & 0 \end{bmatrix}\delta v_{b/e}^{(n)}$$

2-95

$$(ssm(\underline{\omega}_{n/e}^{(n)}) + 2ssm(\underline{\omega}_{e/i}^{(n)}))\delta v_{b/e}^{(n)} =$$
$$\begin{bmatrix} 2\Omega_{e/i}\sin(L_{b/e})\delta v_{b/e,E}^{(n)} + \frac{v_{b/e,E}^{(n)}\tan(L_{b/e})}{(R_E+h_{b/e})}\delta v_{b/e,E}^{(n)} - \frac{v_{b/e,N}^{(n)}}{(R_N+h_{b/e})}\delta v_{b/e,D}^{(n)} \\ -2\Omega_{e/i}\sin(L_{b/e})\delta v_{b/e,N}^{(n)} - \frac{v_{b/e,E}^{(n)}\tan(L_{b/e})}{(R_E+h_{b/e})}\delta v_{b/e,N}^{(n)} - \frac{v_{b/e,E}^{(n)}}{(R_E+h_{b/e})}\delta v_{b/e,D}^{(n)} - 2\Omega_{e/i}\cos(L_{b/e})\delta v_{b/e,D}^{(n)} \\ \frac{v_{b/e,N}^{(n)}}{(R_N+h_{b/e})}\delta v_{b/e,N}^{(n)} + \frac{v_{b/e,E}^{(n)}}{(R_E+h_{b/e})}\delta v_{b/e,E}^{(n)} + 2\Omega_{e/i}\cos(L_{b/e})\delta v_{b/e,E}^{(n)} \end{bmatrix}$$

2-96

$$ssm(v_{b/e}^{(n)})(\underline{\widetilde{\omega}}_{n/e}^{(n)} - \underline{\omega}_{n/e}^{(n)}) =$$
$$\begin{bmatrix} 0 & -v_{b/e,D}^{(n)} & v_{b/e,E}^{(n)} \\ v_{b/e,D}^{(n)} & 0 & -v_{b/e,N}^{(n)} \\ v_{b/e,E}^{(n)} & v_{b/e,N}^{(n)} & 0 \end{bmatrix}\begin{bmatrix} \frac{\delta v_{b/e,E}^{(n)}}{(R_E+h_{b/e})} - \frac{v_{b/e,E}^{(n)}}{(R_E+h_{b/e})^2}\delta h_{b/e} \\ -\frac{\delta v_{b/e,N}^{(n)}}{(R_N+h_{b/e})} + \frac{v_{b/e,N}^{(n)}}{(R_N+h_{b/e})^2}\delta h_{b/e} \\ -\frac{\delta v_{b/e,E}^{(n)}\tan(L_{b/e})}{(R_E+h_{b/e})} - \frac{v_{b/e,E}^{(n)}}{(R_E+h_{b/e})\cos^2(L_{b/e})}\delta L_{b/e} + \frac{v_{b/e,E}^{(n)}\tan(L_{b/e})}{(R_E+h_{b/e})^2}\delta h_{b/e} \end{bmatrix}$$

2-97

$$ssm(\underline{v}_{b/e}^{(n)})(\underline{\tilde{\omega}}_{n/e}^{(n)} - \underline{\omega}_{n/e}^{(n)}) =$$

$$\begin{bmatrix} \dfrac{v_{b/e,D}^{(n)}}{(R_N + h_{b/e})}\delta v_{b/e,N}^{(n)} - \dfrac{v_{b/e,D}^{(n)}v_{b/e,N}^{(n)}}{(R_N + h_{b/e})^2}\delta h_{b/e} - \dfrac{v_{b/e,E}^{(n)}\tan(L_{b/e})}{(R_E + h_{b/e})}\delta v_{b/e,E}^{(n)} - \dfrac{(v_{b/e,E}^{(n)})^2}{(R_E + h_{b/e})\cos^2(L_{b/e})}\delta L_{b/e} + \dfrac{(v_{b/e,E}^{(n)})^2\tan(L_{b/e})}{(R_E + h_{b/e})^2}\delta h_{b/e} \\[2ex] \dfrac{v_{b/e,D}^{(n)}}{(R_E + h_{b/e})}\delta v_{b/e,E}^{(n)} - \dfrac{v_{b/e,D}^{(n)}v_{b/e,E}^{(n)}}{(R_E + h_{b/e})^2}\delta h_{b/e} + \dfrac{v_{b/e,N}^{(n)}\tan(L_{b/e})}{(R_E + h_{b/e})}\delta v_{b/e,E}^{(n)} + \dfrac{v_{b/e,D}^{(n)}v_{b/e,E}^{(n)}}{(R_E + h_{b/e})\cos^2(L_{b/e})}\delta L_{b/e} - \dfrac{v_{b/e,D}^{(n)}v_{b/e,E}^{(n)}\tan(L_{b/e})}{(R_E + h_{b/e})^2}\delta h_{b/e} \\[2ex] -\dfrac{v_{b/e,E}^{(n)}}{(R_E + h_{b/e})}\delta v_{b/e,E}^{(n)} + \dfrac{(v_{b/e,E}^{(n)})^2}{(R_E + h_{b/e})^2}\delta h_{b/e} - \dfrac{v_{b/e,N}^{(n)}}{(R_N + h_{b/e})}\delta v_{b/e,N}^{(n)} + \dfrac{(v_{b/e,N}^{(n)})^2}{(R_N + h_{b/e})^2}\delta h_{b/e} \end{bmatrix} \qquad \textbf{2-98}$$

2.4.3 Position Error

Time derivative of the curvilinear positions are given in the expression (2.18), (2.19) and (2.20). The perturbed forms are expressed as follow

$$\delta \dot{L}_{b/e} = \tilde{\dot{L}}_{b/e} - \dot{L}_{b/e} = \frac{\delta v_{b/e,N}^{(n)}}{R_N + h_{b/e}} - \frac{v_{b/e,N}^{(n)}}{(R_N + h_{b/e})^2}\delta h_{b/e} \qquad \textbf{2-99}$$

$$\delta \dot{\lambda}_{b/e} = \tilde{\dot{\lambda}}_{b/e} - \dot{\lambda}_{b/e} = \frac{\delta v_{b/e,E}^{(n)}}{(R_E + h_{b/e})\cos(L_{b/e})} - \frac{v_{b/e,E}^{(n)}}{(R_E + h_{b/e})^2\cos(L_{b/e})}\delta h_{b/e} \cdots$$
$$+ \frac{v_{b/e,E}^{(n)}\sin(L_{b/e})}{(R_E + h_{b/e})\cos^2(L_{b/e})}\delta L_{b/e} \qquad \textbf{2-100}$$

$$\delta \dot{h}_{b/e} = \tilde{\dot{h}}_{b/e} - \dot{h}_{b/e} = -\delta v_{b/e,D}^{(n)} \qquad \textbf{2-101}$$

2.4.4 State-Space Representation of Error Dynamics

The more appropriate and easy to follow method of grouping the expressions derived in part 2.4.1, 2.4.2 and 2.4.3 is state-space representation.

$$[\delta \dot{x}] = [F][\delta x] + [U] \qquad \textbf{2-102}$$

where $[\delta x]$ is system states, $[F]$ is system internal dynamics matrix (shortly system matrix and $[U]$ is system input matrix.

$$\underbrace{\begin{bmatrix} \overline{\delta \ddot{p}_{b/e}^{(n)}} \\ \overline{\delta \ddot{v}_{b/e}^{(n)}} \\ \delta \dot{\Psi}_{b/n}^{(n)} \end{bmatrix}}_{[\delta \dot{x}]} = \underbrace{\begin{bmatrix} F_{PP} & F_{PV} & 0_{3x3} \\ F_{VP} & F_{VV} & F_{V\Psi} \\ F_{\Psi P} & F_{\Psi V} & F_{\Psi\Psi} \end{bmatrix}}_{[F]} \underbrace{\begin{bmatrix} \overline{\delta p_{b/e}^{(n)}} \\ \overline{\delta v_{b/e}^{(n)}} \\ \delta \Psi_{b/n}^{(n)} \end{bmatrix}}_{[\delta x]} + \underbrace{\begin{bmatrix} 0_{3x3} \\ C_b^n(\tilde{\underline{f}}_{b/i}^{(b)} - \underline{f}_{b/i}^{(b)}) \\ C_b^n(\tilde{\underline{\omega}}_{b/i}^{(b)} - \underline{\omega}_{b/i}^{(b)}) \end{bmatrix}}_{[U]} \qquad \textbf{2-103}$$

Whole $[F_{ii}]$, $\ ii = P, V, \Psi$ terms are derived in the previous sections.

$$F_{PP} = \begin{bmatrix} 0 & 0 & -\dfrac{v_{b/e,N}^{(n)}}{(R_N + h_{b/e})^2} \\[2ex] \dfrac{v_{b/e,E}^{(n)} \sin(L_{b/e})}{(R_E + h_{b/e})\cos^2(L_{b/e})} & 0 & -\dfrac{v_{b/e,E}^{(n)}}{(R_E + h_{b/e})^2 \cos(L_{b/e})} \\[2ex] 0 & 0 & 0 \end{bmatrix}$$ 2-104

$$F_{PV} = \begin{bmatrix} \dfrac{1}{(R_N + h_{b/e})} & 0 & 0 \\[2ex] 0 & \dfrac{1}{(R_E + h_{b/e})\cos(L_{b/e})} & 0 \\[2ex] 0 & 0 & -1 \end{bmatrix}$$ 2-105

$F_{VP} =$

$$\begin{bmatrix} -\dfrac{(v_{b/e,E}^{(n)})^2}{(R_E + h_{b/e})\cos^2(L_{b/e})} - 2v_{b/e,E}^{(n)}\Omega_{e/i}\cos(L_{b/e}) & 0 & \dfrac{(v_{b/e,E}^{(n)})^2 \tan(L_{b/e})}{(R_E + h_{b/e})^2} - \dfrac{v_{b/e,N}^{(n)} v_{b/e,D}^{(n)}}{(R_E + h_{b/e})^2} \\[3ex] \dfrac{v_{b/e,N}^{(n)} v_{b/e,E}^{(n)}}{(R_E + h_{b/e})\cos^2(L_{b/e})} + 2v_{b/e,N}^{(n)}\Omega_{e/i}\cos(L_{b/e}) & 0 & -\dfrac{(v_{b/e,N}^{(n)} v_{b/e,E}^{(n)} \tan(L_{b/e}) + v_{b/e,E}^{(n)} v_{b/e,D}^{(n)})}{(R_E + h_{b/e})^2} \\ -2v_{b/e,D}^{(n)}\Omega_{e/i}\sin(L_{b/e}) & & \\[2ex] -2v_{b/e,E}^{(n)}\Omega_{e/i}\sin(L_{b/e}) & 0 & \dfrac{(v_{b/e,E}^{(n)})^2}{(R_E + h_{b/e})^2} + \dfrac{(v_{b/e,N}^{(n)})^2}{(R_N + h_{b/e})^2} - \dfrac{2g_{0,D}^{(n)}}{|r_{s/e}^e|} \end{bmatrix}$$ 2-106

$F_{VV} =$

$$\begin{bmatrix} \dfrac{v_{b/e,D}^{(n)}}{(R_N + h_{b/e})} & -\dfrac{2v_{b/e,E}^{(n)}\tan(L_{b/e})}{(R_E + h_{b/e})} - 2\Omega_{e/i}\sin(L_{b/e}) & \dfrac{v_{b/e,N}^{(n)}}{(R_N + h_{b/e})} \\[3ex] \dfrac{v_{b/e,E}^{(n)}\tan(L_{b/e})}{(R_E + h_{b/e})} + 2\Omega_{e/i}\sin(L_{b/e}) & \dfrac{v_{b/e,N}^{(n)}\tan(L_{b/e}) + v_{b/e,D}^{(n)}}{(R_E + h_{b/e})} & -\dfrac{v_{b/e,E}^{(n)}}{(R_E + h_{b/e})} - 2\Omega_{e/i}\cos(L_{b/e}) \\ -\dfrac{2v_{b/e,N}^{(n)}}{(R_N + h_{b/e})} & -\dfrac{2v_{b/e,E}^{(n)}}{(R_E + h_{b/e})} - 2\Omega_{e/i}\cos(L_{b/e}) & 0 \end{bmatrix}$$ 2-107

$$F_{V\Psi} = -ssm(C_b^n \underline{f_{b/i}^{(b)}})$$ 2-108

$$F_{\Psi P} = \begin{bmatrix} \Omega_{e/i}\sin(L_{b/e}) & 0 & \dfrac{v_{b/e,E}^{(n)}}{(R_N + h_{b/e})^2} \\[2ex] 0 & 0 & -\dfrac{v_{b/e,N}^{(n)}}{(R_N + h_{b/e})^2} \\[2ex] \Omega_{e/i}\cos(L_{b/e}) + \dfrac{v_{b/e,E}^{(n)}}{(R_N + h_{b/e})\cos^2(L_{b/e})} & 0 & -\dfrac{v_{b/e,E}^{(n)}\tan(L_{b/e})}{(R_N + h_{b/e})^2} \end{bmatrix}$$ 2-109

$$F_{\Psi V} = \begin{bmatrix} 0 & -\dfrac{1}{(R_E + h_{b/e})} & 0 \\ \dfrac{1}{(R_N + h_{b/e})} & 0 & 0 \\ 0 & \dfrac{\tan(L_{b/e})}{(R_E + h_{b/e})} & 0 \end{bmatrix}$$

$\qquad\qquad$ **2-110**

$$F_{\Psi\Psi} = -ssm(\underline{\omega}_{n/i}^{(n)})$$

$\qquad\qquad$ **2-111**

where

$$\underline{\omega}_{n/i}^{(n)} = \underline{\omega}_{n/e}^{(n)} + \underline{\omega}_{e/i}^{(n)} = \begin{bmatrix} \dfrac{v_{b/e,E}^{(n)}}{(R_E + h_{b/e})} + \Omega_{e/i}\cos(L_{b/e}) \\ \dfrac{-v_{b/e,N}^{(n)}}{(R_N + h_{b/e})} \\ \dfrac{-v_{b/e,E}^{(n)}\tan(L_{b/e})}{(R_E + h_{b/e})} - \Omega_{e/i}\sin(L_{b/e}) \end{bmatrix}$$

$\qquad\qquad$ **2-112**

2.5 Inertial Sensors Error Modelling

Both of the accelerometers and gyroscopes suffer from constant error which is independent from the underlying specific force and angular rate. The constant error called as bias error is generally splitted into two fundamental part naming static/fixed/turn-on/repeatable part and dynamic/stability/instability part. Those names given with slash signs are commonly used interchangeable in literature. Apart from accelerometer, gyroscopes especially which are having moving parts such as mechanical, MEMS products suffer from acceleration dependent bias error. Scale factor error on the other hand is the departure of the sensor input-output gradient from unity. Besides that, inertial sensors exhibit different scaling error over the operation range and the variation related to scale factor error is named as nonlinearity. Both of the error sources aforementioned are illustrated on the figure below.
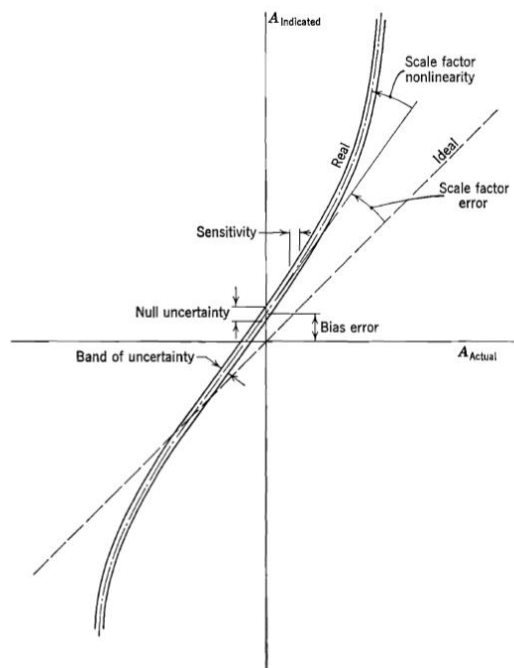
Figure 2.7 Scale Factor and Bias Error [(Adopted from [27])]

Cross-coupling errors in all types of IMU arise from the misalignment of the sensitive axes of the inertial sensors with respect to the orthogonal axes of the body frame. The sensitive axes of the inertial sensors frequently do not form orthogonal triad and this case is valid for both accelerometer and gyroscope triads. As stated by [9] and common assumptions are;

- One of the inertial sensor axis is assumed coincident with orthogonal IMU body axes. Generally, x axis of accelerometer is picked as the IMU chassis x axis which is depicted as sensor frame defined in part 2.1 .

- According to the first statement, y axis of the IMU chassis lies in the plane spanned by x and y axis of accelerometer triad.

The assumptions given above relate the accelerometer triad to orthogonal IMU body axis or in other words, sensor frame by pure rotation. For the gyroscope triad, measurements in the non-orthogonal gyroscope triad frame can be related to orthogonal IMU via 6 different angle represented in the following figure.

28
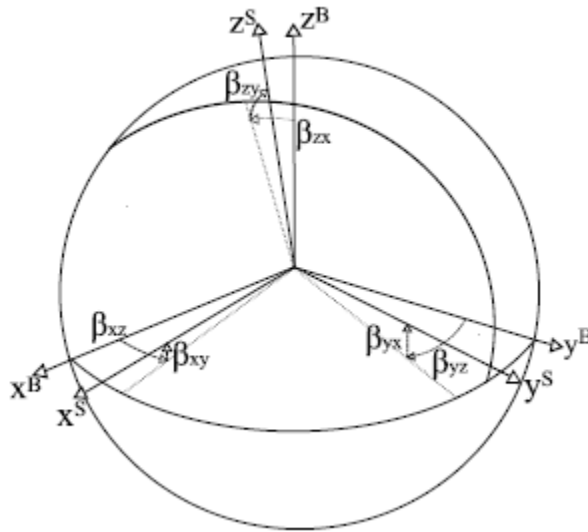
Figure 2.8 Misalignment of Non-Orthogonal Sensor Triad [(Adopted from [9])]

Apart from the deterministic error terms, all kind of inertial sensors suffer from random noise due to various sources. Depending on the manufacturing technologies of inertial sensors, the source of random noise varies.

The relationship between inertial sensors performance parameters and enabling technologies well tabulated into the following tables.

Table 2.2 Inertial Sensor Enabling Technologies and Performance Parameter [(The Upper Table is Adopted From [10] and The Lower Tables are Adopted From [23])]

IMU technology and IMU performance

Class	Position performance	Gyro technology	Accelerometer technology	Gyro bias	Acc bias
"Military grade"	1 nmi / 24 h	ESG, RLG, FOG	Servo accelerometer	< 0.005°/h	< 30 µg
Navigation grade	1 nmi / h	RLG, FOG	Servo accelerometer, Vibrating beam	0.01°/h	50 µg
Tactical grade	> 10 nmi / h	RLG, FOG	Servo accelerometer, Vibrating beam, MEMS	1°/h	1 mg
AHRS	NA	MEMS, RLG, FOG, Coriolis	MEMS	1 - 10°/h	1 mg
Control system	NA	Coriolis	MEMS	10 - 1000°/h	10 mg

29

Characteristic	RIG	DTG	Flex gyroscope	DART/MHD	Vibratory gyro	RLG	FOG
g-Independent bias (°/h)	0.05–10	0.05–10	1–50	360–1800	360–1800	0.001–10	0.5–50
g-Dependent bias (°/h/g)	1–10	0.01–10	1–10	180	36–180	0	<1
Anisoelastic bias (°/h/g^2)	1–2	0.1–0.5	0.05–0.25	18–40	18	0	<0.1
Scale-factor non-linearity (%)	0.01–0.1	0.01–0.1	0.01–0.1	0.5–0.1	0.2–0.3	5–100	0.05–0.5
Bandwidth (Hz)	60	100	100	100/80	500	>200	>100
Maximum input rate (°/s)	>400	1000	>500	800/400	>1000	>1000	>1000
Shock resistance	Moderate	Moderate	Moderate	Moderate	>25 000g	Good	Good

Characteristic	Accelerometer type				
	Force-feedback pendulous	Vibrating fibre optic	Vibrating quartz	SAW	Silicon
Input range (g)	±100	±20	±200	±100	±100
Scale-factor stability (%)	0.1	0.001	0.01	0.1–0.5	0.5–2
Scale-factor non-linearity (% full scale)	0.05	0.05	0.05	<0.1	0.1–0.4
Fixed bias (milli-g)	0.1–10	1	0.1–1	<0.5	<25
Threshold (micro-g)	10	1	<10	1–10	1–10
Bandwidth (Hz)	400	100	400	400	400

2.5.1 Accelerometers Error Model

Accelerometer triad sensor model used in this study is given below.

$$\widetilde{\underline{f}}_{b/i}^{(b)} = \underline{b}_a + (I_{3x3} + M_a)\underline{f}_{b/i}^{(b)} + \underline{w}_a \qquad \text{2-113}$$

where

$\underline{f}_{b/i}^{(b)}$ True specific force

$\widetilde{\underline{f}}_{b/i}^{(b)}$ IMU indicated specific force

$\underline{b}_a$ Accelerometers Bias

M_a Scale factor and Misalignment (Cross-Coupling) error

$\underline{w}_a$ White noise term (Velocity Random Walk is the main contributer)

30

$$M_a = \begin{bmatrix} S_{a,x} & M_{a,xy} & M_{a,xz} \\ 0 & S_{a,y} & M_{a,yz} \\ 0 & 0 & S_{a,z} \end{bmatrix}$$

2-114

Dynamic bias and scale-factor non linearity errors can be modelled as stochastic models described in Appendix B. In this study, they are both modelled as a random walk process.

$$\dot{b}_{a,i} = w_{b_{a,i}}$$

2-115

where $w_{b_{a,i}} : (\underbrace{0}_{mean}, \underbrace{\sigma^2_{b_{ai,d}}}_{variance})$

$$\dot{S}_{a,i} = w_{S_{a,i}}$$

2-116

where $w_{S_{a,i}} : (\underbrace{0}_{mean}, \underbrace{\sigma^2_{S_{ai,d}}}_{variance})$

2.5.2   Gyroscopes Error Model

Similar to accelerometer case, gyroscope error model is given below.

$$\underline{\tilde{\omega}}^{(b)}_{b/i} = \underline{b}_g + (I_{3x3} + M_g)\underline{\omega}^{(b)}_{b/i} + G_g \underline{f}^{(b)}_{b/i} + \underline{w}_g$$

2-117

where

$\underline{\omega}^{(b)}_{b/i}$	True angular rate
$\underline{\tilde{\omega}}^{(b)}_{b/i}$	IMU indicated angular rate
$\underline{b}_g$	Gyroscopes Bias
M_g	Scale factor and Misalignment (Cross-Coupling) error
G_g	Acceleration dependent error (g-dependent)
$\underline{w}_g$	White noise term (Angular Random Walk is the main contributer)

$$M_g = \begin{bmatrix} S_{g,x} & M_{g,xy} & M_{g,xz} \\ M_{g,yx} & S_{g,y} & M_{g,yz} \\ M_{g,zx} & M_{g,zy} & S_{g,z} \end{bmatrix}$$

2-118

$$G_g = \begin{bmatrix} G_{g,xx} & G_{g,xy} & G_{g,xz} \\ G_{g,yx} & G_{g,yy} & G_{g,yz} \\ G_{g,zx} & G_{g,zy} & G_{g,zz} \end{bmatrix}$$

2-119

Dynamic bias and scale-factor non linearity errors can be modelled as exponentially correlated Gauss-Markow process which is explained in Appendix B.

$$\dot{b}_{g,i} = w_{b_{g,i}}$$

2-120

where $w_{b_{g,i}} : (\underbrace{0}_{mean}, \underbrace{\sigma^2_{b_{gi,d}}}_{variance})$

$$\dot{S}_{g,i} = w_{S_{g,i}}$$

2-121

where $w_{S_{g,i}} : (\underbrace{0}_{mean}, \underbrace{\sigma^2_{S_{gi,d}}}_{variance})$

CHAPTER 3

SATELLITE NAVIGATION SYSTEMS

This chapter mainly reviews the fundamental concepts and the basic principle of operation of the satellite navigation systems. First, the general system overview related to short history behind the operational satellite navigation systems and their fundamental components is briefly touched. A description of the satellite system observables which is actually what is being measured and the various sources of error buried inside that observables is given. Finally, this chapter ends with the analytical equations that use the mentioned measurements to form position, velocity and time solutions.

3.1   Systems Operation Principles

As stated in [28], "GPS positioning is based on the one-way ranging technique: the time of travel of a signal transmitted by satellites is measured and scaled by speed of light to obtain the satellite-user distance". That is the fundamental principle lies behind the operation concept of GPS is that each satellite sends out navigation signals, together with a set of its orbital parameters called ephemeris data. This declaration is in fact valid not only GPS but also for the whole satellite systems.The satellite system receiver captures these signals and it is able to process and calculate the user position, velocity and time (PVT) solution. In order to reach that objective, the receiver also needs the satellite position and velocity values which are obtained via ephemeris information. Ephemeris is mainly a set of orbital parameters and their rate of change at a specified system time. Satellites continuously transmit the ephemeris data inside the navigation message. The transmitted ephemeris information is regularly updated by the ground stations which monitors the

satellites. According to the system, ephemeris data or satellite orbital elements are formed mainly in two ways. First type is that satellite ephemeris includes kepler parameters and the related orbit perturbation correction parameters. During the time of this declaration GPS, Galileo and BeiDou satellites transmit ephemeris data including kepler and the related perturbation parameters. However, Global Navigation Satellite System (GLONASS) satellites transmit ephemeris that is containing the position, velocity and acceleration values referenced to ECEF coordinate system at specified system time. The mentioned parameters which used to calculate satellite position and velocity from two different ephemeris form is detailly explained in related ICDs [29,30]. In terms of GPS and GLONASS satellites, several publishment such as [31] can be followed for computing satellite position and velocity information from satellite transmitted ephemeris.

The received ranging signals from transmitted satellites are decoded and used as range measurements between satellites and the receiver. Since within the receiver, a replica code of satellite-generated one is created, that code is shifted in time until the correlation is achieved. If both of the satellite and the receiver clocks are synchronized in a perfect manner, the multiplication of propagation time of the ranging code by the speed of light results in the true range between the satellite and the receiver. Generally, the receiver clock has a large bias error deviated from system time and the perfect synchronization is not possible. Therefore, the determined range during correlation process is denoted as pseudorange. As declared in [32], "The measurement is called pseudorange because it is the range determined by multiplying the signal propagation velocity, c, by the time difference between two nonsynchronized clocks (the satellite clock and the receiver clock). The measurement contains (1) the geometric satellite-to-user range, (2) an offset attributed to the difference between the system time and the user clock, and (3) an offset between system time and the satellite clock." Therefore, in order to solve for the user position, range measurements from at least four distinct satellites are necessary because the receiver clock offset error is the fourth unknown together with three dimensional position unknowns.

3.2   Pseudorange and Delta Range Observables

Before dealing with the error sources inside the observables, the timing relationship between satellite and the receiver is given as below.
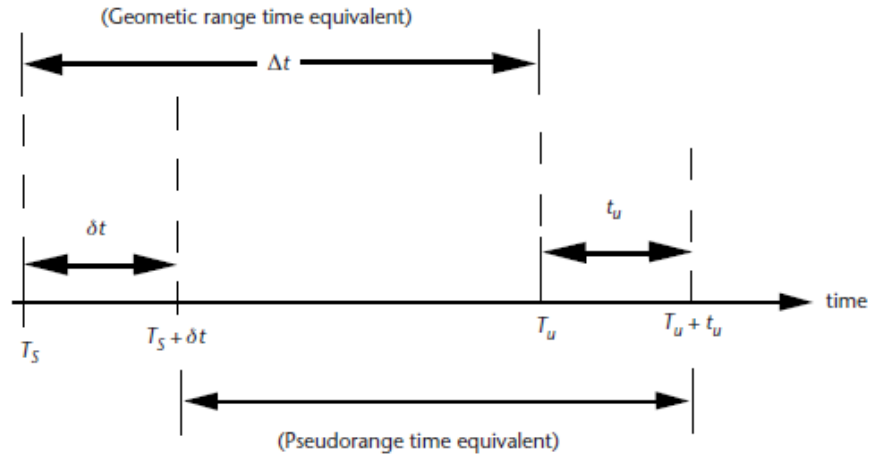

Figure 3.1 Range Measurement Timing Relationships [Adopted from [32]]

where

T_s	System time at which the signal left the satellite
T_u	System time at which the signal reached the user receiver
δt	Offset of the satellite clock from system time [advance is positive; retardation (delay) is negative]
t_u	Offset of the receiver clock from system time
$T_s + \delta t$	Satellite clock reading at the time that the signal left the satellite
$T_u + t_u$	User receiver clock reading at the time the signal reached the user receiver
c	Speed of light

Geometric range $r = c(T_u - T_s) = c\Delta t$ **3-1**

Pseudorange $\rho = c[(T_u + t_u) - (T_s + \delta t)]$
(ideal) $\rho = r + c(t_u - \delta t)$ **3-2**

As indicated in the previous section, the pseudorange observables are not the true geometric ranges and contain error sources. The expression (3.2) is valid for error free environment which is not valid for the real case. Therefore, the pseudorange between the satellite and the receiver can be written as follows:

Pseudorange $\qquad \rho = r + c(t_u - \delta t) + \rho_{iono} + \rho_{tropo} + \varepsilon_{multipath} + \varepsilon_{\rho,noise}$ $\qquad$ **3-3**

where

ρ_{iono} $\qquad$ Range error due to delay induced by Ionosphere

ρ_{tropo} $\qquad$ Range error due to delay induced by Troposphere

$\varepsilon_{multipath}$ $\qquad$ Range error due to multipath effect

$\varepsilon_{\rho,noise}$ $\qquad$ Range error due to random noise

In addition to pseudorange observable, the doppler measurement can be used to determine the user velocity. The pseudorange rate observable is given as follows:

Pseudorange rate $\qquad \dot{\rho} = \dot{r} + \dot{\rho}_{drift} + \varepsilon_{\dot{\rho},noise}$ $\qquad$ **3-4**

where

$\dot{\rho}$ $\qquad$ Rate of change of geometric range

$\dot{r}$ $\qquad$ Rate of change of pseudorange

$\dot{\rho}_{drift}$ $\qquad$ Bias error due to receiver clock drift

$\varepsilon_{\dot{\rho},noise}$ $\qquad$ Range rate error due to random noise

3.3 Satellite Navigation System Measurement Equations

The true range from user to i[th] satellite is

$$r_i = \left| r_{sv/e,i}^{(e)} - r_{b/e}^{(e)} \right|$$ $\qquad$ **3-5**

$$r_i = \sqrt{\left(r_{sv/e,i}^{(e)}(1) - r_{b/e}^{(e)}(1) \right)^2 + \left(r_{sv/e,i}^{(e)}(2) - r_{b/e}^{(e)}(2) \right)^2 + \left(r_{sv/e,i}^{(e)}(3) - r_{b/e}^{(e)}(3) \right)^2}$$

After the corrections related to atmosphere and satellite clock are made, the pseudorange equation becomes;

$$\rho_i = \sqrt{\left(r^{(e)}_{sv/e,i}(1) - r^{(e)}_{b/e}(1)\right)^2 + \left(r^{(e)}_{sv/e,i}(2) - r^{(e)}_{b/e}(2)\right)^2 + \left(r^{(e)}_{sv/e,i}(3) - r^{(e)}_{b/e}(3)\right)^2} + \rho_{offset} + \varepsilon_{\rho,i}$$ **3-6**

where

ρ_i Pseudorange measurement from user position to i[th] satellite

$$\underline{r^{(e)}_{sv/e,i}} = \begin{bmatrix} r^{(e)}_{sv/e,i}(1) \\ r^{(e)}_{sv/e,i}(2) \\ r^{(e)}_{sv/e,i}(3) \end{bmatrix}$$ i[th] satellite position matrix

$$\underline{r^{(e)}_{b/e}} = \begin{bmatrix} r^{(e)}_{b/e}(1) \\ r^{(e)}_{b/e}(2) \\ r^{(e)}_{b/e}(3) \end{bmatrix}$$ The user position matrix

$\rho_{offset} = ct_u$ The receiver clock offset

$\varepsilon_{\rho,i}$ Range error due to random noise

The equation (3.6) is nonlinear for unknown user position. In order to construct linear model, it is necessary to linearize it.

$$let \quad h(\tilde{x}) = \sqrt{\left(r^{(e)}_{sv/e,i}(1) - r^{(e)}_{b/e}(1)\right)^2 + \left(r^{(e)}_{sv/e,i}(2) - r^{(e)}_{b/e}(2)\right)^2 + \left(r^{(e)}_{sv/e,i}(3) - r^{(e)}_{b/e}(3)\right)^2}$$ **3-7**

Using Taylor series expansion around the approximate user position matrix denoted as $\underline{r^{(e)}_a}$ and neglecting higher order terms;

$$h(\tilde{x}) = h(x_a + \delta x)$$

$$h(\tilde{x}) \approx h(x_a) + \frac{dh(x_a)}{dx}\delta x + HOT$$ **3-8**

Using both expressions (3.7) and (3.8) result in;

$$h(\tilde{x}) = \underbrace{\sqrt{\left(r^{(e)}_{sv/e,i}(1) - r^{(e)}_a(1)\right)^2 + \left(r^{(e)}_{sv/e,i}(2) - r^{(e)}_a(2)\right)^2 + \left(r^{(e)}_{sv/e,i}(3) - r^{(e)}_a(3)\right)^2}}_{h(x_a)} + \cdots$$
$$+ \underbrace{\left\{ -\left(\frac{r^{(e)}_{sv/e,i}(1) - r^{(e)}_a(1)}{h(x_a)}\right)\delta r^{(e)}_{b/e}(1) - \left(\frac{r^{(e)}_{sv/e,i}(2) - r^{(e)}_a(2)}{h(x_a)}\right)\delta r^{(e)}_{b/e}(2) - \left(\frac{r^{(e)}_{sv/e,i}(3) - r^{(e)}_a(3)}{h(x_a)}\right)\delta r^{(e)}_{b/e}(3) \right\}}_{\frac{dh(x_a)}{dx}\delta x}$$ **3-9**

By aid of expression (3.9), reformulate the equation (3.6).

$$\rho_i = \sqrt{\left(r_{sv/e,i}^{(e)}(1) - r_a^{(e)}(1)\right)^2 + \left(r_{sv/e,i}^{(e)}(2) - r_a^{(e)}(2)\right)^2 + \left(r_{sv/e,i}^{(e)}(3) - r_a^{(e)}(3)\right)^2} \cdots$$
$$+ \left\{ -\left(\frac{r_{sv/e,i}^{(e)}(1) - r_a^{(e)}(1)}{h(x_a)}\right)\delta r_{b/e}^{(e)}(1) - \left(\frac{r_{sv/e,i}^{(e)}(2) - r_a^{(e)}(2)}{h(x_a)}\right)\delta r_{b/e}^{(e)}(2) - \left(\frac{r_{sv/e,i}^{(e)}(3) - r_a^{(e)}(3)}{h(x_a)}\right)\delta r_{b/e}^{(e)}(3) \right\} \cdots$$
$$+ \rho_{offset} + \varepsilon_{\rho,i}$$

3-10

In more organized way,

$$\rho_i - \rho_a = h_{i1}\delta r_{b/e}^{(e)}(1) + h_{i2}\delta r_{b/e}^{(e)}(2) + h_{i3}\delta r_{b/e}^{(e)}(3) + \rho_{offset} + \varepsilon_{\rho,i}$$

3-11

where

$$\rho_a = \sqrt{\left(r_{sv/e,i}^{(e)}(1) - r_a^{(e)}(1)\right)^2 + \left(r_{sv/e,i}^{(e)}(2) - r_a^{(e)}(2)\right)^2 + \left(r_{sv/e,i}^{(e)}(3) - r_a^{(e)}(3)\right)^2}$$

$$h_{i1} = -\left(\frac{r_{sv/e,i}^{(e)}(1) - r_a^{(e)}(1)}{h(x_a)}\right) = -\left(\frac{r_{sv/e,i}^{(e)}(1) - r_a^{(e)}(1)}{\rho_a}\right)$$

$$h_{i2} = -\left(\frac{r_{sv/e,i}^{(e)}(2) - r_a^{(e)}(2)}{h(x_a)}\right) = -\left(\frac{r_{sv/e,i}^{(e)}(2) - r_a^{(e)}(2)}{\rho_a}\right)$$

$$h_{i3} = -\left(\frac{r_{sv/e,i}^{(e)}(3) - r_a^{(e)}(3)}{h(x_a)}\right) = -\left(\frac{r_{sv/e,i}^{(e)}(3) - r_a^{(e)}(3)}{\rho_a}\right)$$

The expression (3.11) can be put in matrix form by using four pseudorange measurements.

$$\underbrace{\begin{bmatrix} \rho_1 - \rho_a \\ \rho_2 - \rho_a \\ \rho_3 - \rho_a \\ \rho_4 - \rho_a \end{bmatrix}}_{\Delta\rho} = \underbrace{\begin{bmatrix} h_{11} & h_{12} & h_{13} & 1 \\ h_{21} & h_{22} & h_{23} & 1 \\ h_{31} & h_{32} & h_{33} & 1 \\ h_{41} & h_{42} & h_{43} & 1 \end{bmatrix}}_{H} \underbrace{\begin{bmatrix} \delta r_{b/e}^{(e)}(1) \\ \delta r_{b/e}^{(e)}(2) \\ \delta r_{b/e}^{(e)}(3) \\ \rho_{offset} \end{bmatrix}}_{\Delta x} + \underbrace{\begin{bmatrix} \varepsilon_{\rho,1} \\ \varepsilon_{\rho,2} \\ \varepsilon_{\rho,3} \\ \varepsilon_{\rho,4} \end{bmatrix}}_{v_\rho}$$

3-12

If there is only four pseudorange measurements, one may use below expression for obtaining solution.

$$\Delta x = H^{-1}\Delta\rho$$

3-13

Generally, more than four measurements are available and the expression (3.12) becomes over-determined. Least square method is commonly used for that case.

$$\Delta x = (H^T H)^{-1} H^T \Delta \rho \qquad \textbf{3-14}$$

The aforementioned calculations with least square method are generally an iterative method. The solution of expression (3.14) is used to correct the approximate user position as described below. Later, the same procedure is followed with the new position and clock offset estimate until the estimated position corrections become so small compared to the predefined threshold.

$$\begin{bmatrix} r_{b/e}^{(e)}(1) \\ r_{b/e}^{(e)}(2) \\ r_{b/e}^{(e)}(3) \end{bmatrix}_{k+1} = \begin{bmatrix} r_{b/e}^{(e)}(1) \\ r_{b/e}^{(e)}(2) \\ r_{b/e}^{(e)}(3) \end{bmatrix}_{k} + \begin{bmatrix} \Delta x(1) \\ \Delta x(2) \\ \Delta x(3) \end{bmatrix} \qquad \textbf{3-15}$$

The pseudorange rate is directly the time derivative of pseudorange. Therefore differentiate the expression (3.6) yields

$$\dot{\rho}_i = \frac{1}{2} \frac{2\left(r_{sv/e,i}^{(e)}(1) - r_{b/e}^{(e)}(1)\right)\left(\dot{r}_{sv/e,i}^{(e)}(1) - \dot{r}_{b/e}^{(e)}(1)\right)}{\sqrt{\left(r_{sv/e,i}^{(e)}(1) - r_{b/e}^{(e)}(1)\right)^2 + \left(r_{sv/e,i}^{(e)}(2) - r_{b/e}^{(e)}(2)\right)^2 + \left(r_{sv/e,i}^{(e)}(3) - r_{b/e}^{(e)}(3)\right)^2}} \cdots$$
$$+ \frac{1}{2} \frac{2\left(r_{sv/e,i}^{(e)}(2) - r_{b/e}^{(e)}(2)\right)\left(\dot{r}_{sv/e,i}^{(e)}(2) - \dot{r}_{b/e}^{(e)}(2)\right)}{\sqrt{\left(r_{sv/e,i}^{(e)}(1) - r_{b/e}^{(e)}(1)\right)^2 + \left(r_{sv/e,i}^{(e)}(2) - r_{b/e}^{(e)}(2)\right)^2 + \left(r_{sv/e,i}^{(e)}(3) - r_{b/e}^{(e)}(3)\right)^2}} \cdots \qquad \textbf{3-16}$$
$$+ \frac{1}{2} \frac{2\left(r_{sv/e,i}^{(e)}(3) - r_{b/e}^{(e)}(3)\right)\left(\dot{r}_{sv/e,i}^{(e)}(3) - \dot{r}_{b/e}^{(e)}(3)\right)}{\sqrt{\left(r_{sv/e,i}^{(e)}(1) - r_{b/e}^{(e)}(1)\right)^2 + \left(r_{sv/e,i}^{(e)}(2) - r_{b/e}^{(e)}(2)\right)^2 + \left(r_{sv/e,i}^{(e)}(3) - r_{b/e}^{(e)}(3)\right)^2}} \cdots$$
$$+ \dot{\rho}_{drift} + \varepsilon_{\dot{\rho},i}$$

$$\dot{\rho}_i = \frac{\left(r_{sv/e,i}^{(e)}(1) - r_{b/e}^{(e)}(1)\right)\left(\dot{r}_{sv/e,i}^{(e)}(1) - \dot{r}_{b/e}^{(e)}(1)\right)}{\rho_i} + \frac{\left(r_{sv/e,i}^{(e)}(2) - r_{b/e}^{(e)}(2)\right)\left(\dot{r}_{sv/e,i}^{(e)}(2) - \dot{r}_{b/e}^{(e)}(2)\right)}{\rho_i} \cdots$$
$$+ \frac{\left(r_{sv/e,i}^{(e)}(3) - r_{b/e}^{(e)}(3)\right)\left(\dot{r}_{sv/e,i}^{(e)}(3) - \dot{r}_{b/e}^{(e)}(3)\right)}{\rho_i} + \dot{\rho}_{drift} + \varepsilon_{\dot{\rho},i} \qquad \textbf{3-17}$$

where

$\dot{\rho}_i$ Pseudorange rate measurement from user position to i^{th} satellite

$$\underline{\dot{r}}_{sv/e,i}^{(e)} = \begin{bmatrix} \dot{r}_{sv/e,i}^{(e)}(1) \\ \dot{r}_{sv/e,i}^{(e)}(2) \\ \dot{r}_{sv/e,i}^{(e)}(3) \end{bmatrix}$$ i^{th} satellite velocity matrix

$$\underline{\dot{r}}_{b/e}^{(e)} = \begin{bmatrix} \dot{r}_{b/e}^{(e)}(1) \\ \dot{r}_{b/e}^{(e)}(2) \\ \dot{r}_{b/e}^{(e)}(3) \end{bmatrix}$$ The user velocity matrix

$\varepsilon_{\dot{\rho},i}$ Range rate error due to random noise

Similar to pseudorange equation, the equation (3.17) can be linearized by Taylor series expansion around the approximate user velocity matrix denoted as $\underline{\dot{r}}_a^{(e)}$.

$$\dot{\rho}_i - \dot{\rho}_a = h_{i1}\delta\ddot{r}_{b/e}^{(e)}(1) + h_{i2}\delta\ddot{r}_{b/e}^{(e)}(2) + h_{i3}\delta\ddot{r}_{b/e}^{(e)}(3) + \dot{\rho}_{drift} + \varepsilon_{\dot{\rho},i} \qquad \textbf{3-18}$$

where

$$\dot{\rho}_a = \frac{\left(r_{sv/e,i}^{(e)}(1) - r_{b/e}^{(e)}(1)\right)\left(\dot{r}_{sv/e,i}^{(e)}(1) - \dot{r}_a^{(e)}(1)\right)}{\rho_i} \quad \dots$$

$$+ \frac{\left(r_{sv/e,i}^{(e)}(2) - r_{b/e}^{(e)}(2)\right)\left(\dot{r}_{sv/e,i}^{(e)}(2) - \dot{r}_a^{(e)}(2)\right)}{\rho_i} + \frac{\left(r_{sv/e,i}^{(e)}(3) - r_{b/e}^{(e)}(3)\right)\left(\dot{r}_{sv/e,i}^{(e)}(3) - \dot{r}_a^{(e)}(3)\right)}{\rho_i} \qquad \textbf{3-19}$$

h_{i1}, h_{i2}, h_{i3} are defined in the description part of expression (3.11)

In matrix form;

$$\underbrace{\begin{bmatrix} \dot{\rho}_1 - \dot{\rho}_a \\ \dot{\rho}_2 - \dot{\rho}_a \\ \dot{\rho}_3 - \dot{\rho}_a \\ \dot{\rho}_4 - \dot{\rho}_a \end{bmatrix}}_{\underline{\Delta\dot{\rho}}} = \underbrace{\begin{bmatrix} h_{11} & h_{12} & h_{13} & 1 \\ h_{21} & h_{22} & h_{23} & 1 \\ h_{31} & h_{32} & h_{33} & 1 \\ h_{41} & h_{42} & h_{43} & 1 \end{bmatrix}}_{H} \underbrace{\begin{bmatrix} \delta\ddot{r}_{b/e}^{(e)}(1) \\ \delta\ddot{r}_{b/e}^{(e)}(2) \\ \delta\ddot{r}_{b/e}^{(e)}(3) \\ \dot{\rho}_{drift} \end{bmatrix}}_{\underline{\Delta\dot{x}}} + \underbrace{\begin{bmatrix} \varepsilon_{\dot{\rho},1} \\ \varepsilon_{\dot{\rho},2} \\ \varepsilon_{\dot{\rho},3} \\ \varepsilon_{\dot{\rho},4} \end{bmatrix}}_{\underline{v}_{\dot{\rho}}} \qquad \textbf{3-20}$$

The same iterative approach and the least square method solution are exactly the same as pseudorange measurements counterpart given in expressions (3.13) to (3.15).

3.4 Complementary Features of Inertial Navigation and Satellite Navigation Systems

The overview of inertial navigation system and satellite navigation systems are highlighted in chapter 2 and 3 so far. Since the sampling rate of the inertial sensors can be high as much as 50-1000 Hz, the INS can be operated at that rate as well. Oppose to INS, Satellite navigation system receivers cannot usually reach that much rate of generating navigation solution. In addition to that, INS is a fully self-contained standalone navigation system and can calculate full navigation solution including position, velocity and the attitude of the user. Single antenna receivers are however cannot tell much about the attitude of the user. As briefly mentioned above, both of the system has strength that can eliminate each other weaknesses. The complementary features of INS and satellite navigation system make blended integration schemes outperform the individual standalone system.

The detailed features of both systems are well tabulated below to clearly highlight the potential benefits of integration.

Table 3.1 Characteristic Features of GNSS and INS

GNSS	INS
Low data rate (1-10 Hz)	High data rate (50-1000 Hz)
Supply 3 dimensional position and velocity (Attitude solution requires additional hardware and complex algorithms)	Full navigation solution (3 dimensional position, velocity and attitude)
Self-contained system (Initial states are not necessary but clear sky view is necessary to conserve accuracy level)	Self-contained system (If initial states are supplied)
Susceptible to interferences (Signal blockage, jamming and spoofing)	Immune to jamming (Continuous operation)
Long term accuracy (Time independent accuracy and stability level)	Short term accuracy (Unbounded error growth due to constant integration process of noisy sensor measurements)

CHAPTER 4

DEVELOPMENT OF MULTI-PURPOSE INTEGRATED NAVIGATION SYSTEM MODEL

As stated in the earlier chapter, the development of integrated algorithm which incorporate different aiding sources is forming one of the main features of this study. For navigation applications utilizing low cost inertial sensor, the navigation solution accuracy degrades rapidly due to fact that uncompensated inertial sensor errors which is common for especially comsumer grade MEMS based inertial sensors produced with high quantity. Therefore, aiding inertial navigation system which is based on such sensors with every possible sources to calibrate the inertial sensors on the field becomes a critical task to maintaining the navigation performance several order of magnitude better when compared with pure inertial mean. In this study, especially for land navigation applications, one central commonly used Extended Kalman Filter structure is used as an integration algorithm that is blending the inertial navigation system with information and sources including GPS receiver, motion constraints of platforms, detection of static conditions together with field calibration of inertial sensor essentially depends upon magnitude of local gravity.

4.1 Kalman Filtering

"The Kalman filter is essentially a set of mathematical equations that implement a predictor-corrector type estimator that is optimal in the sense that it minimizes the estimated error covariance – when some presumed conditions are met." [33]. Over 50 years of extensive usage and practices among many researches and applications,

the Kalman filter is one of the most well-known mathematical tools that is essentially stochastic estimator from noisy measurements made from various types of sensors in terms of ease of understanding, optimal properties mentioned above, recursive estimation feature and low level of computation burden. From a very extensive explanation to application oriented simple examples and intuitive approaches related to understanding the Kalman filter is referenced in [34], [35], [36], [37], [38], [39], and [40].

"The Kalman filter estimates a process a form of feedback control: the filter estimates the process state at some time and then obtains a feedback in the form of (noisy) measurement." [33]. That is, the estimation process is based upon two different sets of equations which are named as time update part also known as predictor equations and measurement update part which includes corrector equations. The common form of Kalman filter recursive loop is highlighted in the following figure.
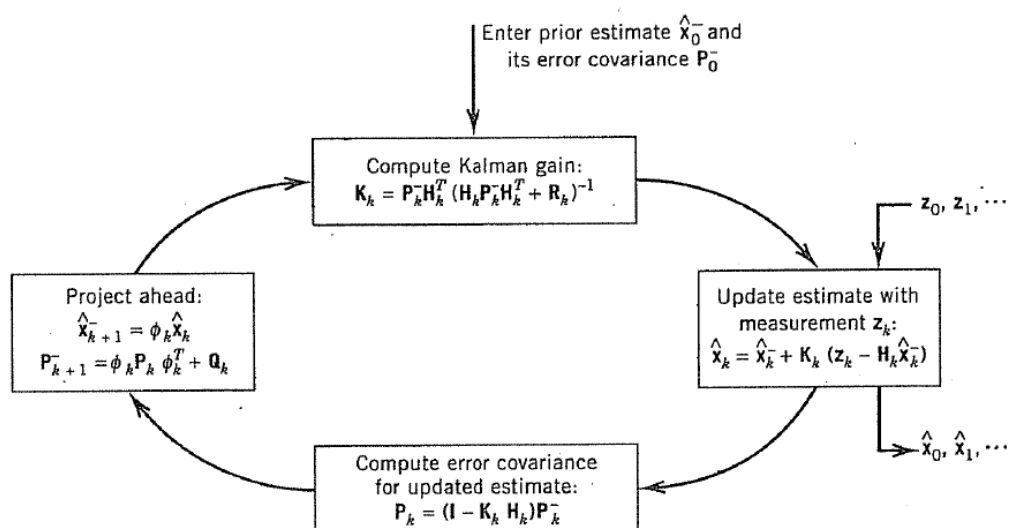
Figure 4.1 Kalman Loop (Adopted from [41])

Table 4.1 Kalman Loop Equations

Time Update	Measurement Update
$\hat{x}_{k+1}^- = \Phi_k \hat{x}_k$	$K_k = P_k^- H_k^T \left(H_k P_k^- H_k^T + R_k \right)^{-1}$
$P_{k+1}^- = \Phi_k P_k \Phi_k^T + Q_k$	$\hat{x}_k = \hat{x}_k^- + K_k \left(z_k - H_k \hat{x}_k^- \right)$
	$P_k = \left(I - K_k H_k \right) P_k^-$

4.2 Multi-Purpose Integrated Algorithm Operational Flow

The developed integrated navigation algorithm is simple integration of inertial navigation system with multi-measurement model Extended Kalman Filter as shown in the following figure. Inertial navigation mechanization process with necessary equations are detailly explained in chapter 2. The modular architecture concept comes from multi-measurement model including various types of aiding information from real or hypotetical sensors or estimated information enable integration algorithm to have a flexibility related to increase/decrease number of informations obtained from various forms of sources. In other words, the developed algorithm is operating on sequential form which is accepting any measurement from the modelled sources.
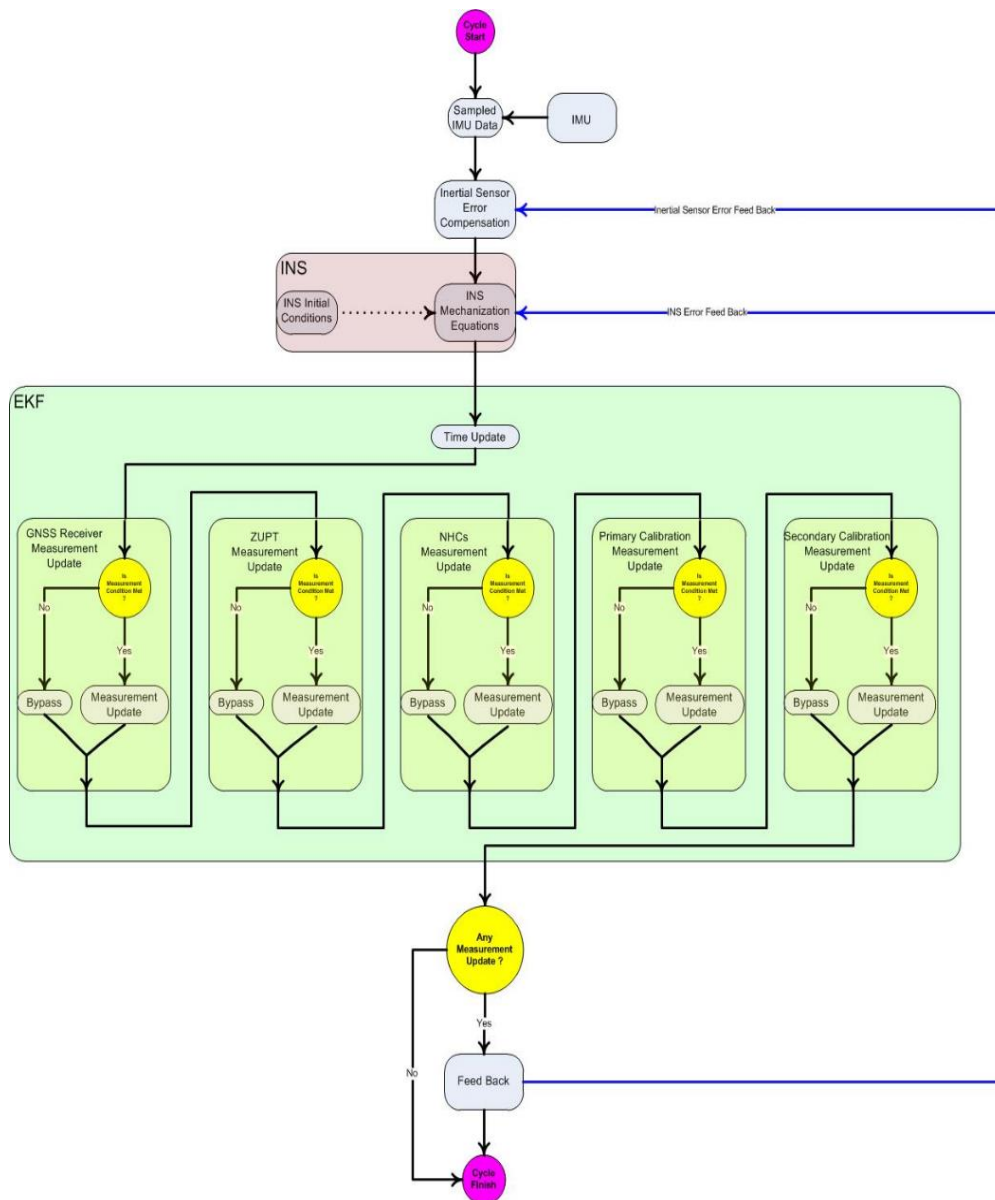
Figure 4.2 Multi-Purpose Integrated Algorithm Operational Flowchart

The well-known measurement update process that is given in the Table 4.1 is repeated for whole aiding informations if the necessary measurement condition sets are satisfied. Such condition check flow is given in the figure below. If the mentioned conditions are met, then the measurement update proess of Kalman filter takes place.
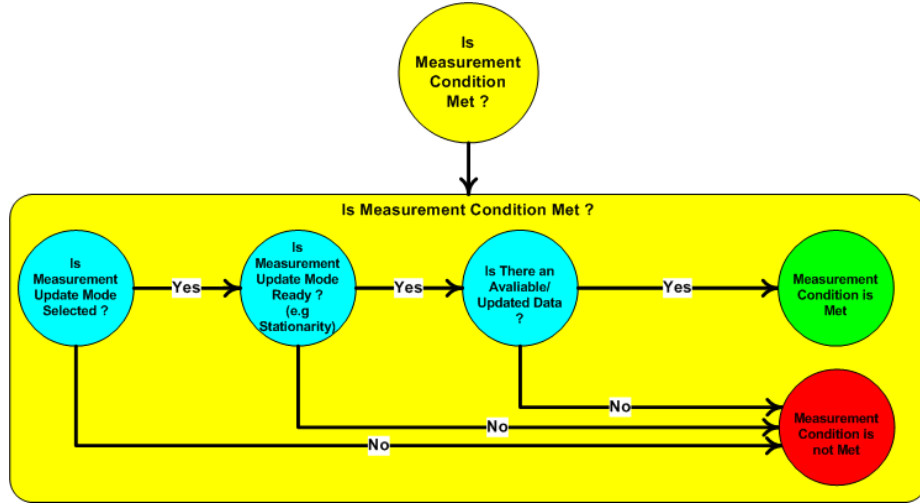
Figure 4.3 Generic Measurement Condition Check

4.3 System Model

As a system model, the standard use of full navigation error states system model and full inertial sensor error terms illustrated in part 2.4 and 2.5 respectively. From (2.113), the following expression is obtained

$$\underline{\tilde{f}}_{b/i}^{(b)} - \underline{f}_{b/i}^{(b)} \cong \underline{b}_a + M_a \underline{f}_{b/i}^{(b)} + \underline{w}_a \qquad \text{4-1}$$

For gyroscope case, using (2.114) in the similar manner yields

$$\underline{\tilde{\omega}}_{b/i}^{(b)} - \underline{\omega}_{b/i}^{(b)} \cong \underline{b}_g + M_g \underline{\omega}_{b/i}^{(b)} + G_g \underline{f}_{b/i}^{(b)} + \underline{w}_g \qquad \text{4-2}$$

In state-space representation, the above expression can be grouped as

$$
\underline{\tilde{f}}_{b/i}^{(b)} - \underline{f}_{b/i}^{(b)} \cong \underbrace{\begin{bmatrix} b_{a,x} \\ b_{a,y} \\ b_{a,z} \end{bmatrix}}_{b_a} + \underbrace{\begin{bmatrix} f_{b/i,x}^{(b)} & 0 & 0 \\ 0 & f_{b/i,x}^{(b)} & 0 \\ 0 & 0 & f_{b/i,x}^{(b)} \end{bmatrix}}_{A^*} \underbrace{\begin{bmatrix} S_{a,x} \\ S_{a,y} \\ S_{a,z} \end{bmatrix}}_{S_a} \ldots
$$

$$
+ \underbrace{\begin{bmatrix} f_{b/i,y}^{(b)} & f_{b/i,z}^{(b)} & 0 \\ 0 & 0 & f_{b/i,z}^{(b)} \\ 0 & 0 & 0 \end{bmatrix}}_{A^{**}} \underbrace{\begin{bmatrix} M_{a,xy} \\ M_{a,xz} \\ M_{a,yz} \end{bmatrix}}_{M_a} + \underbrace{\begin{bmatrix} w_{a,x} \\ w_{a,y} \\ w_{a,z} \end{bmatrix}}_{w_a} \qquad \text{4-3}
$$

$$\underline{\widetilde{\omega}}_{b/i}^{(b)} - \underline{\omega}_{b/i}^{(b)} \cong \underbrace{\begin{bmatrix} b_{g,x} \\ b_{g,y} \\ b_{g,z} \end{bmatrix}}_{b_g} + \underbrace{\begin{bmatrix} \omega_{b/i,x}^{(b)} & 0 & 0 \\ 0 & \omega_{b/i,x}^{(b)} & 0 \\ 0 & 0 & \omega_{b/i,x}^{(b)} \end{bmatrix}}_{G^*} \underbrace{\begin{bmatrix} S_{g,x} \\ S_{g,y} \\ S_{g,z} \end{bmatrix}}_{S_g} \cdots$$

$$+ \underbrace{\begin{bmatrix} \omega_{b/i,y}^{(b)} & \omega_{b/i,z}^{(b)} & 0 & 0 & 0 & 0 \\ 0 & 0 & \omega_{b/i,x}^{(b)} & \omega_{b/i,z}^{(b)} & 0 & 0 \\ 0 & 0 & 0 & 0 & \omega_{b/i,x}^{(b)} & \omega_{b/i,y}^{(b)} \end{bmatrix}}_{G^{**}} \underbrace{\begin{bmatrix} M_{g,xy} \\ M_{g,xz} \\ M_{g,yx} \\ M_{g,yz} \\ M_{g,zx} \\ M_{g,zy} \end{bmatrix}}_{M_g} + \cdots$$

4-4

$$+ \underbrace{\begin{bmatrix} f_{b/i,x}^{(b)} & f_{b/i,y}^{(b)} & f_{b/i,z}^{(b)} & 0 & 0 & 0 & 0 & 0 & 0 \\ 0 & 0 & 0 & f_{b/i,x}^{(b)} & f_{b/i,y}^{(b)} & f_{b/i,z}^{(b)} & 0 & 0 & 0 \\ 0 & 0 & 0 & 0 & 0 & 0 & f_{b/i,x}^{(b)} & f_{b/i,y}^{(b)} & f_{b/i,z}^{(b)} \end{bmatrix}}_{G^{***}} \underbrace{\begin{bmatrix} G_{g,xx} \\ G_{g,xy} \\ G_{g,xz} \\ G_{g,yx} \\ G_{g,yy} \\ G_{g,yz} \\ G_{g,zx} \\ G_{g,zy} \\ G_{g,zz} \end{bmatrix}}_{G_g} + \underbrace{\begin{bmatrix} w_{g,x} \\ w_{g,y} \\ w_{g,z} \end{bmatrix}}_{w_g}$$

Now full state-space representation of system model can be obtained by using expression (4.3), (4.4), (2.103) with the system states given below. As oppose to Chapter 2, abbreviation such as S_a, S_g, M_a, $M_{g,}$ and G_g are used here to symbolize column matrices which should not be confused with the square matrices that are highlighted in part 2.5.

$$[\delta \dot{x}] = [F][\delta x] + [G][w]$$

4-5

$$[\delta x] = \begin{bmatrix} \underbrace{\delta p_{b/e}^{(n)T}}_{1x3} & \underbrace{\delta v_{b/e}^{(n)T}}_{1x3} & \underbrace{\delta \Psi_{b/n}^{(n)T}}_{1x3} & \underbrace{b_a^T}_{1x3} & \underbrace{b_g^T}_{1x3} & \underbrace{S_a^T}_{1x3} & \underbrace{M_a^T}_{1x3} & \underbrace{S_g^T}_{1x3} & \underbrace{M_g^T}_{1x6} & \underbrace{G_g^T}_{1x9} \end{bmatrix}^T_{1x39}$$

4-6

$$\underline{\delta \ddot{p}}_{b/e}^{(n)} = F_{PP} \, \underline{\delta p}_{b/e}^{(n)} + F_{PV} \, \underline{\delta v}_{b/e}^{(n)}$$

4-7

$$\underline{\delta \dot{v}}_{b/e}^{(n)} = F_{VP} \, \underline{\delta p}_{b/e}^{(n)} + F_{VV} \, \underline{\delta v}_{b/e}^{(n)} + F_{V\Psi} \, \underline{\delta \Psi}_{b/n}^{(n)} + C_b^n \left(\underline{\widetilde{f}}_{b/i}^{(b)} - \underline{f}_{b/i}^{(b)} \right)$$

4-8

$$\underline{\delta \dot{\Psi}}_{b/e}^{(n)} = F_{\Psi P} \, \underline{\delta p}_{b/e}^{(n)} + F_{\Psi V} \, \underline{\delta v}_{b/e}^{(n)} + F_{\Psi \Psi} \, \underline{\delta \Psi}_{b/n}^{(n)} + C_b^n \left(\underline{\widetilde{\omega}}_{b/i}^{(b)} - \underline{\omega}_{b/i}^{(b)} \right)$$

4-9

$$
\underbrace{\begin{bmatrix} \delta\ddot{p}_{b/e}^{(n)} \\ \delta\dot{v}_{b/e}^{(n)} \\ \delta\dot{\Psi}_{b/n}^{(n)} \\ \dot{b}_a \\ \dot{b}_g \\ \dot{S}_a \\ \dot{M}_a \\ \dot{S}_g \\ \dot{M}_g \\ \dot{G}_g \end{bmatrix}}_{[\dot{\delta x}]}
=
\underbrace{\begin{bmatrix}
F_{PP} & F_{PV} & 0_{3x3} & 0_{3x3} & 0_{3x3} & 0_{3x3} & 0_{3x3} & 0_{3x3} & 0_{3x6} & 0_{3x9} \\
F_{VP} & F_{VV} & F_{V\Psi} & C_b^n & 0_{3x3} & C_b^n A^* & C_b^n A^{**} & 0_{3x3} & 0_{3x6} & 0_{3x9} \\
F_{\Psi P} & F_{\Psi V} & F_{\Psi\Psi} & 0_{3x3} & C_b^n & 0_{3x3} & 0_{3x3} & C_b^n G^* & C_b^n G^{**} & C_b^n G^{***} \\
0_{3x3} & 0_{3x3} & 0_{3x3} & 0_{3x3} & 0_{3x3} & 0_{3x3} & 0_{3x3} & 0_{3x3} & 0_{3x6} & 0_{3x9} \\
0_{3x3} & 0_{3x3} & 0_{3x3} & 0_{3x3} & 0_{3x3} & 0_{3x3} & 0_{3x3} & 0_{3x3} & 0_{3x6} & 0_{3x9} \\
0_{3x3} & 0_{3x3} & 0_{3x3} & 0_{3x3} & 0_{3x3} & 0_{3x3} & 0_{3x3} & 0_{3x3} & 0_{3x6} & 0_{3x9} \\
0_{3x3} & 0_{3x3} & 0_{3x3} & 0_{3x3} & 0_{3x3} & 0_{3x3} & 0_{3x3} & 0_{3x3} & 0_{3x6} & 0_{3x9} \\
0_{3x3} & 0_{3x3} & 0_{3x3} & 0_{3x3} & 0_{3x3} & 0_{3x3} & 0_{3x3} & 0_{3x3} & 0_{3x6} & 0_{3x9} \\
0_{6x3} & 0_{6x3} & 0_{6x3} & 0_{6x3} & 0_{6x3} & 0_{6x3} & 0_{6x3} & 0_{6x3} & 0_{6x6} & 0_{6x9} \\
0_{9x3} & 0_{9x3} & 0_{9x3} & 0_{9x3} & 0_{9x3} & 0_{9x3} & 0_{9x3} & 0_{9x3} & 0_{9x6} & 0_{9x9}
\end{bmatrix}}_{[F]}
\underbrace{\begin{bmatrix} \delta p_{b/e}^{(n)} \\ \delta v_{b/e}^{(n)} \\ \delta\Psi_{b/n}^{(n)} \\ b_a \\ b_g \\ S_a \\ M_a \\ S_g \\ M_g \\ G_g \end{bmatrix}}_{[\delta x]} \dots
$$

$$
\dots +
\underbrace{\begin{bmatrix}
0_{3x3} & 0_{3x3} & 0_{3x3} & 0_{3x3} & 0_{3x3} & 0_{3x3} \\
C_b^n & 0_{3x3} & 0_{3x3} & 0_{3x3} & 0_{3x3} & 0_{3x3} \\
0_{3x3} & C_b^n & 0_{3x3} & 0_{3x3} & 0_{3x3} & 0_{3x3} \\
0_{3x3} & 0_{3x3} & I_{3x3} & 0_{3x3} & 0_{3x3} & 0_{3x3} \\
0_{3x3} & 0_{3x3} & 0_{3x3} & I_{3x3} & 0_{3x3} & 0_{3x3} \\
0_{3x3} & 0_{3x3} & 0_{3x3} & 0_{3x3} & I_{3x3} & 0_{3x3} \\
0_{3x3} & 0_{3x3} & 0_{3x3} & 0_{3x3} & 0_{3x3} & 0_{3x3} \\
0_{3x3} & 0_{3x3} & 0_{3x3} & 0_{3x3} & 0_{3x3} & I_{3x3} \\
0_{6x3} & 0_{6x3} & 0_{6x3} & 0_{6x3} & 0_{6x3} & 0_{6x3} \\
0_{9x3} & 0_{9x3} & 0_{9x3} & 0_{9x3} & 0_{9x3} & 0_{9x3}
\end{bmatrix}}_{[G]}
\underbrace{\begin{bmatrix} w_a \\ w_g \\ w_{b_a} \\ w_{b_g} \\ w_{S_a} \\ w_{S_g} \end{bmatrix}}_{[w]}
$$

4-10

Bias and scale factor errors of inertial sensors are modelled as random walk which is explained in Appendix B.

For this study, loosely coupled integration is taken into consideration. If tight or ultra-tight architectures were used, it would been necessary to add GNSS receiver clock offset and drift to system model. For the sake of completeness, the clock offset and clock drift is modelled as given below.

$$
\frac{d}{dt}\left(\delta\rho_{offset}\right) = \delta\dot{\rho}_{drift} + w_{\delta\rho_{offset}}
$$

4-11

where w is the receiver clock offset driving noise

$$
\frac{d}{dt}\left(\delta\dot{\rho}_{drift}\right) = w_{\delta\dot{\rho}_{drift}}
$$

4-12

where w is the receiver clock drift driving noise

4.4   INS/GNSS Integration

As shown in Table 3.1, the integration of INS/GNSS enables the user to exploit the complementary characteristics and gain uninterrupted navigation solution with both short and long term accuracy. The common integration schemes of INS and GNSS receiver illustrated in the Figure 4.4. For loosely coupled integration, both of the inertial navigation system and GNSS receiver navigation filter operates individually. GNSS receiver navigation filter outputs are aided to INS in terms of position and/or velocity information. As it is stated in the section 3, in order to form navigation solution for GNSS navigation filter four individual satellite signals are necessary. However, tightly coupled integration scheme uses GNSS receiver raw ranging information to aid INS. The last and the most cumbersome integration architecture is ultra-tight form (some author uses deep integration) in which GNSS receiver and INS devices no longer work as independent systems, GNSS measurement are used to estimate INS error and INS measurement to aid GNSS receiver tracking loops.
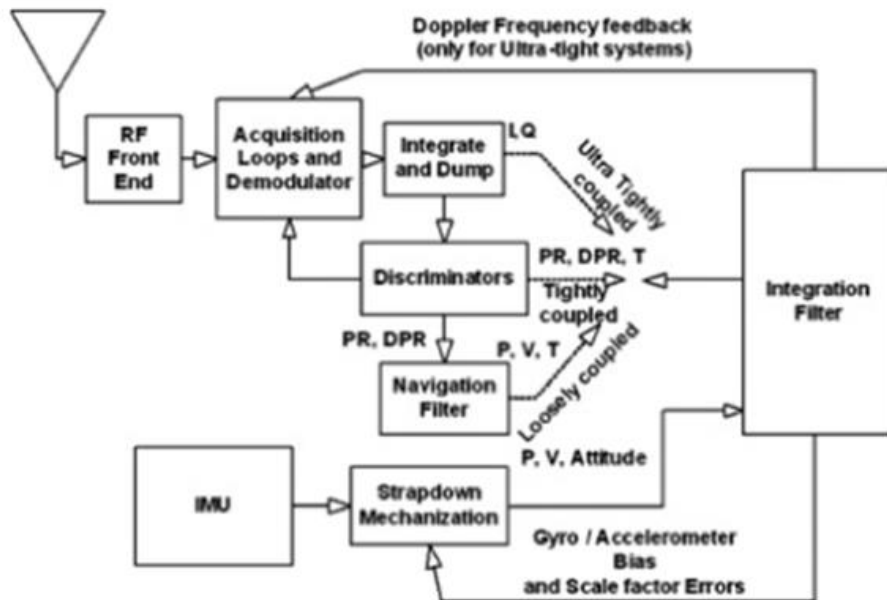
Figure 4.4 Loose, Tight and Ultra-Tight INS/GNSS Navigation System

4.4.1 INS/GNSS Integration Measurement Model

The two common integration architecture of INS and GNSS receiver system measurement modelling is described below.

4.4.1.1 Loosely Coupled INS/GNSS Measurement Model

Loosely coupled (LC) integration mainly rely on the output of navigation filter of GNSS receiver which are generally 3D linear position and linear velocity informations.

$$\underline{\delta z} = H \delta x + \underline{\eta} \tag{4-13}$$

For LC, the measurement vector consists of the difference between GNSS receiver position, velocity and the INS position, velocity.

$$\underline{\delta z} = \begin{bmatrix} \underline{p}^{(n)}_{b/e,GNSS} - \underline{\widetilde{p}}^{(n)}_{b/e} \\ \underline{v}^{(n)}_{b/e,GNSS} - \underline{\widetilde{v}}^{(n)}_{b/e} \end{bmatrix} = H \delta x + \underline{\eta} \tag{4-14}$$

$$\underline{p}^{(n)}_{b/e,GNSS} = \underline{p}^{(n)}_{b/e} + \underline{\eta}^{(n)}_{p^{(n)}_{b/e,GNSS}} \qquad\qquad \underline{v}^{(n)}_{b/e,GNSS} = \underline{v}^{(n)}_{b/e} + \underline{\eta}^{(n)}_{v^{(n)}_{b/e,GNSS}} \tag{4-15}$$

$$\underline{\widetilde{p}}^{(n)}_{b/e} = \underline{p}^{(n)}_{b/e} + \underline{\delta p}^{(n)}_{b/e} \qquad\qquad \underline{\widetilde{v}}^{(n)}_{b/e} = \underline{v}^{(n)}_{b/e} + \underline{\delta v}^{(n)}_{b/e} \tag{4-16}$$

$$\underline{\delta z} = \begin{bmatrix} \eta^{(n)}_{p^{(n)}_{b/e,GNSS}} - \underline{\delta p}^{(n)}_{b/e} \\ \eta^{(n)}_{v^{(n)}_{b/e,GNSS}} - \underline{\delta v}^{(n)}_{b/e} \end{bmatrix}$$

$$H = \begin{bmatrix} -I_{3x3} & 0_{3x3} & 0_{3x3} & 0_{3x3} & 0_{3x3} & 0_{3x3} & 0_{3x3} & 0_{3x3} & 0_{3x6} & 0_{3x9} \\ 0_{3x3} & -I_{3x3} & 0_{3x3} & 0_{3x3} & 0_{3x3} & 0_{3x3} & 0_{3x3} & 0_{3x3} & 0_{3x6} & 0_{3x9} \end{bmatrix} \tag{4-17}$$

$$\eta = \begin{bmatrix} \eta^{(n)}_{p^{(n)}_{b/e,GNSS}} \\ \underline{\eta}^{(n)}_{v^{(n)}_{b/e,GNSS}} \end{bmatrix} \tag{4-18}$$

4.4.1.2 Tightly Coupled INS/GNSS Measurement Model

Apart from loosely coupled integration, tight integration scheme is based on exploiting the raw GNSS receiver ranging and range rate informations. Since tight integration is not dependent upon the outputs of GNSS receiver navigation filter, only one integration algorithm generally Kalman filter can be used.

$$\delta z = H \delta x + \eta$$

$$
\delta z = \begin{bmatrix} \rho_{GNSS,i} - \tilde{\rho}_i \\ \vdots \\ \vdots \\ \dot{\rho}_{GNSS,i} - \dot{\tilde{\rho}}_i \\ \vdots \\ \vdots \end{bmatrix}
$$
4-19

$$\rho_{GNSS,i} = \rho_i + \delta\rho_{offset} + \eta_{\rho_{GNSS,i}}$$
4-20

$$\tilde{\rho}_i = \left| r_{sv/e,i}^{(e)} - \tilde{r}_{b/e}^{(e)} \right|$$

$$\tilde{\rho}_i = \underbrace{\sqrt{\left(r_{sv/e,i}^{(e)}(1) - \tilde{r}_{b/e}^{(e)}(1)\right)^2 + \left(r_{sv/e,i}^{(e)}(2) - \tilde{r}_{b/e}^{(e)}(2)\right)^2 + \left(r_{sv/e,i}^{(e)}(3) - \tilde{r}_{b/e}^{(e)}(3)\right)^2}}_{h(\tilde{x})}$$
4-21

Expression (4.21) can be linearized around the approximation point via using the 1st order Taylor approximation.

$$h(\tilde{x}) = h(x + \delta x) \underset{Approximation}{\overset{1^{st}\,orderTaylor}{\Longrightarrow\Longrightarrow\Longrightarrow\Longrightarrow}} h(\tilde{x}) = h(x) + \frac{dh(x)}{dx}\delta x$$

$$\tilde{\rho}_i = \underbrace{\sqrt{\left(r_{sv/e,i}^{(e)}(1) - r_{b/e}^{(e)}(1)\right)^2 + \left(r_{sv/e,i}^{(e)}(2) - r_{b/e}^{(e)}(2)\right)^2 + \left(r_{sv/e,i}^{(e)}(3) - r_{b/e}^{(e)}(3)\right)^2}}_{h(x)=\rho_i} \cdots$$

$$+ \underbrace{\left\{ -\left(\frac{r_{sv/e,i}^{(e)}(1) - r_{b/e}^{(e)}(1)}{\rho_i}\right)\delta r_{b/e}^{(e)}(1) - \left(\frac{r_{sv/e,i}^{(e)}(2) - r_{b/e}^{(e)}(2)}{\rho_i}\right)\delta r_{b/e}^{(e)}(2) - \left(\frac{r_{sv/e,i}^{(e)}(3) - r_{b/e}^{(e)}(3)}{\rho_i}\right)\delta r_{b/e}^{(e)}(3) \right\}}_{\frac{dh(x)}{dx}\delta x}$$
4-22

$$\tilde{\rho}_i = \rho_i - \left(LOS_{sv/b,i}^{(e)}\right)^T \delta r_{b/e}^{(e)}$$
4-23

4-24

$$LOS_{sv/b,i}^{(e)} = \begin{bmatrix} \left(\dfrac{r_{sv/e,i}^{(e)}(1) - r_{b/e}^{(e)}(1)}{\rho_i} \right) \\ \left(\dfrac{r_{sv/e,i}^{(e)}(2) - r_{b/e}^{(e)}(2)}{\rho_i} \right) \\ \left(\dfrac{r_{sv/e,i}^{(e)}(3) - r_{b/e}^{(e)}(3)}{\rho_i} \right) \end{bmatrix} \quad where \quad LOS : Line\ of\ sight\ vector$$

From expressions (2.18), (2.19), and (2.20), the relation between cartesian and curvilinear position errors which can be approximated as small increments can be formed as below.

$$\delta r_{b/e}^{(n)} = \begin{bmatrix} (R_N + h_{b/e}) & 0 & 0 \\ 0 & (R_E + h_{b/e})\cos(L_{b/e}) & 0 \\ 0 & 0 & -1 \end{bmatrix} \delta p_{b/e}^{(n)} \tag{4-25}$$

$$\tilde{\rho}_i = \rho_i - \left(C_n^e LOS_{sv/b,i}^{(n)} \right)^T C_n^e \delta r_{b/e}^{(n)} \Rightarrow\Rightarrow\Rightarrow \tilde{\rho}_i = \rho_i - \left(LOS_{sv/b,i}^{(n)} \right)^T \underbrace{C_e^n C_n^e}_{I_{3x3}} \delta r_{b/e}^{(n)} \tag{4-26}$$

$$\tilde{\rho}_i = \rho_i - \left(LOS_{sv/b,i}^{(n)} \right)^T \begin{bmatrix} (R_N + h_{b/e}) & 0 & 0 \\ 0 & (R_E + h_{b/e})\cos(L_{b/e}) & 0 \\ 0 & 0 & -1 \end{bmatrix} \delta p_{b/e}^{(n)} \tag{4-27}$$

Substitute the expression (4.20) into (4.27)

$$\rho_{GNSS,i} - \tilde{\rho}_i = \rho_i + \delta p_{offset} + \eta_{\rho_{GNSS,i}} \cdots$$
$$\cdots - \left(\rho_i - \left(LOS_{sv/b,i}^{(n)} \right)^T \begin{bmatrix} (R_N + h_{b/e}) & 0 & 0 \\ 0 & (R_E + h_{b/e})\cos(L_{b/e}) & 0 \\ 0 & 0 & -1 \end{bmatrix} \delta p_{b/e}^{(n)} \right) \tag{4-28}$$

$$\delta p_i = \left(LOS_{sv/b,i}^{(n)} \right)^T \begin{bmatrix} (R_N + h_{b/e}) & 0 & 0 \\ 0 & (R_E + h_{b/e})\cos(L_{b/e}) & 0 \\ 0 & 0 & -1 \end{bmatrix} \delta p_{b/e}^{(n)} \cdots \tag{4-29}$$
$$+ \delta p_{offset} + \eta_{\rho_{GNSS,i}}$$

Similar to pseudorange equation given as (4.20), pseudorange rate expression can be written as follow,

$$\dot{\rho}_{GNSS,i} = \dot{\rho}_i + \delta\dot{\rho}_{drift} + \eta_{\dot{\rho}_{GNSS,i}} \qquad \textbf{4-30}$$

$$\dot{\tilde{\rho}}_i = \left(\underline{\tilde{u}}_{sv/b,i}^{(e)}\right)^T \left(\underline{v}_{sv/e}^{(e)} - \underline{\tilde{v}}_{b/e}^{(e)}\right) \qquad \textbf{4-31}$$

Since positiyon error dependence of PRR by LOS is so weak, neglect variation of LOS

$$\dot{\tilde{\rho}}_i = \left(\underline{u}_{sv/b,i}^{(e)}\right)^T \left(\underline{v}_{sv/e}^{(e)} - \left(\underline{v}_{b/e}^{(e)} + \underline{\delta v}_{b/e}^{(e)}\right)\right)$$
$$\dot{\tilde{\rho}}_i = \underbrace{\left(\underline{u}_{sv/b,i}^{(e)}\right)^T \left(\underline{v}_{sv/e}^{(e)} - \underline{v}_{b/e}^{(e)}\right)}_{\dot{\rho}_i} - \left(\underline{u}_{sv/b,i}^{(e)}\right)^T \underline{\delta v}_{b/e}^{(e)} \qquad \textbf{4-32}$$

$$\dot{\tilde{\rho}}_i = \dot{\rho}_i - \underbrace{\left(C_n^e \underline{u}_{sv/b,i}^{(n)}\right)^T C_n^e \underline{\delta v}_{b/e}^{(n)}}_{\underset{I_{3x3}}{\left(\underline{u}_{sv/b,i}^{(n)}\right)^T \underline{C_e^n C_n^e} \underline{\delta v}_{b/e}^{(n)}}} \qquad \textbf{4-33}$$

$$\dot{\tilde{\rho}}_i = \dot{\rho}_i - \left(\underline{u}_{sv/b,i}^{(n)}\right)^T \underline{\delta v}_{b/e}^{(n)}$$

$$\dot{\rho}_{GNSS,i} - \dot{\tilde{\rho}}_i = \dot{\rho}_i + \delta\dot{\rho}_{drift} + \eta_{\dot{\rho}_{GNSS,i}} - \left(\dot{\rho}_i - \left(\underline{u}_{sv/b,i}^{(n)}\right)^T \underline{\delta v}_{b/e}^{(n)}\right) \qquad \textbf{4-34}$$

$$\delta\dot{\rho}_i = \left(\underline{u}_{sv/b,i}^{(n)}\right)^T \underline{\delta v}_{b/e}^{(n)} + \delta\dot{\rho}_{drift} + \eta_{\dot{\rho}_{GNSS,i}} \qquad \textbf{4-35}$$

4.5   Zero Velocity Update (ZUPT)

For the land vehicle applications, the platform stops frequently especially in urban environment. Therefore, the stationary state of the platform can be detected to aid inertial navigation system via using the knowledge of hypothetical zero velocity measurement.

4.5.1   Zero Velocity Update Measurement Model

When the static state of vehicle is captured, it can be used to prevent velocity error growth. The measurement model expression for ZUPT is given below.

$$\underline{z_{ext}} = \left[v_{b/e,ZUPT}^{(n)} \right] = \left[\underline{0_{3x1}} + \eta_{v_{b/e,ZUPT}^{(n)}}^{(n)} \right] \qquad \textbf{4-36}$$

$$\underline{\tilde{z}} = \left[\underline{\tilde{v}_{b/e}^{(n)}} \right] = \left[v_{b/e}^{(n)} + \delta v_{b/e}^{(n)} \right] \qquad \textbf{4-37}$$

$$\underline{\delta z} = \underline{z_{ext}} - \underline{\tilde{z}} = H\delta x + \underline{\eta}$$

$$H = \begin{bmatrix} 0_{3x3} & -I_{3x3} & 0_{3x33} \end{bmatrix} \qquad \textbf{4-38}$$

$$\left[\underline{\delta z} \right] = \left[H \right] \left[\delta x \right] + \left[\underline{\eta} \right]$$

$$\left[\underline{v_{b/e,ZUPT}^{(n)}} - \underline{\tilde{v}_{b/e}^{(n)}} \right] = \begin{bmatrix} 0_{3x3} & -I_{3x3} & 0_{3x33} \end{bmatrix} \left[\delta x \right] + \left[\underline{\eta_{v_{b/e,ZUPT}^{(n)}}} \right] \qquad \textbf{4-39}$$

4.6   Non-Holonomic Constraints (NHCs)

Non-holonomic constraints refer the fact that unless the vehicle jumps off the ground or slides to the ground, the velocity of the vehicle in the plane perpendicular to the forward direction (x-axis) is almost zero.

For land vehicle, two non-holonomic constraints can be considered to aid inertial navigation system. Forward direction of land platforms usually aligned with the velocity vector unless the vehicle makes sharp turns. Therefore, a land platform can be approximated as a train on a rail. That is if the vehicle making its turns delicately then the velocity in the lateral direction (y-axis) can be taken as close to zero.
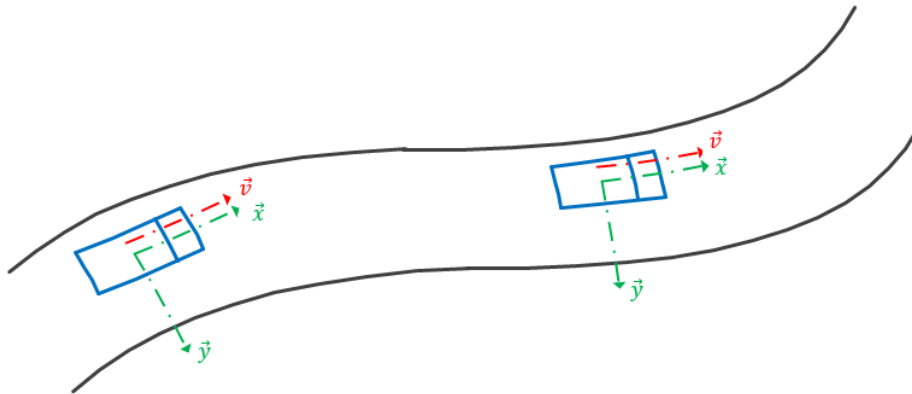
4.5 Lateral Motion Constaint 2D Sketch

As it can be imagined from the sketch given below, when the platform accelerates or decelerates, it will high likely experience a pitching motion. Thus, if the speed of vehicle is almost constant or not changing drastically, velocity in vertical direction (z-direction) can be taken close to zero. In order to obtain better visualization, z-axis is drawn vertically up which is contradicting with the vehicle body frame definition made in Chapter 2.
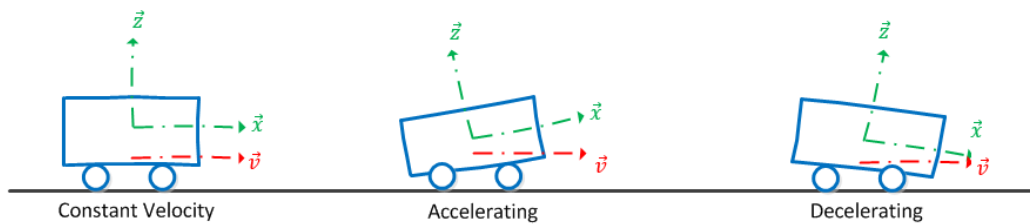
4.6 Vertical Motion Constaint 2D Sketch

Whole discussion aforementioned can be wrapped up as if the platform is not under high dynamic maneuvers and speed changes, two motion constraints can be accepted as a hypothetical velocity measurements.

4.6.1 Non-Holonomic Constraints Measurement Model

Non-holonomic constraints exploit the fact that the land vehicle generally moves in the forward direction. Movements such as jump, fall, side-slip etc. are quite uncommon.

$$\underline{z}_{ext} = v_{b/e,NHC}^{(b)} = \begin{bmatrix} ... \\ 0 + \eta_{v_{b/e,y,NHC}^{(b)}} \\ 0 + \eta_{v_{b/e,z,NHC}^{(b)}} \end{bmatrix} \tag{4-40}$$

For the expression below, IMU sensor coordinate axis is assumed to be aligned with the vehicle body axis.

$$\underline{\tilde{z}} = \tilde{v}_{b/e}^{(b)} = \tilde{C}_b^{n^T} \tilde{v}_{b/e}^{(b)} \tag{4-41}$$

$$\underline{\delta z}^* = \underline{z}_{ext} - \underline{\tilde{z}} = C_b^{n^T} v_{b/e}^{(n)} - \tilde{C}_b^{n^T} \underbrace{\tilde{v}_{b/e}^{(n)}}_{v_{b/e}^{(n)} + \delta v_{b/e}^{(n)}} = -C_b^{n^T} \delta v_{b/e}^{(n)} - C_b^{n^T} ssm(v_{b/e}^{(n)}) \partial \Psi_{b/n}^{(n)} \tag{4-42}$$

$$[\delta z] = [H][\delta x] + [\eta]$$

$$\begin{bmatrix} \delta z_1^* \\ \delta z_2^* \end{bmatrix} = \begin{bmatrix} H_{2x39}^* \\ H_{3x39}^* \end{bmatrix} [\delta x] + \begin{bmatrix} \eta_{v_{b/e,y,NHC}^{(b)}} \\ \eta_{v_{b/e,z,NHC}^{(b)}} \end{bmatrix} \tag{4-43}$$

4.7 Field Calibration of Inertial Sensor

Inertial sensor field calibration model is based on two different algorithmic process. First of all, the known magnitude of local gravity is exploited to compensate accelerometer triad error parameters under the name of primary calibration model. When the primary calibration is finished, the calibrated accelerometer triad readings are used as local gravity vector measurements. Lateron, the attitude computation algorithm which is actually readily avaliable as part of INS starts computing the body attitude. The gravity vector computed via attitude integration algorithm is discriminated with the compensated accelerometer measurements to estimate and calibrate the gyroscope triad errors in the name of secondary calibration model.

4.7.1 Primary Calibration Measurement Model

When the inertial measurement unit in static condition, the regardless of the orientation the total magnitude of accelerometer reading is ideally equals to magnitude of gravity. In other words, the primary calibration measurement model is use the known magnitude of local gravity to compensate accelerometer bias, scale factor and cross-coupling errors. Moreover, the stationary condition implies that total angular rate can be measured by gyroscope triad must equal to the Earth rotation rate. Therefore, as long as the inertial measurement unit remains in static condition, gyroscope bias and acceleration dependent bias error can be calibrated.

Figure 4.7 Representation of Local Gravity Vector and The Earth Rate

$$z_{ext} = |g_{local}| \qquad\qquad \textbf{4-44}$$

$$\tilde{z} = |\tilde{g}_{local}| = h(x_a + \delta x) \qquad\qquad \textbf{4-45}$$

By using first order Taylor approximation

$$\tilde{x}_a = x_a + \delta x \qquad\qquad \textbf{4-46}$$

$$h(\tilde{x}_a) = h(x_a + \delta x) = h(x_a) + \frac{\partial h(x_a)}{\partial \delta x} \delta x$$

$$h(x_a) = |\tilde{g}_{local}(x_a)| = \sqrt{\tilde{f}_{b/i,x}^{(b)\,2}(x_a) + \tilde{f}_{b/i,y}^{(b)\,2}(x_a) + \tilde{f}_{b/i,z}^{(b)\,2}(x_a)} \qquad\qquad \textbf{4-47}$$

The accelerometer triad error model equation given as expression (2.113) is substitude into the equation above.

$$\underline{\tilde{f}}_{b/i}^{(b)} = \underline{b}_a + (I_3 + S_a + M_a)\underline{f}_{b/i}^{(b)} + \underline{w}_a$$

$$\frac{\partial h(x_a)}{\partial b_{a,x}} = \frac{\tilde{f}_{b/i,x}^{(b)}(x_a)}{h(x_a)}, \quad \frac{\partial h(x_a)}{\partial S_{a,x}} = \frac{\tilde{f}_{b/i,x}^{(b)}{}^2(x_a)}{h(x_a)}, \quad \frac{\partial h(x_a)}{\partial M_{a,xy}} = \frac{\tilde{f}_{b/i,x}^{(b)}(x_a)\tilde{f}_{b/i,y}^{(b)}(x_a)}{h(x_a)} \qquad \textbf{4-48}$$

The measurement model can be formed as

$$\delta z = z_{ext} - \tilde{z} = H\delta x + \eta$$

$$\delta z_{P1} = |g_{local}| - h(x_a) - \frac{\partial h(x_a)}{\partial \delta x}\delta x = H_{P1}\delta x + \eta_{P1} \qquad \textbf{4-49}$$

$$H_{P1} = -\frac{\partial h(x_a)}{\partial \delta x} = \left[0_{1x9} \quad -\frac{\tilde{f}_{b/i,x}^{(b)}(x_a)}{h(x_a)} \quad -\frac{\tilde{f}_{b/i,y}^{(b)}(x_a)}{h(x_a)} \quad -\frac{\tilde{f}_{b/i,z}^{(b)}(x_a)}{h(x_a)} \quad 0_{1x3} \quad -\frac{\tilde{f}_{b/i,x}^{(b)}{}^2(x_a)}{h(x_a)} \quad \dots \right.$$

$$\left. \dots \quad -\frac{\tilde{f}_{b/i,y}^{(b)}{}^2(x_a)}{h(x_a)} \quad -\frac{\tilde{f}_{b/i,z}^{(b)}{}^2(x_a)}{h(x_a)} \quad -\frac{\tilde{f}_{b/i,x}^{(b)}(x_a)\tilde{f}_{b/i,y}^{(b)}(x_a)}{h(x_a)} \quad -\frac{\tilde{f}_{b/i,x}^{(b)}(x_a)\tilde{f}_{b/i,z}^{(b)}(x_a)}{h(x_a)} \quad -\frac{\tilde{f}_{b/i,y}^{(b)}(x_a)\tilde{f}_{b/i,z}^{(b)}(x_a)}{h(x_a)} \quad 0_{1x18} \right] \qquad \textbf{4-50}$$

Similar to the measurement model of absolute magnitude of local gravity, magnitude of the Earth rate is used as a measurement.

$$z_{ext} = |\Omega_{e/i}| \qquad \textbf{4-51}$$

$$\tilde{z} = |\tilde{\Omega}_{e/i}| = h(x_a + \delta x) \qquad \textbf{4-52}$$

By using first order Taylor approximation

$$\tilde{x}_a = x_a + \delta x$$

$$h(\tilde{x}_a) = h(x_a + \delta x) = h(x_a) + \frac{\partial h(x_a)}{\partial \delta x}\delta x$$

$$h(x_a) = |\tilde{\Omega}_{e/i}(x_a)| = \sqrt{\tilde{\omega}_{b/i,x}^{(b)}{}^2(x_a) + \tilde{\omega}_{b/i,y}^{(b)}{}^2(x_a) + \tilde{\omega}_{b/i,z}^{(b)}{}^2(x_a)} \qquad \textbf{4-53}$$

When the inertial measurement unit in static condition, following reductions can be performed. Since the Earth rate is so weak, for static conditions scale factor and cross-coupling errors arised in gyroscopes do not cause any substantial angular rate error when compared to bias error. Therefore, the reduction done in equation (4.54) is quite acceptable in stationary cases.

59

$$\underline{\tilde{\omega}}_{b/i}^{(b)} = \underline{b}_g + (I_3 + S_g + M_g)\underline{\omega}_{b/i}^{(b)} + G_g \underline{f}_{b/i}^{(b)} + w_g$$

$$\underset{Static\,Condition}{\Longrightarrow\Longrightarrow\Longrightarrow} \qquad \underline{\tilde{\omega}}_{b/i}^{(b)} \approx \underline{b}_g + \underline{\omega}_{b/i}^{(b)} + G_g \underline{f}_{b/i}^{(b)} + w_g \qquad \text{4-54}$$

$$\frac{\partial h(x_a)}{\partial b_{g,x}} = \frac{\tilde{\omega}_{b/i,x}^{(b)}(x_a)}{h(x_a)} \qquad \qquad \frac{\partial h(x_a)}{\partial G_{a,xx}} = \frac{\tilde{\omega}_{b/i,x}^{(b)}(x_a)\tilde{f}_{b/i,x}^{(b)}(x_a)}{h(x_a)} \qquad \text{4-55}$$

$$\delta z = z_{ext} - \tilde{z} = H\delta x + \eta$$

$$\delta z_{P2} = \left|\Omega_{e/i}\right| - h(x_a) - \frac{\partial h(x_a)}{\partial \delta x}\delta x = H_{P2}\delta x + \eta_{P2} \qquad \text{4-56}$$

$$H_{P2} = -\frac{\partial h(x_a)}{\partial \delta x} = \left[0_{1x12} \quad -\frac{\tilde{\omega}_{b/i,x}^{(b)}(x_a)}{h(x_a)} \quad -\frac{\tilde{\omega}_{b/i,y}^{(b)}(x_a)}{h(x_a)} \quad -\frac{\tilde{\omega}_{b/i,z}^{(b)}(x_a)}{h(x_a)} \quad 0_{1x18} \quad -\frac{\tilde{\omega}_{b/i,x}^{(b)}(x_a)\tilde{f}_{b/i,x}^{(b)}(x_a)}{h(x_a)} \quad \cdots \right.$$

$$\cdots \quad -\frac{\tilde{\omega}_{b/i,x}^{(b)}(x_a)\tilde{f}_{b/i,y}^{(b)}(x_a)}{h(x_a)} \quad -\frac{\tilde{\omega}_{b/i,x}^{(b)}(x_a)\tilde{f}_{b/i,z}^{(b)}(x_a)}{h(x_a)} \quad -\frac{\tilde{\omega}_{b/i,y}^{(b)}(x_a)\tilde{f}_{b/i,x}^{(b)}(x_a)}{h(x_a)} \quad -\frac{\tilde{\omega}_{b/i,y}^{(b)}(x_a)\tilde{f}_{b/i,y}^{(b)}(x_a)}{h(x_a)} \quad \cdots \qquad \text{4-57}$$

$$\cdots \quad \left. -\frac{\tilde{\omega}_{b/i,y}^{(b)}(x_a)\tilde{f}_{b/i,z}^{(b)}(x_a)}{h(x_a)} \quad -\frac{\tilde{\omega}_{b/i,z}^{(b)}(x_a)\tilde{f}_{b/i,x}^{(b)}(x_a)}{h(x_a)} \quad -\frac{\tilde{\omega}_{b/i,z}^{(b)}(x_a)\tilde{f}_{b/i,y}^{(b)}(x_a)}{h(x_a)} \quad -\frac{\tilde{\omega}_{b/i,z}^{(b)}(x_a)\tilde{f}_{b/i,z}^{(b)}(x_a)}{h(x_a)} \right]$$

$$[\delta z] = [H][\delta x] + [\eta]$$

$$\begin{bmatrix} \delta z_{P1} \\ \delta z_{P2} \end{bmatrix} = \begin{bmatrix} H_{P1} \\ H_{P2} \end{bmatrix}[\delta x] + \begin{bmatrix} \eta_{P1} \\ \eta_{P2} \end{bmatrix} \qquad \text{4-58}$$

4.7.2 Secondary Calibration Measurement Model

The secondary calibration is based on using the calibrated accelerometer signal from the primary calibration model to form gravity vector. The gravity vector obtained by attitude integration algorithm which is directly done via inertial navigation system attitude update part is compared with the reference gravity vector provided by the calibrated accelerometers. In other words, the gravity vector computed via calibrated accelerometers is used as a measurement to estimate gyroscope scale factor and cross-coupling errors.

$$\underline{z}_{ext} = \underline{g}_{local}^{(n)} = -\underline{f}_{b/i}^{(n)} = -C_b^n \underline{f}_{b/i}^{(b)} \qquad \text{4-59}$$

$$\underline{\tilde{z}} = -\tilde{C}_b^n \underline{\tilde{f}}_{b/i}^{(b)} \qquad \text{4-60}$$

Substitude expressions (2.60) and (2.65) into the above equation yields

$$\underline{\tilde{z}} = -(I_3 + ssm(\delta\underline{\Psi}_{b/n}^{(n)}))C_b^n \underline{\tilde{f}}_{b/i}^{(b)} \qquad \text{4-61}$$

The difference between the measurement and the equation (4.63) is given as

$$\underline{\delta z} = \underline{z}_{ext} - \underline{\tilde{z}} = -C_b^n \underline{f}_{b/i}^{(b)} + C_b^n \underline{\tilde{f}}_{b/i}^{(b)} + ssm(\delta\underline{\Psi}_{b/n}^{(n)})C_b^n \underline{\tilde{f}}_{b/i}^{(b)}$$
$$\underbrace{\Rightarrow\Rightarrow\Rightarrow}_{\substack{neglecting\,multiplication \\ of\,error\,terms}} \qquad \text{4-62}$$
$$\underline{\delta z} = C_b^n(\underline{\tilde{f}}_{b/i}^{(b)} - \underline{f}_{b/i}^{(b)}) - ssm(\underline{f}_{b/i}^{(n)})\delta\underline{\Psi}_{b/n}^{(n)}$$
$$\underline{\delta z} = C_b^n(\underline{b_a} + S_a \underline{f}_{b/i}^{(b)} + M_a \underline{f}_{b/i}^{(b)} + \underline{w_a}) - ssm(\underline{f}_{b/i}^{(n)})\delta\underline{\Psi}_{b/n}^{(n)}$$

If the primary calibration is done, the reduced equation can be approximated as

$$\underline{\delta z}_{reduced} \approx C_b^n \underline{w_a} - ssm(\underline{f}_{b/i}^{(n)})\delta\underline{\Psi}_{b/n}^{(n)} \qquad \text{4-63}$$

$$\underline{\delta z} = \underline{z}_{ext} - \underline{\tilde{z}} = H\delta x + \underline{\eta}$$

$$H_{reduced} = \begin{bmatrix} 0_{3x6} & -ssm(\underline{f}_{b/i}^{(n)}) & 0_{3x30} \end{bmatrix} \qquad \text{4-64}$$

4.8   Stationary Detection

The primary calibration and zero velocity update measurement models are purely depend on the detection of static conditions. For this purpose, the mean quadratic deviations of inertial sensors readings are used as static case detection filter. When the inertial measurement unit in is in stationary case, variance of both the accelerometer and gyroscope readings do not excess certain limits.

Empirical acceleration and angular rate thresholds are used to for this specific purpose. References such as [42], [43], and [44] illustrate practical uses of stationary detection methods.

$$\underline{\sigma_f} = \sqrt{\frac{1}{N} \sum_{k=1}^{N} \left(\left\| \underline{f_{b/i}^{(b)}} \right\| - \underline{\mu_f} \right)} \qquad \textbf{4-65}$$

$$\underline{\sigma_\omega} = \sqrt{\frac{1}{N} \sum_{k=1}^{N} \left(\left\| \underline{\omega_{b/i}^{(b)}} \right\| - \underline{\mu_\omega} \right)} \qquad \textbf{4-66}$$

Where μ is representing the moving average of inertial sensor data for N point data window.

CHAPTER 5

ASSESSMENT OF THE FIELD CALIBRATION VIA SIMULATION ANALYSIS

The integration algorithm stated in part 4 is developed in MATLAB Simulink environment together with trajectory generator and sensor models. The top level Simulink block diagram is given in the following figure with key explanations described in the Table 5.1.
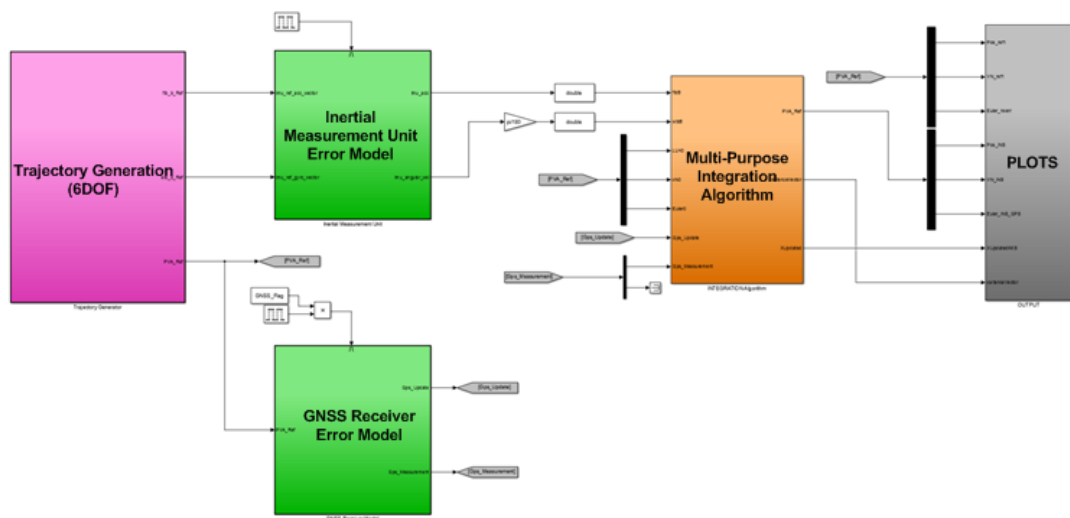
Figure 5.1 Top Level View of The Developed Simulation

Table 5.1 Simulation Block Description

Model Block Identifer	Explanations and Details
Trajectory Generation (Magenta Block)	Ideal error-free data of accelerometer and gyroscope triads are calculated together with error-free 6 DOF trajectory informations. The details are given in the appendix C.
Inertial Measurement Unit (Upper Green Block)	Ideal inertial sensors readings are deflected with error parameters given in Table 5.2 according expressions given in the part 2.5.
GNSS Receiver (Lower Green Block)	Three dimensional ideal linear position and velocity data generated via trajectory generation block is perturbed by error counter-part modelled as Gauss-Markov process and random walk respectively. The mathematical model of stochastic processes are highlighted in appendix B.
Multi-Purpose Intengration Algorithm (Orange Block)	The developed integrated algortihm which is detailly explained and formulated in chapter 4.
Results and Plots (Gray Block)	It is used as data comparison, record and some other trivial plot functions.

The simulated rotational trajectory is used as a reference signal to generate stimulus ideal inertial data. After a myriad of trials, the proposed calibration routine is simple rotation around all three axis of inertial measurement unit and the simulated sample ideal inertial signals are given below. Three simple rotation is simulated within in total 270 second and it is doubled in which the secondary calibration algorithm is used in the second part of the simulation while the primary calibration begins with the simulation. For both of the single and multi-run analysis, magnitude of local gravity is assumed to be perfectly known and no error model is established which is in fact not completely reflecting the real case.
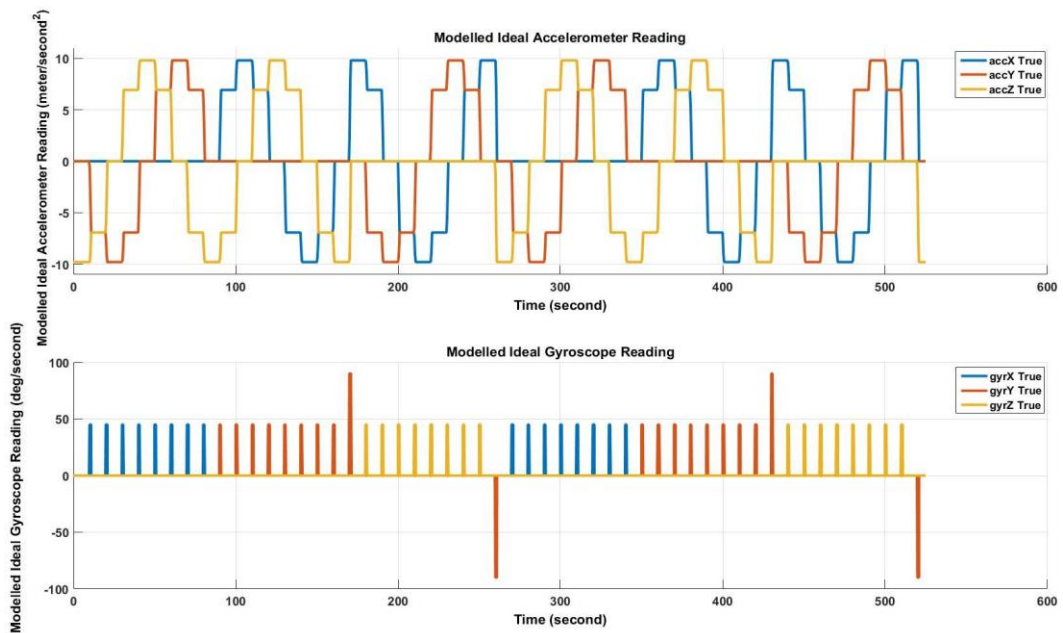
Figure 5.2 Simulated Ideal Accelerometer and Gyroscope Readings

The generated rotational trajectory is fed to inertial measurement unit model to simulate real inertial sensor data via applying sensor errors for two different grade of IMU which is tabulated in the Table 5.2. All values given in the Table 5.2 are modelled as 1 sigma (standard deviation).

Table 5.2 Simulated IMU Technical Specifications

		Automotive Grade IMU (Control-System Grade)	Tactical Grade IMU
Accelerometer Triad	Bias [mg]	50	1
	Scale Factor [ppm]	10000	300
	Misalignment (Cross-coupling) [mrad]	10	0.5

	Velocity Random Walk (VRW) [meter/s^2/sqrt(Hz)]	0.0083	0.0003302
Gyroscope Triad	Bias [degree/hr]	200	1
	Scale Factor [ppm]	10000	150
	Misalignment (Cross-coupling) [mrad]	10	0.5
	G-Dependent Bias [degree/hour/g]	100	-
	Angular Random Walk (ARW) [degree/sqrt(hr)]	0.500	0.125

Simulation study is carried out via a single run and multi-run (Monte-Carlo) analysis.

5.1   Single-Run Analysis

The developed algorithm is tested for its inertial sensor calibration feature in MATLAB environment via using automotive (commercial) grade IMU specifications. Square root of normalized variance of whole sensor error states are plotted and analyzed as a measure of algorithm convergence merit. The filter estimate of sensor errors are also plotted in the same figures to further clarify the performance of calibration.
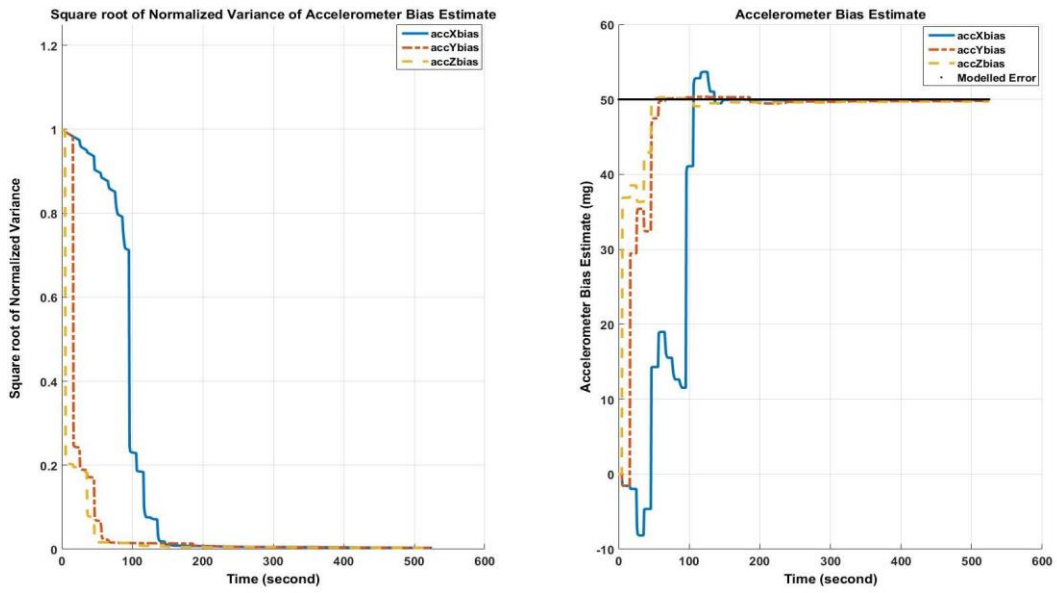
Figure 5.3 The Filter Accelerometer Bias Estimate and Its Square Root of Normalized Variance

As clearly seen from Figure 5.3 and Figure 5.4, the normalized variance of accelerometer triad bias and scale factor error estimates quickly fall below 10 percent of the inital uncertainty value within 150 second of simulation. That is, accelerometer triad bias and scale factor error estimates are reasonable close to the modelled value when three of whole accelerometer sensors at least a period of time pointing locally up and down.
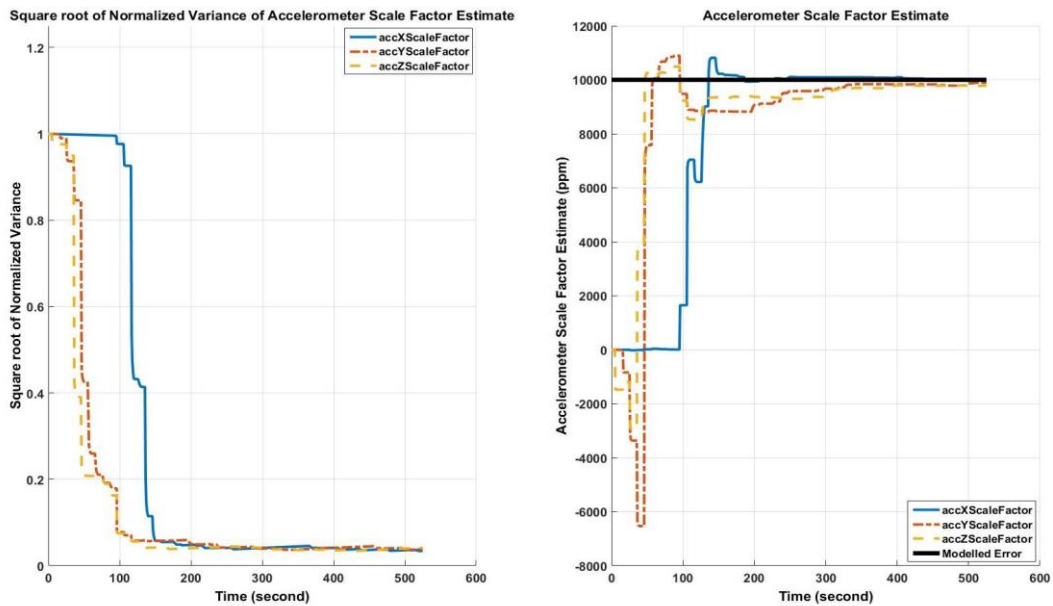
Figure 5.4 The Filter Accelerometer Scale Factor Estimate and Its Square Root of Normalized Variance

As the orientation of the accelerometer triad changes, the cross-coupling error estimates approaches the modelled ones which is given in the Figure 5.5. When the Figure 5.1 and Figure 5.5 are evaluated together, it is necessary to orient each of accelerometer sensitive axis to locally up and down more than several times to lower the uncertainity of integration filter cross-coupling error estimates. For accelerometer calibration, it can be clearly deduced from this single simulation analysis that as long as each axis of the accelerometer triad roughly aligned with the local up/down direction, the major part of bias and scale factor errors are estimated when the uncertainty of the estimate concerned. However, since the second order inertial sensor error sources are not modelled and the assumption of perfectly known gravity is made, there will be performance degradation when stepped outside from the simulation world.
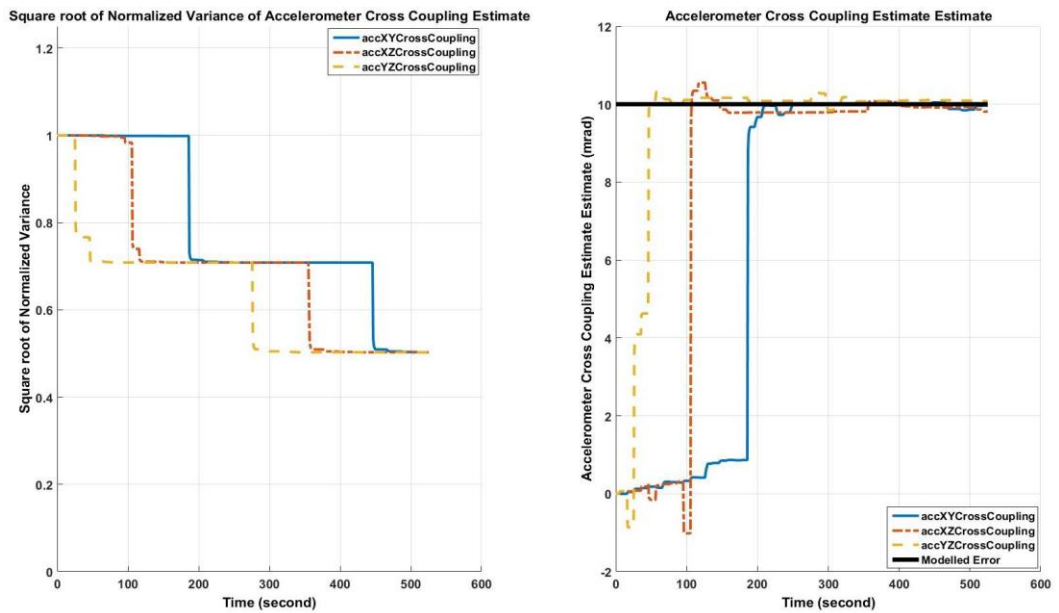
Figure 5.5 The Filter Accelerometer Cross Coupling Error Estimate and Its Square Root of Normalized Variance
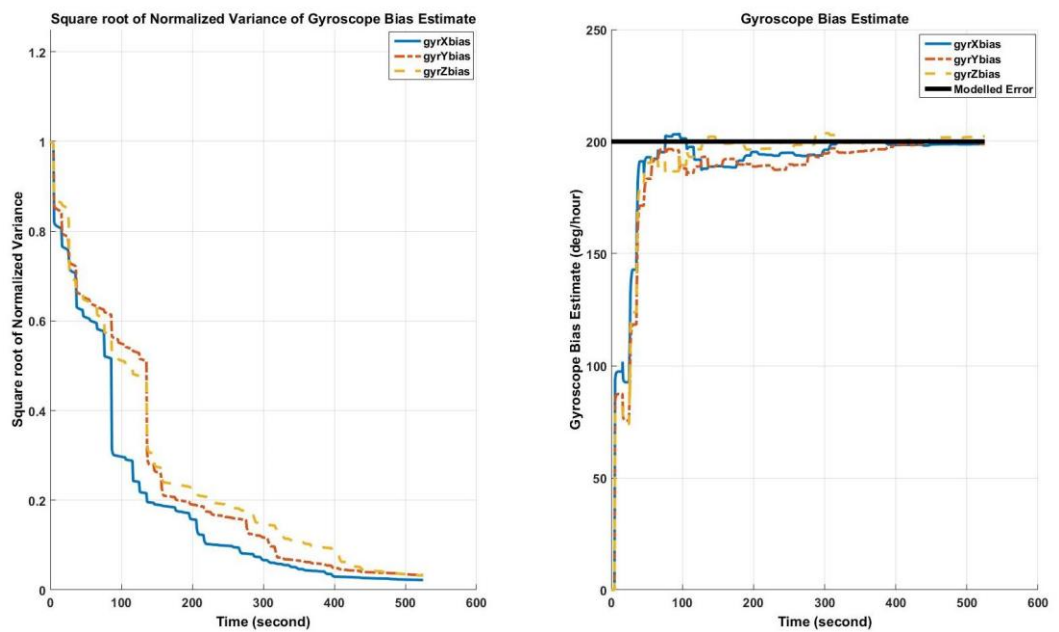
Figure 5.6 The Filter Gyroscope Bias Estimate and Its Square Root of Normalized Variance

For the gyroscope triad, bias and g-dependent bias error estimating process begin with the primary calibration algorithm which also begins with the simulation start

while scale factor and cross-coupling errors are estimated during the secondary calibration process. Both of bias and g-dependent bias terms are estimating all through the simulation length while it can be clearly seen from Figure 5.7 that scale factor error is directly observed when there is rotation around the related gyroscope unit. That is also true for the cross-coupling error estimates and their normalized variance values computed from integration filter.
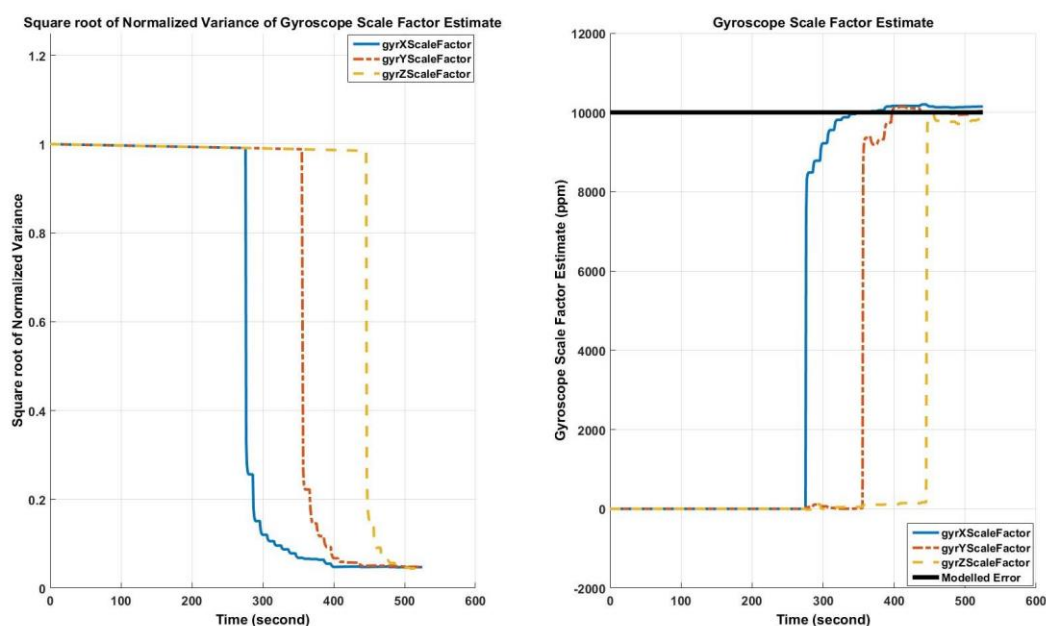
Figure 5.7 The Filter Gyroscope Scale Factor Estimate and Its Square Root of Normalized Variance

Figure 5.7 and figure 5.8 can be interpreted as the scale factor and the cross-coupling error estimations are high likely discriminated from each other by the estimation process.

70
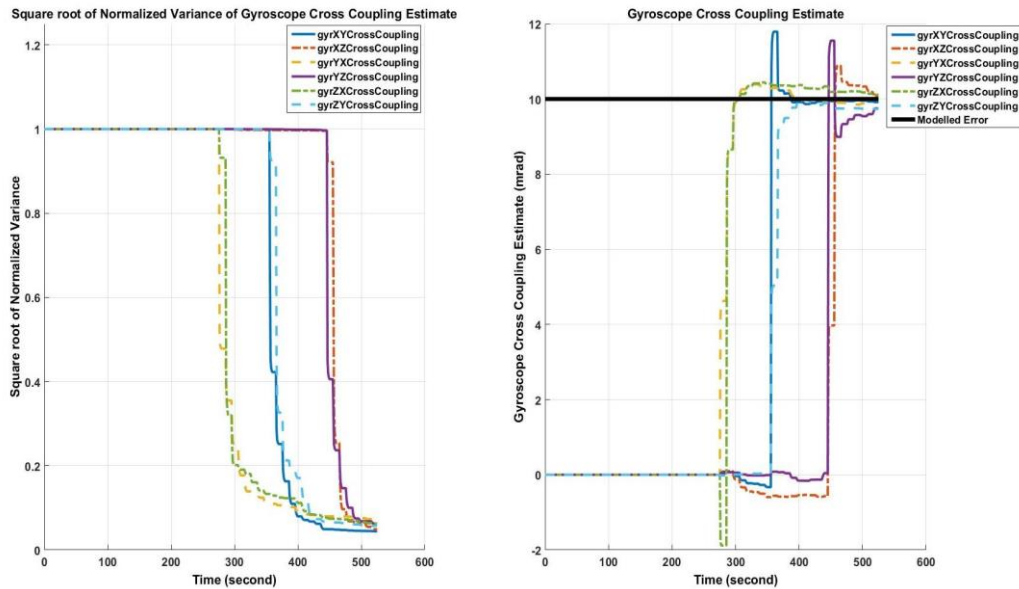
Figure 5.8 The Filter Gyroscope Cross Coupling Error Estimate and Its Square Root of Normalized Variance

Unlike to accelerometer case, the uncertainty of cross-coupling error estimate of gyroscope triad fall more than %10 of the initial value when a simple rotation is performed around each of the gyroscopes sensitive axis.
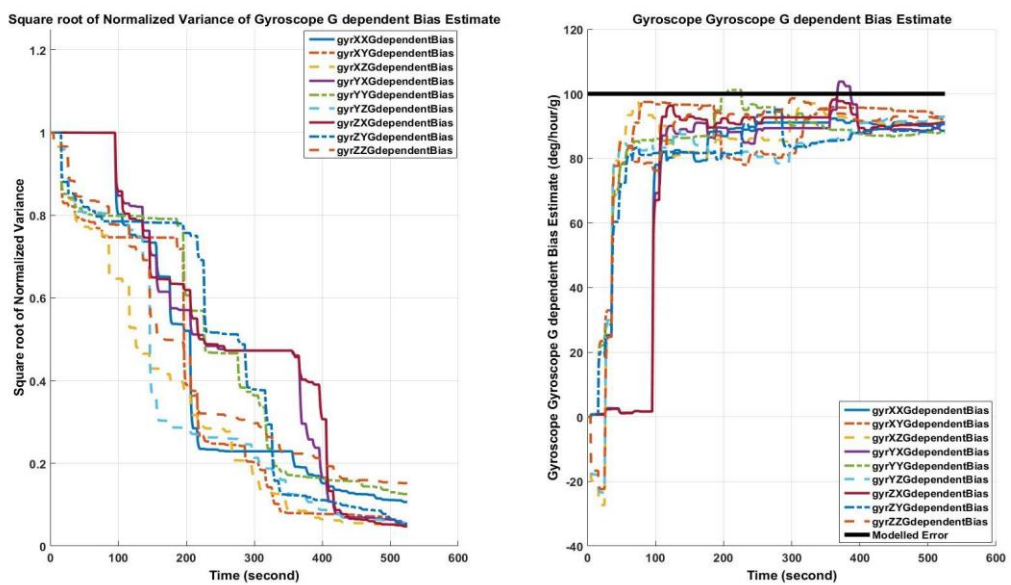
Figure 5.9 The Filter Gyroscope G-Dependent Bias Estimate and Its Square Root of Normalized Variance

71

Figure 5.10 is representing the modelled accelerometer triad and compensated accelerometer triad readings during the whole simulation. As it is highligted in the Figure 5.3 to Figure 5.5, obvious calibration result is obtained.
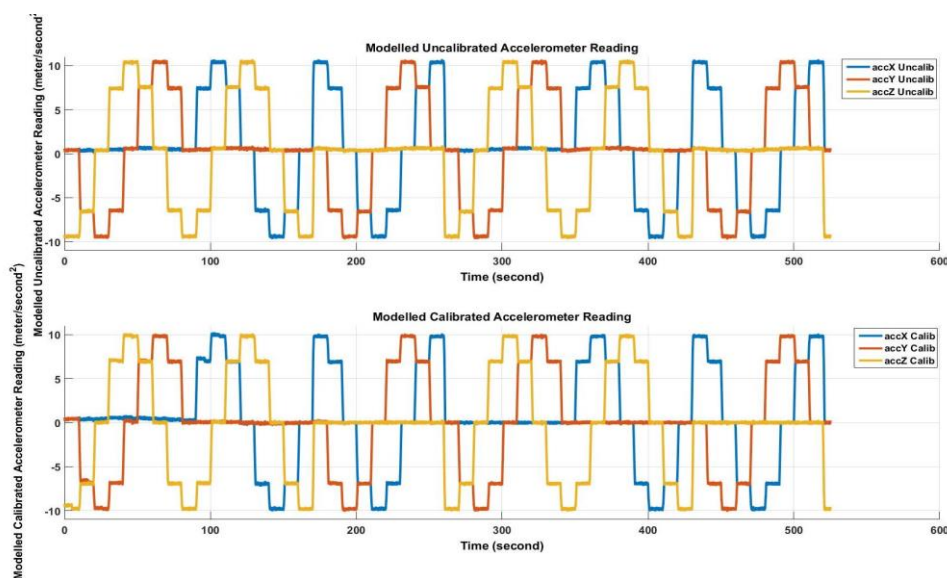
Figure 5.10 Simulated Uncalibrated and Calibrated Accelerometer Data

Examining the figures from 5.1 to figure 5.10 and wrapping up the single simulation analysis with simple rotational routine, the following outcomes can be deduced. Accelerometer triad:

- As long as the magnitude of local gravity is known accurate enough, major part of bias and scale factor errors are compensated effectively if all axis of sensor array point locally up/down direction at least a single time.

- Single simulation run indicates that cross-coupling error estimate may be improved further if the rotation routine is made with repeated action.

Gyroscope triad:

- Since the Earth rate is very weak signal especially for low grade gyroscopes, the noise in the sensor output becomes critical factor in the bias estimation process. Therefore, it can be pointed out that depending upon the sensor grade, noise suppressing techniques such as moving data average with emprically detected window size should be practiced.

-   It can be inferred from figure 5.7 and figure 5.8, if the bias terms of gyroscope triad compensated, scale factor and cross-coupling errors are effectively calibrated with a simple rotational process around the sensitive axis of calibration intended gyroscope.

5.2   Multi-Run Analysis

In order to generalize the performance of the algorithm in a statistical manner, multi-run analysis is carried out. The single run analysis stated in part 5.1 is repeated 1000 times for two different grades of inertial measurement unit. Besides, whole inertial sensor errors are normally distributed for each simulation run. When the simulations are finished, the histogram graphs of both of the modelled inertial sensor errors and residual terms left from calibration algorithm are plotted and the results are tabulated in this section.

In order not to pollute with a myriad of figures, only bias and scale factor errors of the x-axis of automotive grade inertial sensors plots are given below and the rest is listed in Appendix D.
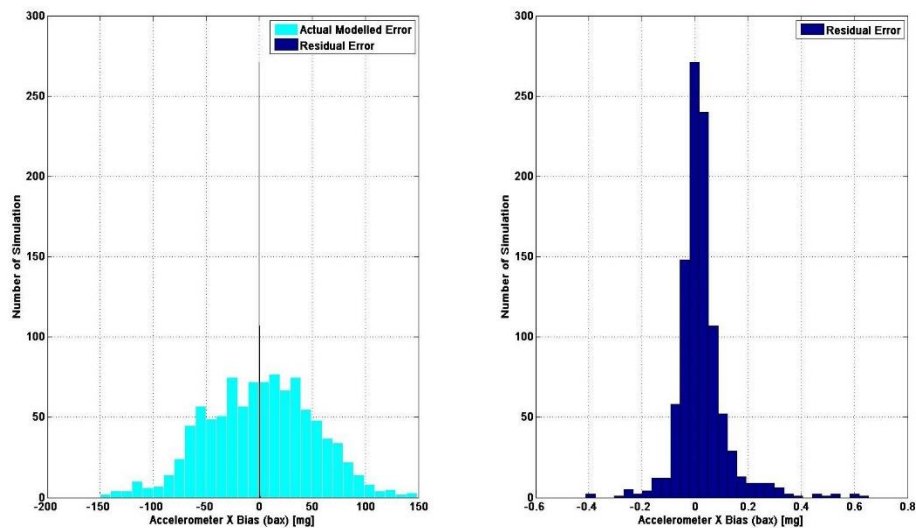
Figure 5.11 Automotive Grade X Accelerometer Modelled and Residual Bias Error
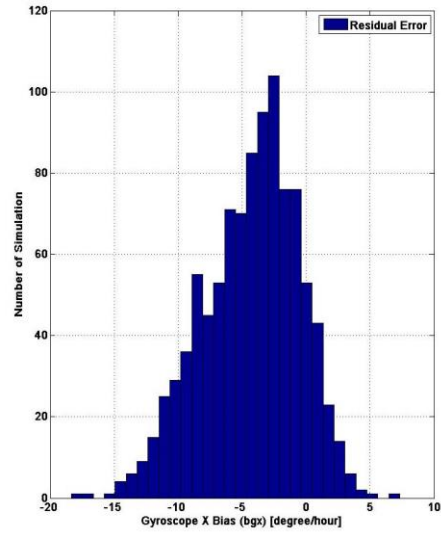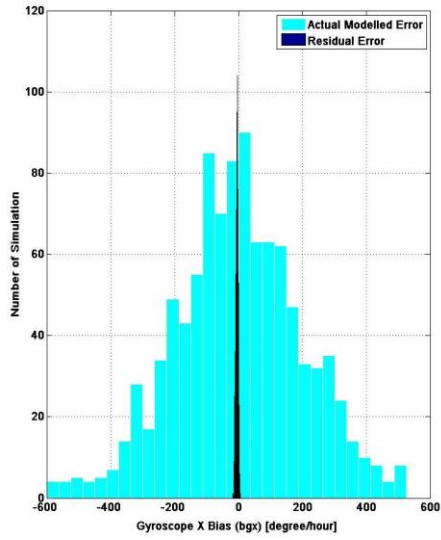
Figure 5.12 Automotive Grade X Gyroscope Modelled and Residual Bias Error
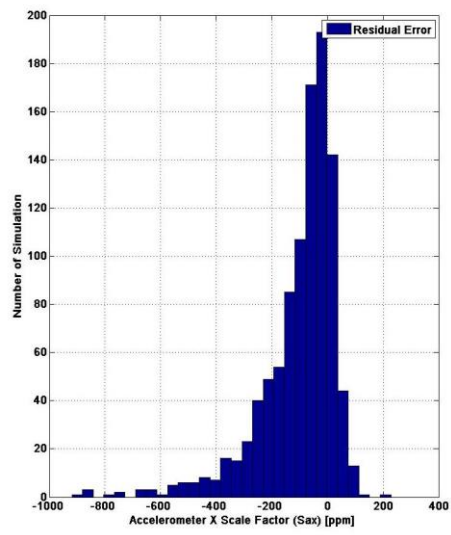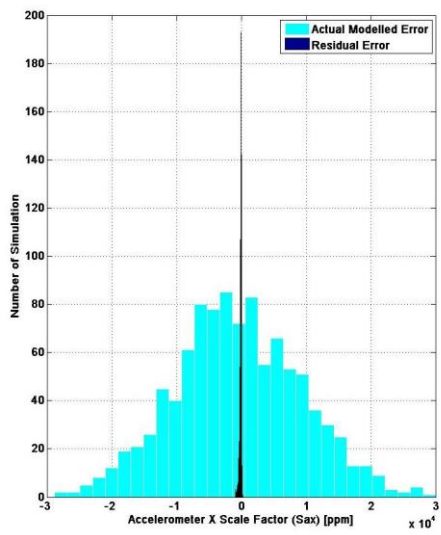
Figure 5.13 Automotive Grade X Accelerometer Modelled and Residual Scale Factor

74
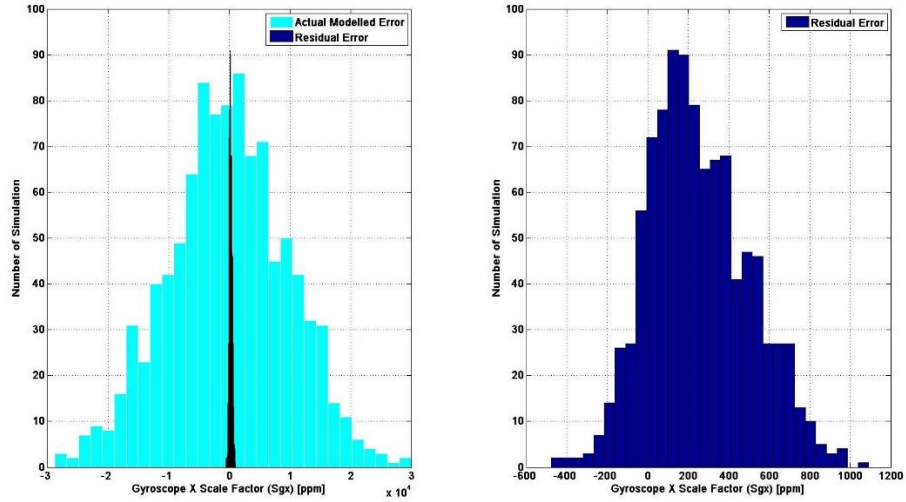
Figure 5.14 Automotive Grade X Gyroscope Modelled and Residual Scale Factor

The statistical results related to multi-run analysis are well tabulated in the following tables. In these tables, mean and standard deviation of modelled and residual error left from estimation process given.

Table 5.3 Multi-Run Analysis Results for Accelerometer Triad

			Automotive Grade IMU				Tactical Grade IMU			
			Modelled Error		Residual Error		Modelled Error		Residual Error	
			Mean	Std	Mean	Std	Mean	Std	Mean	Std
Accelerometer Triad	Bias	Bax [mg]	1.1456	50.924	0.0233	0.092	0.0229	1.0185	0.0000	0.0036
		Bay [mg]	-2.2110	49.186	0.0068	0.345	-0.0442	0.9837	0.0000	0.0038
		Baz [mg]	-2.3847	48.944	-0.0997	0.412	-0.0477	0.9789	-0.0001	0.0035
	Scale Factor	Sax [ppm]	-526.46	9836.7	-101.88	141.72	-15.794	295.101	0.0732	4.273
		Say [ppm]	43.70	10003.0	199.74	255.85	1.311	300.091	0.0498	4.446
		Saz [ppm]	393.31	9991.4	283.69	283.44	11.799	299.743	0.7189	4.067
	Misalignment (Cross-coupling)	Maxy [mrad/ (arcsec)]	0.4022 (81.44)	10.019 (2028)	-0.0017 (-0.344)	0.0553 (11.21)	0.0201 (4.072)	0.5010 (101.4)	-0.0006 (-0.115)	0.0076 (1.537)
		Maxz [mrad/ (arcsec)]	0.3494 (70.74)	10.205 (2066)	0.0341 (6.906)	0.1648 (33.37)	0.0175 (3.537)	0.5102 (103.3)	-0.0001 (-0.021)	0.0122 (2.479)
		Mayz [mrad/ (arcsec)]	0.1276 (25.85)	10.107 (2046)	0.0399 (8.099)	0.0914 (18.51)	0.0064 (1.293)	0.5054 (102.3)	-0.0001 (-0.191)	0.0197 (3.985)

For both of automotive and tactical grade IMUs, the accelerometer error estimates are quite match with the modelled values during multi-run simulations. Moreover, it can be seen from both Figure 5.11, Figure 5.13, accelerometer related figures in Appendix D and the table above, all of the accelerometer errors calibrated well and two to three orders of magnitude enhancement can be accomplished compared to the modelled sensor errors. Although the degree of improvement is nearly same for different grades of inertial sensors, there will be expectation for performance degradation in the estimation process for real cases due to the assumption of error-free gravity model. Since the main motivation of this work is more concentrated on the low cost inertial sensors, the well-known and commonly used gravity model such as normal gravity, J2, J4, etc. are quite adequete for the field calibration process. The reference [45] depicts comparison among the popular gravity models used commonly by navigation society. As it is highlighted in the references such as [46] and [47], the common form of simple gravity models such as ellipsoid gravity model differ from the actual gravity less around 100 mgal (approximately 0.1 mg) which is shown in gravity disturbance figures shown below . Gravity disturbance is defined as the difference between the actual gravity value for any arbitrary point on the Earth with the ellipsoid gravity model indicated value for the same location. As seen from the sample figures below, the gravity signal obtained from the ellipsoid gravity model is actually highly accurate reference signals for low cost, especially uncompensated accelerometers.
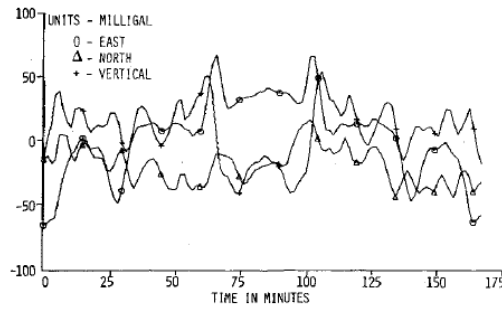
Inertial navigation gravity model error for ellipsoid gravity model.

Gravity disturbances on the trajectory of area 2.

Gravity disturbances on the trajectory of area 3.
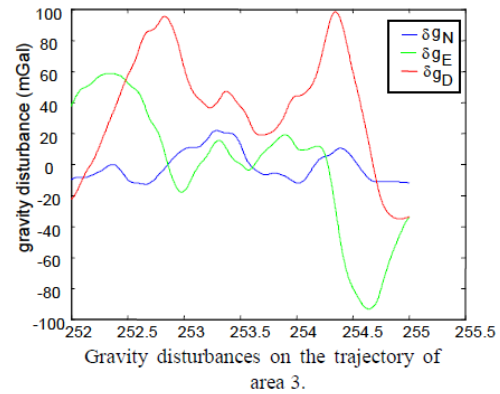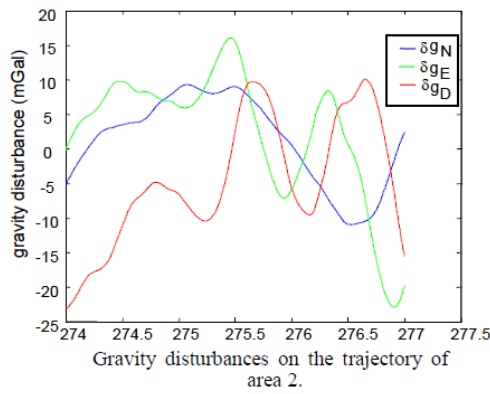
5.15 Gravity Disturbances Around Sample Trajectories (The Upper Figure is Adopted From [46] and The Lower Figures are Adopted From [47])

For gyroscope case, the field calibration algorithm results in nearly two order of magnitude enhancement for gyroscope main sensor errors except from g-dependent bias error for automotive grade typical uncompensated modelled gyroscope values. Acceleration dependent error of gyroscopes can be improved around an order of magnitude but as it is seen from Figure 5.9, further orientation change with repeated action to align the sensitive axis of each sensor inside the gyroscope triad with local down direction may increase the performance of estimation process. Besides from low grade inertial sensor, for tactical grade gyroscope specifications several order of magnitude increase in scale factor and cross-coupling errors can be seen from Table 5.4 which can be also seen from the figures given in Appendix D. Apart from scaling errors the bias error estimate of tactical grade gyroscope can be improved about several times better than the modelled error in which the noise level of gyroscope signal becomes the limiting factor. The gained experience from simulation studies indicate that in order to obtain better estimation performance for

especially gyroscope bias error, long period of averaging time becomes necessary to suppress the noise effect of sensor signal. In other words, moving from low grade gyroscope to high grades toward navigation grade and further, the averaging time for bias estimation proportionally increase the duration of field calibration process.

Table 5.4 Multi-Run Analysis Results for Gyroscope Triad

			Automotive Grade IMU				Tactical Grade IMU			
			Modelled Error		Residual Error		Modelled Error		Residual Error	
			Mean	Std	Mean	Std	Mean	Std	Mean	Std
Gyroscope Triad	Bias	Bgx [°/hr]	-0.2201	198.66	-4.3182	3.787	-0.0011	0.9933	-0.0131	0.2329
		Bgy [°/hr]	4.8621	195.94	0.8005	4.768	0.0243	0.9797	0.0223	0.4874
		Bgz [°/hr]	-4.3174	201.7	-3.5579	3.680	-0.0216	1.0085	-0.0158	0.2417
	Scale Factor	Sgx [ppm]	-217.79	9850.2	253.19	248.85	-3.2668	147.753	0.6285	17.744
		Sgy [ppm]	-253.30	9401.4	-43.09	276.08	-3.5296	141.021	-1.5150	28.165
		Sgz [ppm]	-86.719	10069	219.48	237.11	-1.3008	151.040	0.7212	18.821
	Misalignment (Cross-coupling)	Mgxy [mrad/ (arcsec)]	0.3176 (64.32)	10.123 (2050)	0.2525 (51.13)	0.2262 (45.80)	0.0159 (3.216)	0.5062 (102.5)	0.0005 (0.107)	0.0205 (4.150)
		Mgxz [mrad/ (arcsec)]	-0.0717 (-14.53)	10.143 (2053)	0.2443 (49.48)	0.2659 (53.85)	-0.0036 (-0.726)	0.5071 (102.7)	0.0020 (0.407)	0.0235 (4.749)
		Mgyx [mrad/ (arcsec)]	-0.6554 (-132.7)	9.867 (1998)	-0.1323 (-26.79)	0.3864 (78.23)	-0.0328 (-6.636)	0.4934 (99.9)	-0.0027 (-0.545)	0.0382 (7.733)
		Mgyz [mrad/ (arcsec)]	-0.2942 (-59.57)	9.900 (2005)	0.0272 (5.504)	0.3231 (65.43)	-0.0147 (-2.978)	0.4950 (100.2)	-0.0014 (-0.285)	0.0371 (7.521)
		Mgzx [mrad/ (arcsec)]	-0.2824 (-57.18)	10.503 (2127)	0.2372 (48.02)	0.3022 (61.19)	-0.0141 (-2.859)	0.5251 (106.3)	0.0015 (0.311)	0.0250 (5.068)
		Mgzy [mrad/ (arcsec)]	-0.3198 (-64.75)	10.126 (2050)	0.1394 (28.22)	0.2313 (46.85)	-0.0160 (-3.238)	0.5063 (102.5)	0.0010 (0.196)	0.0210 (4.258)
	Gyroscopes Acceleration Dependent Error	Ggxx [°/hr/g]	2.570	91.388	-8.424	5.645	-	-	-	-
		Ggxy [°/hr/g]	0.144	92.356	0.233	3.650	-	-	-	-
		Ggxz [°/hr/g]	-4.756	90.891	0.695	3.560	-	-	-	-
		Ggyx [°/hr/g]	0.083	91.034	-0.538	2.984	-	-	-	-
		Ggyy [°/hr/g]	0.747	88.295	-6.639	7.297	-	-	-	-
		Ggyz [°/hr/g]	-2.808	89.164	0.371	4.206	-	-	-	-
		Ggzx [°/hr/g]	-4.547	89.792	-0.443	2.587	-	-	-	-
		Ggzy [°/hr/g]	-3.494	89.372	-0.092	3.728	-	-	-	-
		Ggzz [°/hr/g]	1.070	90.745	-7.459	7.732	-	-	-	-

78

CHAPTER 6

FIELD TESTS

Outcomes of the simulation studies defined in chapter 5 are quite promising and thus application of the simulated work becomes necessary for further clarification. Therefore, field tests are carried out by using very low cost equipment which is described in part 6.1 to fortify the theoretical work and developed algorithm in terms of both field calibration feature and inertial navigation system aiding modes other than GNSS receiver. The reason of using cheap inertial measurement unit comes from the fact that it is overlapping with the main motivation of this research which is calibration of the low cost inertial sensor on the field. On top of that, during the field tests non-GPS/GNSS aid mode which is referred to combination of ZUPT and NHCs is tested as well.

6.1   Test Hardware and Equipment

Hardwares used in testing process include Ardupilot APM 2.5 for IMU labeled as MPU 6000 onboard and Ublox M8N as a GPS receiver. During both static and dynamic tests, both of the inertial sensors and GPS receiver data are recorded in flash memory of Ardupilot which is later on exported to personal computer. The exported data is post-processed in MATLAB environment. Besides, the power input of the APM unit is supplied from labtop USB COM port via mini USB interface cable.

Table 6.1 Main Test Hardware

Inertial Measurement Unit	Arduino, ArduPilot (APM 2.5) = 25 $
	
	- MPU 6000 Evaluation Board
	
	    ➤ 3 Axis Gyroscopes
	    ➤ 3 Axis Accelerometers
	    ➤ 3 Axis Magnetometers
		
		Figure 6.1 Ardupilot APM 2.5

GPS Receiver	Ublox M8N = 30 $	 **Figure 6.2 Ublox M8N GPS Receiver**

In order to establish field calibration procedure with the proposed rotational process that is dealt with during simulation study, low cost fixture is built from furniture connection parts from local store around 5 $ cost. The calibration fixture is actually assembled from four "L" shape and a flat aluminum furniture connection parts which are bolted together. The unit under test is sticked to the flat surface with double sided tape.
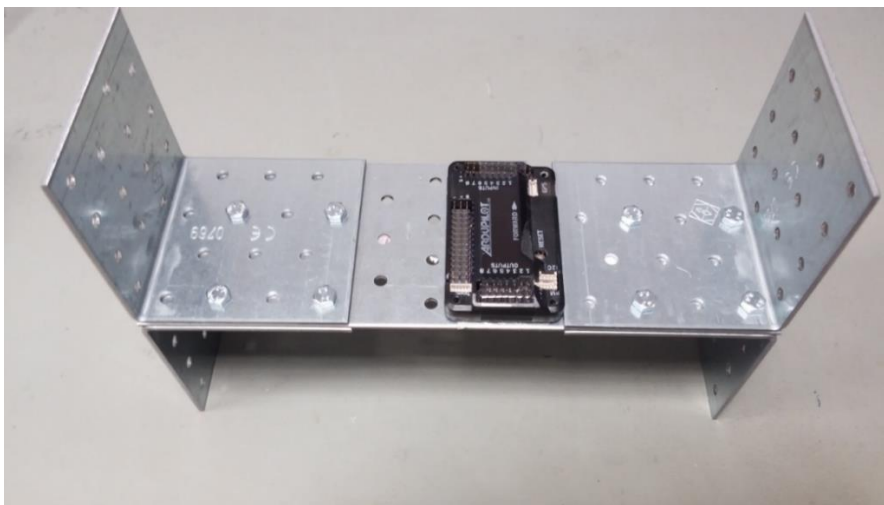
Figure 6.3 Low-Cost Calibration Fixture

Apart from MPU 6000 inertial measurement unit which is built in ArduPilot APM 2.5 card, two different relatively costly IMUs compared to APM undergo the same field calibration routine to assess the performance gain for various inertial sensor hardware. The inertial sensors data are collected from those units via the connector/cable and necessary software which are supplied in the related development kit.

VectorNav VN-200 = 2600 $ (GPS integrated INS)	Xsens Mti-G-710 = 3800 € (GPS integrated INS)
Figure 6.4 VN-200 with Calibration Fixture	**Figure 6.5 Mti-G-710 with Calibration Fixture**
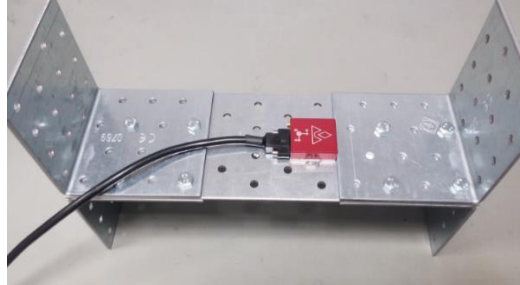
6.2 Field Calibration Process and Performance Tests

After the simulation studies related to the field calibration algorithm, orientation procedure mainly consists of three simple rotation around each of the IMU sensor axes.

The proposed simple rotation based calibration process is given in the following figure. In other words, the handmade calibration fixture is rotated at roughly around 45 degrees orientation poses around all three of the IMU in which each of the inertial sensors at least rotated once around the axis perpendicular to locally up/down direction. The calibration process is repeated for three different IMUs described in the previous section.
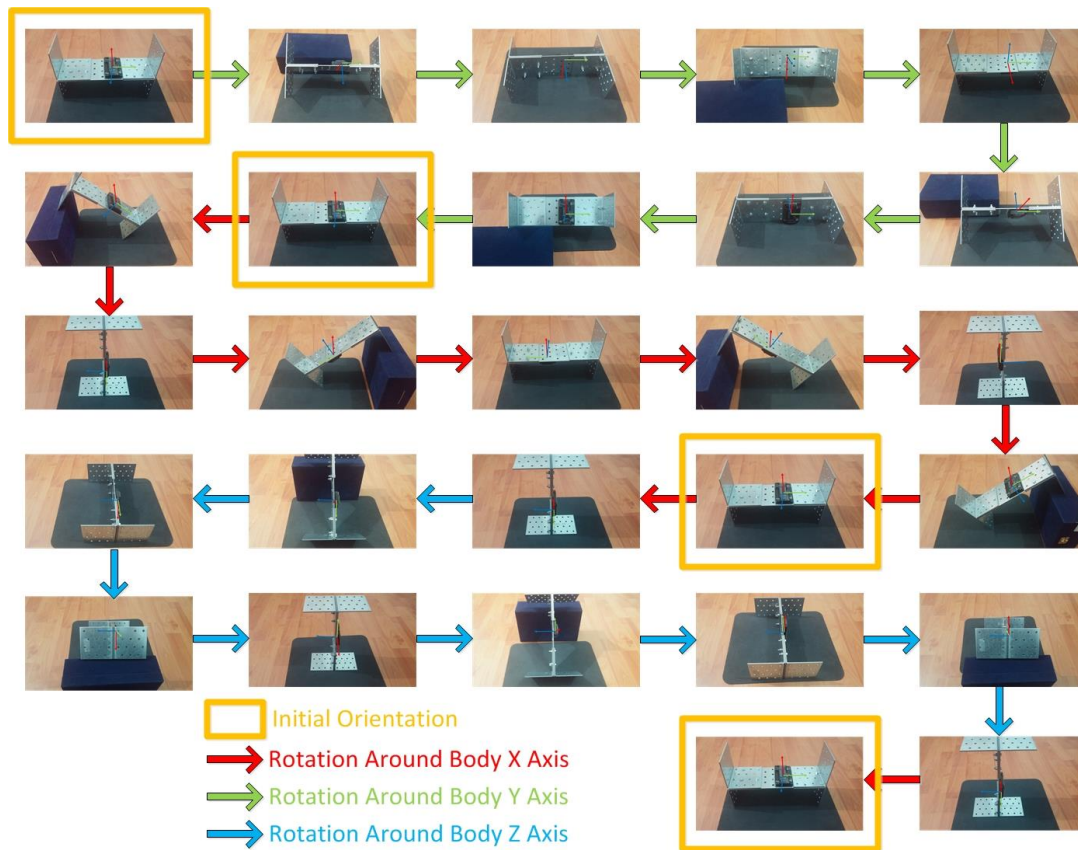
Figure 6.6 Calibration Routine

6.2.1 Static Tests

6.2.1.1 Ardupilot MPU-6000 Case

The above calibration routine given in the Figure 6.6 is based upon simple orthogonal rotation from all three axis of inertial sensors. The logged data from three different inertial measurement units are post processed with the developed algorithm. Later on, the calibrated and uncalibrated inertial sensor readings are fed into inertial mechanization equations which is inherently built in the integrated algorithm to see whether the field calibration process increase the navigation performance. The initial position is taken from GPS measurement and the initial attitude information is obtained from accelerometer levelling. The levelling process is given in the references [48], and [49].

The calibrated and uncalibrated raw readings from ArduPilot accelerometer are given in the following figure.
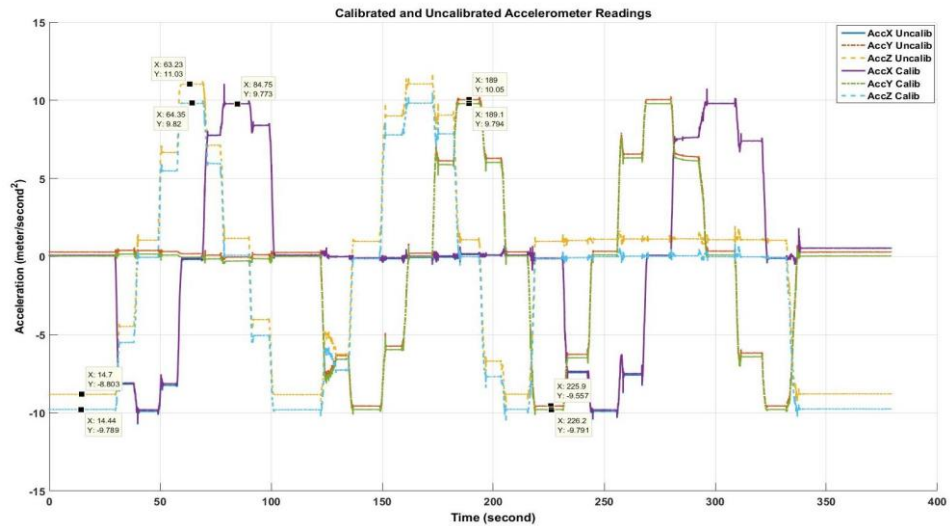
Figure 6.7 Ardupilot MPU-6000 Calibrated and Uncalibrated Accelerometer Data

The horizontal and vertical positioning errors are plotted for raw inertial sensor readings, only gyroscope calibrated and full calibrated inertial sensor readings.

As it can be seen from figure below, the accelerometer errors are the dominant source of the positioning error. From Figure 6.7, it is crystal clear to notice that around 100 mg misreading of gravity magnitude in accelerometer-z sensor which in turn leading to more than a km vertical positioning error under just 60 seconds.
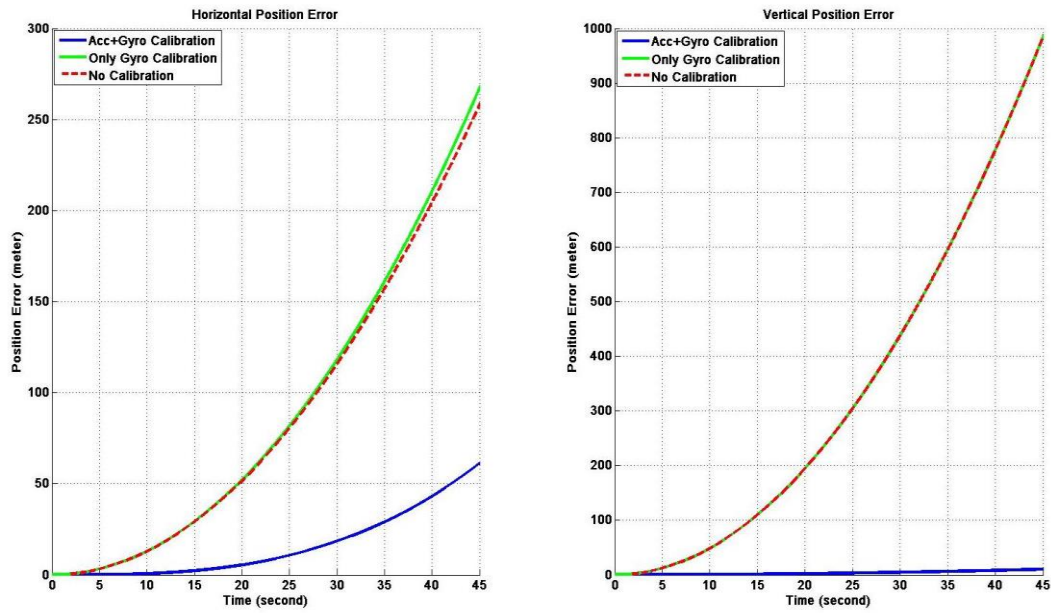
Figure 6.8 Ardupilot MPU-6000 Horizontal and Vertical Positioning Error

6.2.1.2 VN-200 Case

The same test is carried out for both of the VN-200 and Mti-710-G units. Calibrated and uncalibrated raw accelerometer readings of VN-200 are given below.
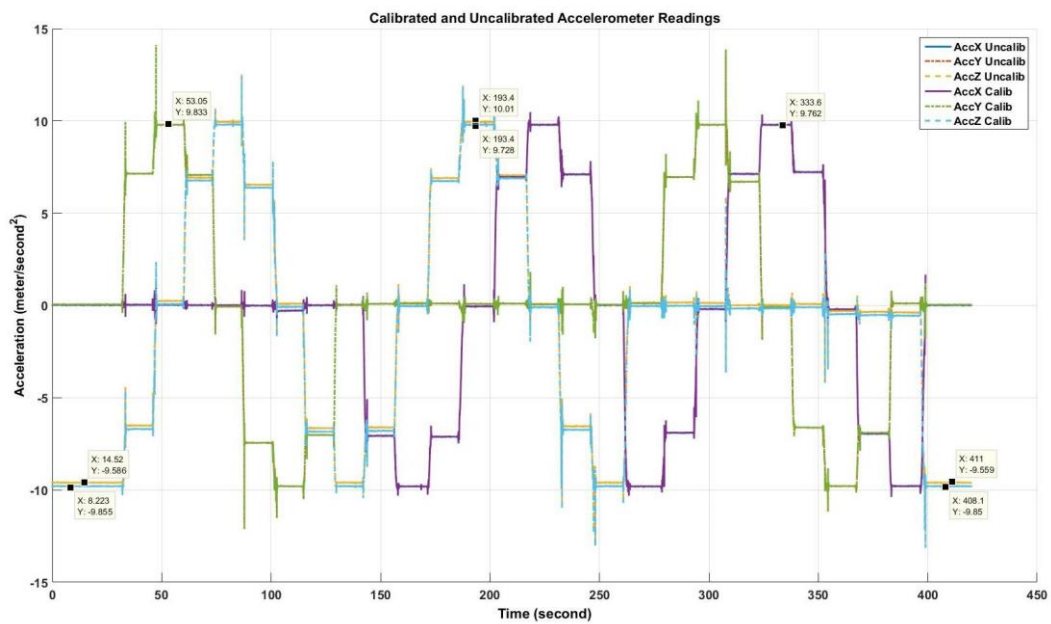
Figure 6.9 VN-200 Calibrated and Uncalibrated Accelerometer Data

Calibrated and uncalibrated raw gyroscope readings of VN-200 are given below. The gyroscope data before calibration and the calibrated gyroscope data are plotted only for VN-200 case because of the fact that the high amount of angular rate bias error in sensor readings which is obviously illustrated in the figure below. Although the bias error of gyroscope-z is around 1 degree per second level, it does not cause static positioning error due to fact that it is responsible for heading angle error acumulation. However, comparably high amount of angular rate bias error in one of the horizontal gyroscope cause main portion of horizontal positioning error shown in the Figure 6.11.
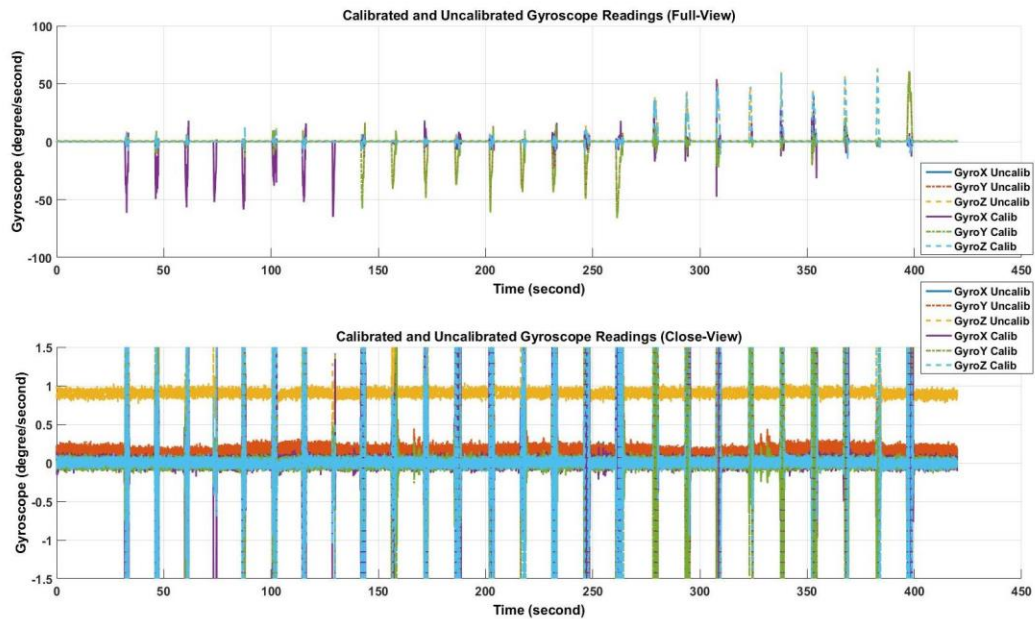
Figure 6.10 VN-200 Calibrated and Uncalibrated Gyroscope Data
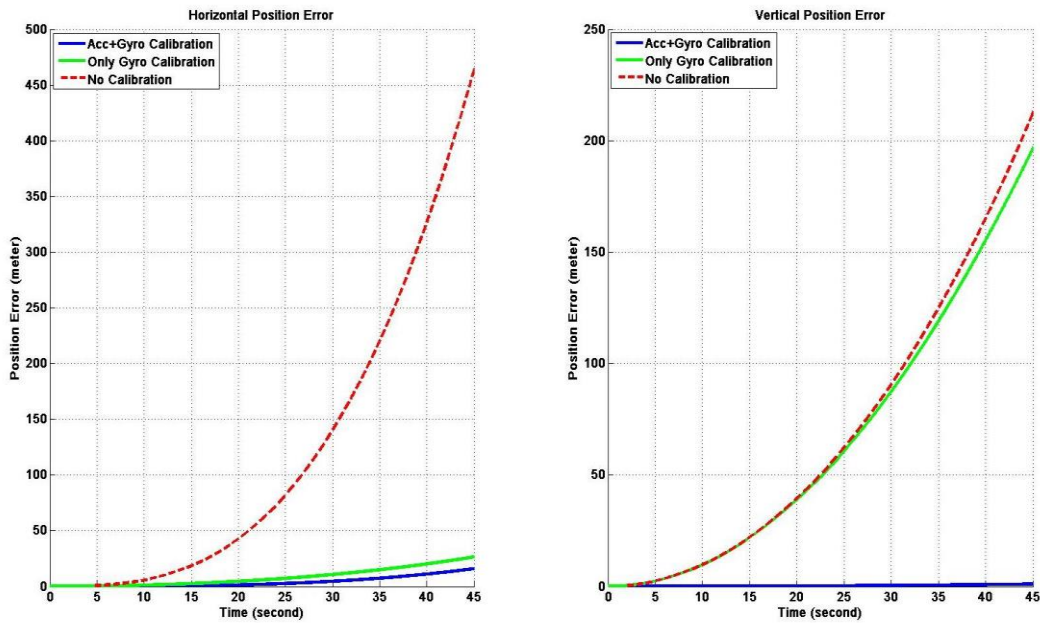
Figure 6.11 VN-200 Horizontal and Vertical Positioning Error

6.2.1.3 Mti-710G Case

The same field calibration attitude orientation routine given in the Figure 6.6 is applied to Mti-710-G as well and the positioning error graphs are given below. The results are quite similar to VN-200 case which is the main sources of static positioning error of pure inertial navigation system solution induced by bias error of gyroscopes in the horizontal plane.
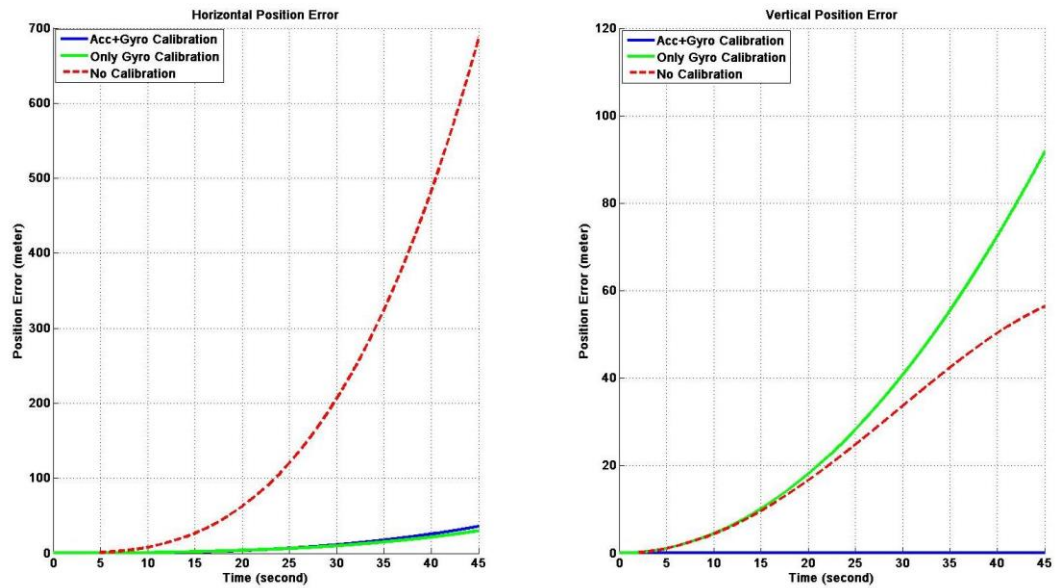
Figure 6.12 Mti-710G Horizontal and Vertical Positioning Error

Static tests conducted with three different MEMS IMU and more than an order of magnitude of positioning accuracy gain is achieved via field calibration process. That is, the field calibration orientation routine rotated to arbitrary angles by hand demonstrate its effectiveness in static positioning performance which is in fact directly related to how well inertial sensor errors are compensated.

6.2.2 Dynamic Tests

In addition to static tests applied for various inertial measurement units, dynamic test for land vehicle application is taken into consideration. Integration with GPS receiver and aiding modes other than GPS receiver are tested during dynamic tests. Both of ArduPilot and the GPS receiver mounted on the main part of the calibration fixture that are sticked to the dashboard of a car.

Figure 6.13 Dynamic Test Hardware and Dashboard View 1

Figure 6.14 Dynamic Test Hardware and Dashboard View 2

The dynamic test process is done for two different trajectory in Elmadag which is one of the state of Ankara. The mentioned trajectories are plotten from the data obtained by Google Earth application. During the dynamic tests, the data obtained from ArduPilot inertial sensor readings and uBlox GPS receiver data are fed to the developed integrated algorithm while various form of aiding modes are active. Besides that, intensional GPS receiver track losses are created to further investigate the performance increase with algorithm aiding modes.
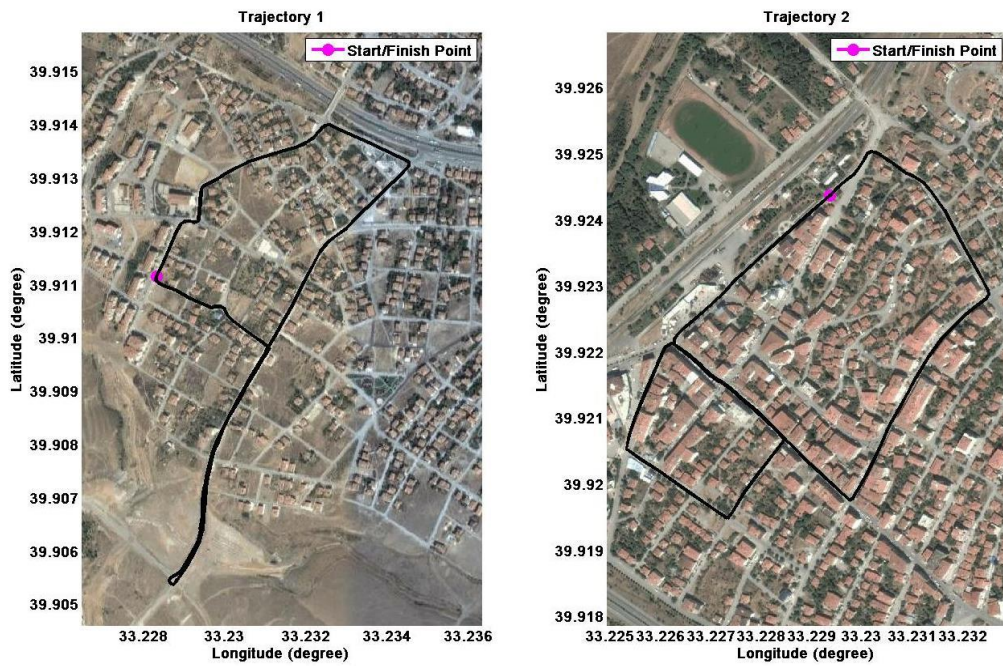
Figure 6.15 Dynamic Test Trajectories

6.2.2.1 Trajectory 1

The 2D/3D positioning, NED velocity and Euler angles calculated from the integrated algorithm with various forms of algorithm modes are given in the Figure 6.16 to Figure 6.20.
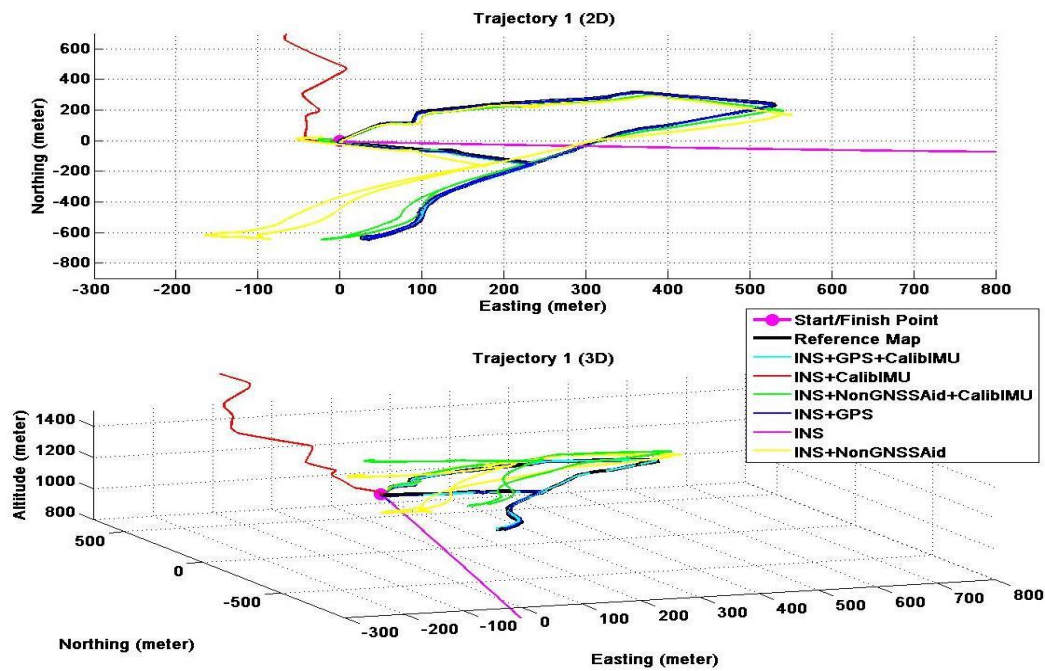
Figure 6.16 Trajectory 1, 2D-3D Position Data

As it is previously seen from the static tests highligted in part 6.2.1.1, errors in uncompensated inertial sensor especially accelerometers cause so called "garbage" navigation velocity and positioning solution which is obviously indicated in the velocity comparison plot given below. The field calibration algorithm remedies especially for vertical channel navigation accuracy illusturated in the Table 6.2 with several orders of magnitude increase in positioning and velocity solution accuracy. However, whether or not the field calibration is done, the navigation accuracy obtained is not enough and the stand alone INS solution cannot be used for long period of time. On the other hand the non-GNSS abbreviated as "NG" aiding modes highly increase the accuracy of navigation outputs which is tabulated in the Table 6.2 and the performance increase is also seen from the Figure 6.16 and Figure 6.17. Together with the inertial sensor field calibration procedure, the "NG" aiding results in below 20 meter horizontal positioning and below 80 meter vertical positioning accuracy within nearly 10 minutes of typical land vehicle test scenerio in urban environment.
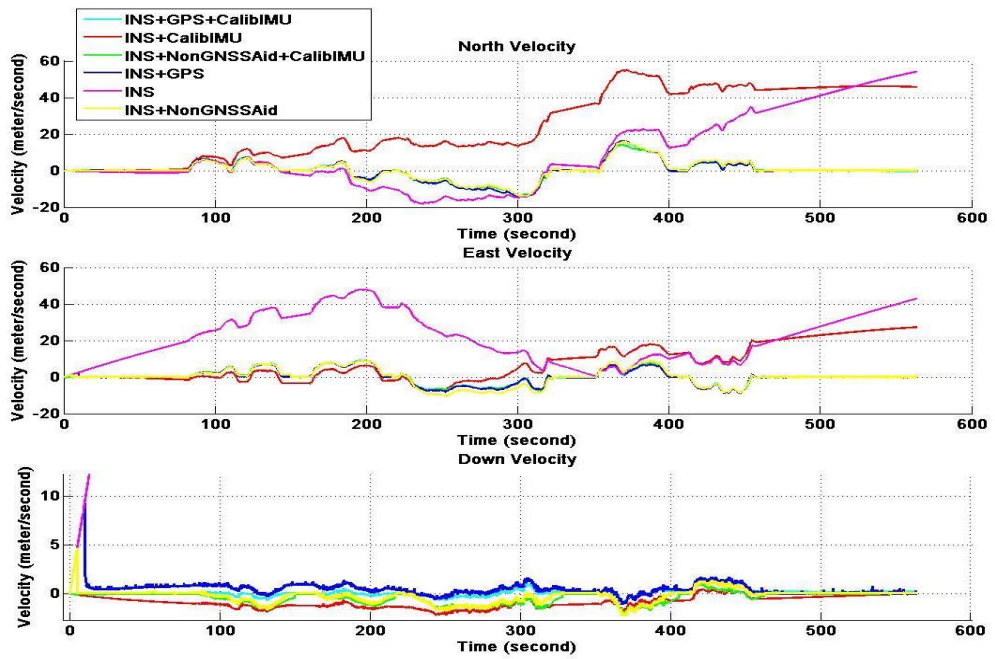
Figure 6.17 Trajectory 1, NED (North-East-Down) Velocity Data
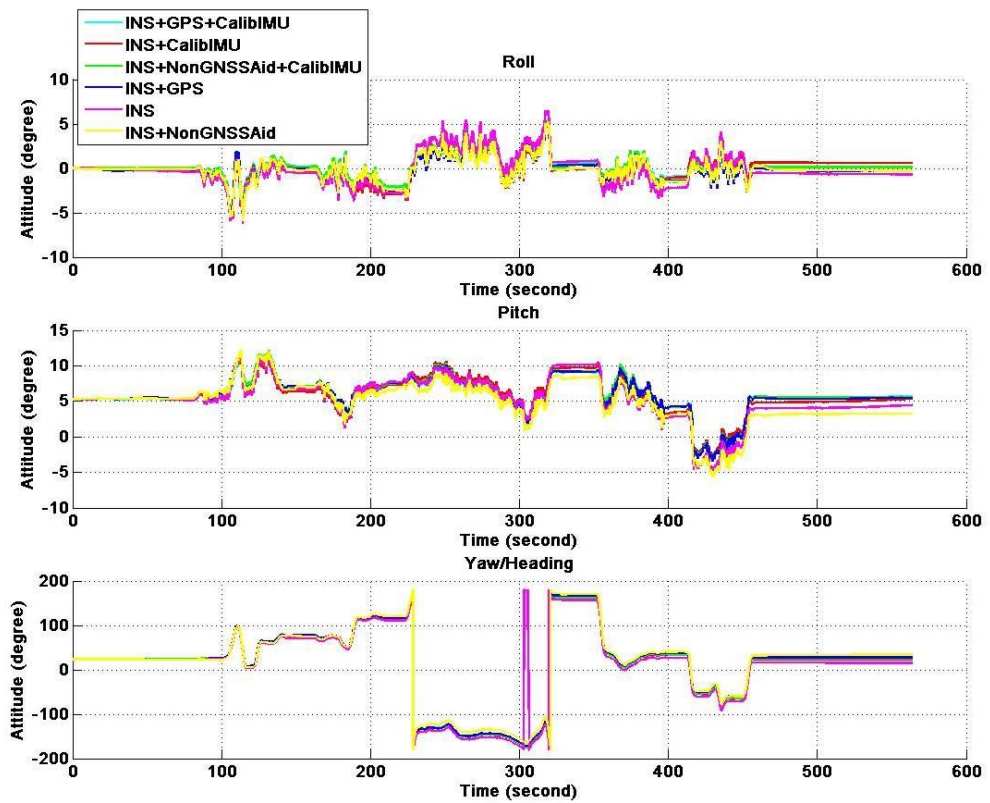
Figure 6.18 Trajectory 1, Euler Angle Data

Performance table belongs to whole test scenerios related to trajectory 1 is given below. The Figure 6.19 and Figure 6.20 is representing the positioning solution performance of integrated algorithm with different types of algorithm modes while the GPS receiver aid is inactive. The power of field calibration algorithm is straightforwardly distinguished from Figure 6.20 that is the more than an order of magnitude increase in performance is achived. Apart from the field calibration process, the non-GNSS aid modes also yield the similar performance gain with the short term pure inertial solution obtained from the field calibrated inertial sensors.

Table 6.2 Trajectory 1 Navigation Performance Table

	GPS Aid	Operational Modes	Position Accuracy (meter)		Velocity Accuracy (meter/second)		Rotational Accuracy (degree)
			Horizontal	Vertical	Horizontal	Vertical	Roll / Pitch / Yaw
Trajectory 1	None	INS+CIMU	6188.15	315.94	37.64	1.06	0.49 / 0.52 / 2.49
	None	INS+CIMU+NG	18.33	71.94	0.69	0.43	0.19 / 0.30 / 1.75
	None	INS	6978.13	71771.49	32.21	343.22	0.80 / 0.96 / 7.73
	None	INS+NG	66.27	101.90	1.35	0.61	0.34 / 1.34 / 4.38
	Full	INS	1.61	4.19	0.37	0.87	0.31 / 0.36 / 1.06
	Partial	INS+CIMU	34.31	10.41	1.38	0.19	0.11 / 0.08 / 0.60
	Partial	INS+CIMU+NG	27.74	8.88	1.11	0.23	0.11 / 0.11 / 1.13
	Partial	INS	159.43	803.34	7.35	32.82	0.32 / 0.65 / 1.54
	Partial	INS+NG	19.22	17.42	1.05	1.01	0.24 / 0.46 / 1.44
Notes							
All calculations are compared with (Full GPS Aided INS + CIMU) solution							
None	GPS aid is not used at all						
Full	GPS aid is fully used throughout trajectory						
Partial	Intentional GPS signal loss assumed						
INS	Inertial Navigation System						
CIMU	Calibrated Inertial Measurement Unit (Field calibration is done)						
NG	Non-GPS/GNSS modes active						

Figure 6.19 Trajectory 1, 2D-3D Position Data for Intentional GPS Loss Case
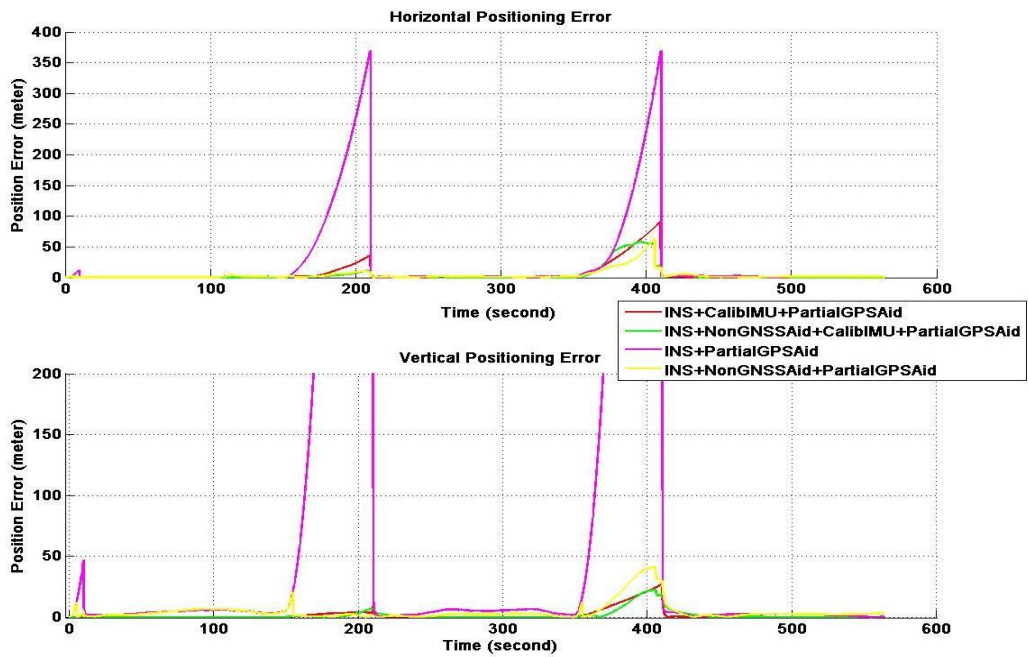
Figure 6.20 Trajectory 1, Horizontal and Vertical Positioning Error Data for Intentional GPS Loss Case

6.2.2.2   Trajectory 2

The 2D/3D positioning, NED velocity and Euler angles calculated from the integrated algorithm with various forms of algorithm modes are given in the Figure 6.21 to Figure 6.25.
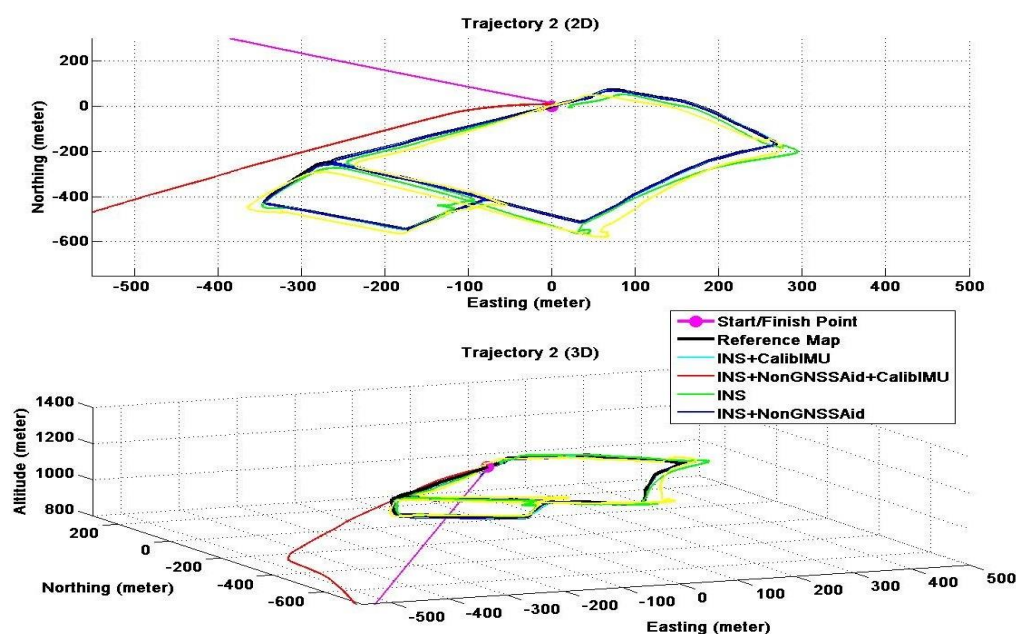
Figure 6.21 Trajectory 2, 2D-3D Position Data

Similar to trajectory 1 case, pure inertial navigation solution with uncompensated inertial sensor data cause highly degraded navigation velocity and positioning solution. On the other hand the non-GNSS aiding modes again highly increase the accuracy of navigation outputs which is tabulated in the Table 6.3 and the performance increase is also seen from the Figure 6.21 and Figure 6.22. Together with the inertial sensor field calibration procedure, the "NG" aiding results in below 30 meter horizontal positioning and below 6 meter vertical positioning accuracy within nearly 10 minutes of typical land vehicle test scenerio in urban environment.
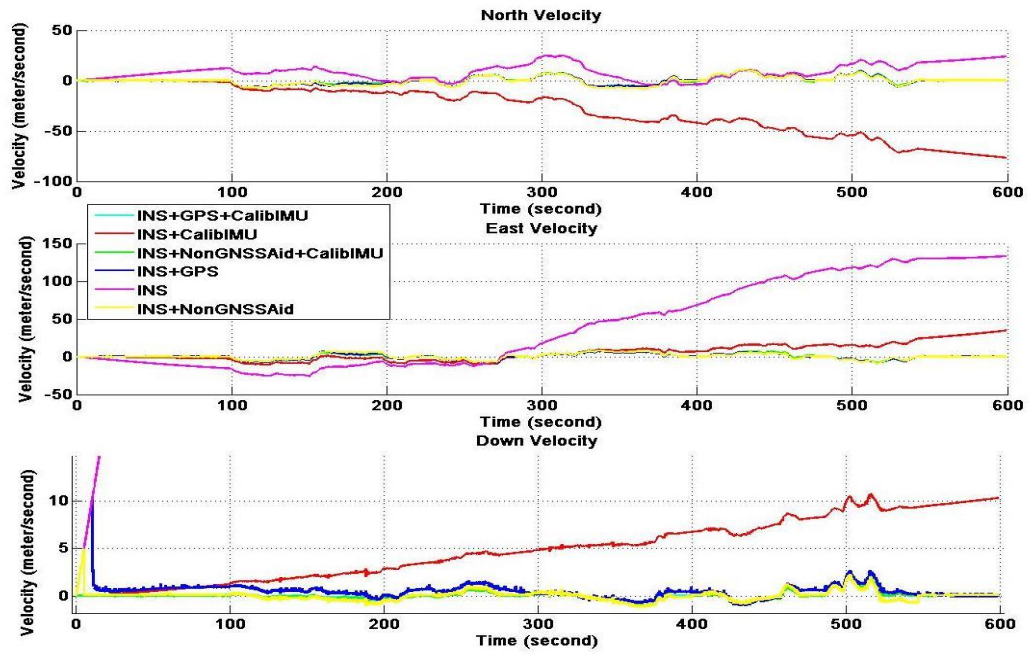
Figure 6.22 Trajectory 2, NED (North-East-Down) Velocity Data
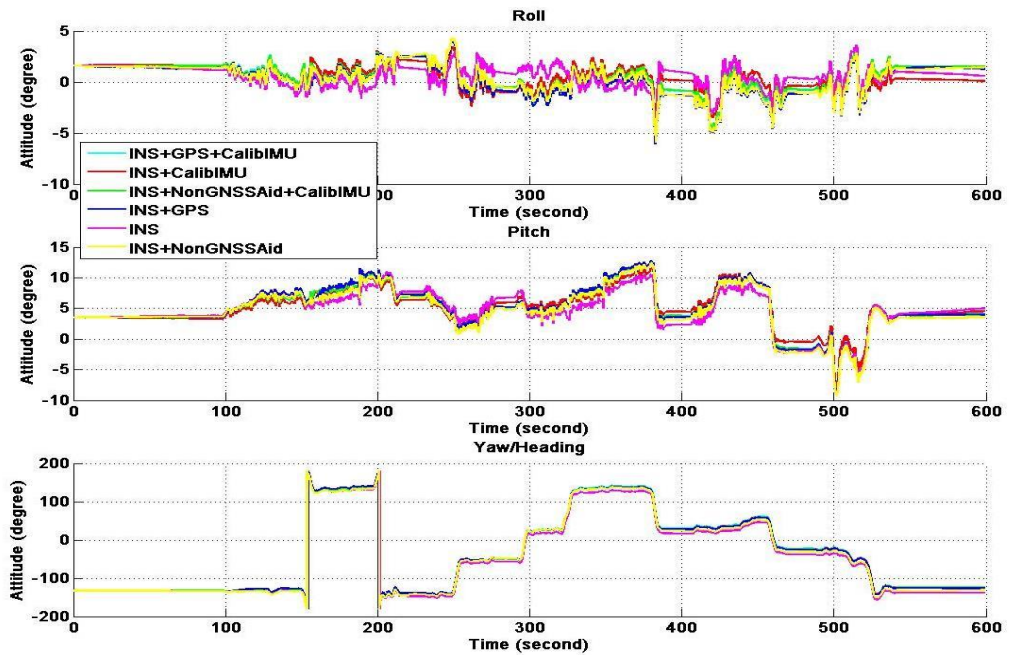
Figure 6.23 Trajectory 2, Euler Angle Data

95

Performance table related to whole test scenerios related to trajectory 2 is given below. Similar to trajectory 1, the Figure 6.24 and Figure 6.25 is representing the positioning solution performance of integrated algorithm with different types of algorithm modes while the GPS receiver aid is inactive. Performance gain in terms of navigation accuracy due to field calibration is again significant which is quite similar to outcomes of trajectory 1. The power of field calibration algorithm is straightforwardly distinguished from Figure 6.25 that is the more than an order of magnitude increase in performance is achived. Similar to the trajectory 1, the non-GNSS aid modes also yield the comparabely higher performance gain with the short term pure inertial solution obtained from the field calibrated inertial sensors.

Table 6.3 Trajectory 2 Navigation Performance Table

| | GPS Aid | Operational Modes | Position Accuracy (meter) | | Velocity Accuracy (meter/second) | | Rotational Accuracy (degree) |
			Horizontal	Vertical	Horizontal	Vertical	Roll / Pitch / Yaw
Trajectory 2	None	INS+CIMU	6811.25	1275.34	40.08	5.73	0.69 / 0.62 / 1.33
	None	INS+CIMU+NG	27.12	16.63	0.86	0.08	0.09 / 0.10 / 1.26
	None	INS	8559.36	84280.23	70.39	379.38	1.08 / 1.11 / 10.01
	None	INS+NG	32.55	21.41	1.03	0.34	0.24 / 0.40 / 5.44
	Full	INS	1.609	4.45	0.38	0.92	0.31 / 0.31 / 2.04
	Partial	INS+CIMU	95.94	41.34	2.65	0.94	0.22 / 0.16 / 0.48
	Partial	INS+CIMU+NG	28.73	5.99	0.99	0.09	0.08 / 0.08 / 0.31
	Partial	INS	450.49	2223.17	11.56	56.91	0.95 / 0.91 / 2.13
	Partial	INS+NG	30.05	19.62	1.73	0.81	0.28 / 0.49 / 2.57

Notes	
All calculations are compared with (Full GPS Aided INS + CIMU) solution	
None	GPS aid is not used at all
Full	GPS aid is fully used throughout trajectory
Partial	Intentional GPS signal loss assumed
INS	Inertial Navigation System
CIMU	Calibrated Inertial Measurement Unit (Field calibration is done)
NG	Non-GPS/GNSS modes active

Figure 6.24 Trajectory 2, 2D-3D Position Data for Intentional GPS Loss Case
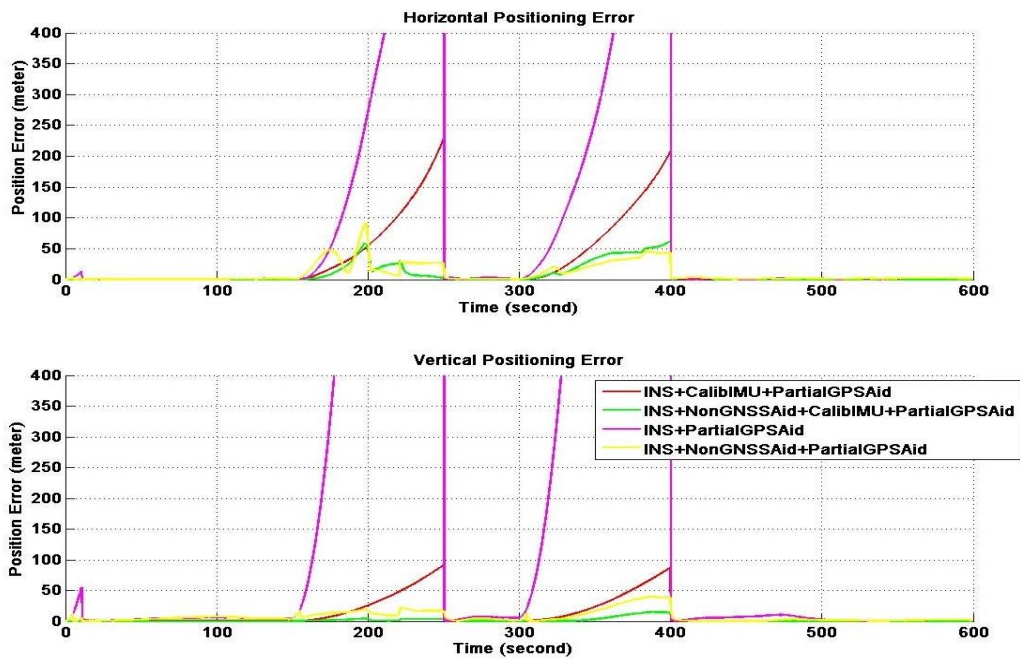
Figure 6.25 Trajectory 2, Horizontal and Vertical Positioning Error Data for Intentional GPS Loss Case

CHAPTER 7

DISCUSSION AND CONCLUSION

In this research,

- The basis of inertial navigation and its integration with other aiding is studied and analyzed.

- EKF based field calibration algorithm is developed, analyzed in simulation environment and tested with real hardware.

- Single-run and multi-run simulation analysis for both tactical and automotive grade IMU show the tremendous increase in the performance.

- Very low cost (sub 100$) GPS aided INS is developed and tested during static and dynamic tests.

- Three different inertial measurement unit is tested with the developed calibration algorithm and the static positioning tests show the performance improvement of the method.

- Land vehicle based dynamic tests for two different trajectories are carried out.

- During the dynamic tests, non-GNSS aid such as non-holonomic constraints and zero velocity update modes are tested.

- Dynamic tests indicate that use of non-GNSS aid is way more superior to the pure inertial mean whether the IMU is calibrated or not.

- If the calibration procedure is carried out together with the non-GNSS aid modes, it is shown that the very low cost IMU and GPS receiver can be used to build integrated navigation system for land applications with accuracy of positioning can be useful (< 50 meters) for couple of minutes of receiver unavailability.

- It is shown that the field calibration process enables the calibration of inertial sensors without the need of accurate, expensive laboratory equipment and the extensive labor of laboratory works.

- Application of the field calibration process toward the highly accurate inertial measurement units (ranging from tactical grade to navigation and further grades) left for future studies. Apart from that, the sensitivity analysis related to relationship between field calibration performance and gravity model error topic needs high amount of attention. In this study, commonly used simple gravity models are taken as error-free models which is exactly opposing the reality. However, the accuracy of those simple models is quite adequate for field calibration of low grades especially uncompansated inertial sensors.

- It is deduced that simple non-accurate and low cost rotary platforms can be used for calibrating numbers of IMU at the same time with the embedded version of the field calibration algorithm. In other words, inertial sensor calibration for mass production facilities can be done without requiring any rigorous calibration processes and manpower especially for low performance uncompansated IMUs.

- The comparison of calibration performance of the field calibration algorithm with the classical laboratory calibration methods for various types of IMUs is left for future work. The study made in this research will be highly beneficial for going forward through that aim.

- The multi-measurement model Kalman filter is tested to be easy to implement method for fusing data from various sources. The modularity of the developed filter structure is highly flexible for employing various types sensor to be data fused together. This feature is an another main objective left for future study to work and blend different data sources for different application fields covering navigation applications for land, sea, and air to yield better performance compared to the stand-alone cases.

REFERENCES

[1]   The Concise Oxford Dictionary, 9th ed., Oxford University Press, Oxford, U.K., 1996.

[2]   Yang Yong, Tightly Coupled MEMS INS/GPS Integration with INS Aided Receiver Tracking Loops, University of Calgary, Calgary, 2008.

[3]   Shin Eun-Hwan, and El-Sheimy Naser, A New Calibration Method for Strapdown Inertial Navigation Systems, The University of Calgary, Calgary, Canada, 2002.

[4]   Syed Z. F., Aggarwal P., Goodall C., Niu X, and El-Sheimy N., A New Multi-Position Calibration Method for MEMS Inertial Navigation Systems, Meas. Sci. Technol. 18 1897-907, 2007.

[5]   Fong W. T., Ong S. K., and Nee A. Y. C, Methods for In-Field User Calibration of an Inertial Measurement Unit Without External Equipment, Meas. Sci. Technol. 19 085202, National University of Singapore, Singapore, 2008.

[6]   Tedaldi Davir, Menegatti Emanuele, Pretto Alberto, IMU Calibration without Mechanical Equipment, University of Padova, Padova, Italy, 2013.

[7]   Tedaldi David, Pretto Alberto, and Menegatti Emanuele, A Robust and Easy to Implement Method for IMU Calibration without External Equipments, 2014 IEEE International Conference on Robotics & Automation (ICRA), Hong Kong Convention and Exhibition Center, Hong Kong, China, 2014.

[8]   Pretto Alberto, and Grisetti Grisetti, Calibration and Performance Evaluation of Low-Cost IMUs, 20th IMEKO TC4 International Symposium and 18th International Workshop on ADC Modelling And Testing, University of Rome, Rome, Italy, 2014.

[9]   Skog L., and Hndel P., Calibration of a Mems Inertial Measurement Unit, Proc. of XVII IMEKO World Congress, 2006.

[10]   Gade Kenneth, Introduction to Inertial Navigation, Tutorial for Geodesi- og Hydrografidagene, Norway, 2005.

[11]   Shin Eun-Hwan, Accuracy Improvement of Low Cost INS/GPS for Land Applications, University of Calgary, Calgary, Canada, 2001.

[12]   Solimeno Adriano, Low-Cost INS/GPS Data Fusion with Extended Kalman Filter for Airborne Applications, Universidade Tecnica de Lisboa, Lisbon, Portugal, 2007.

[13]   http:plasti.cgsociety.org (web-site).

[14]   Anon., Department of Defense World Geodetic System 1984, National Imagery and Mapping Agency (NGA), TR8350.2, 1997.

[15]   Boucher C., The ITRF 2000, International Earth Rotation and Reference Systems Service Technical Note No. 31, 2004.

[16]   Groves Paul D., Principles of GNSS, Inertial, and Multisensor Integrated Navigation Systems, London, U.K, 2008.

[17]   Shuster Malcolm D., A Survey of Attitude Representations, The Journal of the Astronautical Sciences, Vol 41, No. 4, 1993.

[18]   Hughes P. C., Spacecraft Attitude Dynamics, John Wiley & Sons, New York, 1986.

[19]   Mayer A., Rotations and Their Algebra, SIAM Review, Vol. 2, 1960.

[20]   Jiang Y. F., and Lin Y. P., On the Rotation Vector Differential Equation, IEEE Transactions of Aerospace and Electronic Systems, Vol. AES-27, 1991.

[21]   Shuster, Malcolm D., The Kinematic Equation for the Rotation Vector, IEEE Transactions on Aerospace and Electronic Systems, Vol. 29, 1993

[22]   Farrell Jay A., Aided Navigation GPS with High Rate Sensors, 2008.

[23]   Titterton David, Weston John L., Strapdown Inertial Navigation Technology, 2nd Edition, The Institution of Engineering and Technology, London, U.K, 2004

[24]   Savage P. G., Strapdown System Algorithms, Advances in Strapdown Inertial Systems, AGARD Lecture Series No. 133, 1984

[25]   Grosekatthöfer Harsten, Yoon Zizung, Introduction into Quaternions for Spacecraft Attitude Representation, Technical University of Berlin, Berlin, Germany, 2012

[26]   Axelrad P., Lawrence D., Attitude Representation, ASEN3200, 2006.

[27]   Pitman George R., Inertial Guidance, University of California Engineering and Physical Sciences Extension Series, 1962.

[28]   Angrisano Antonio, GNSS/INS Integration Methods, University of Calgary, Calgary, U.S., 2010.

[29]   Global Positioning Systems Directorate Systems Engineering & Integration, Interface Specification IS-GPS-200, 2013.

[30]   Global Navigation Satellite System GLONASS, Interface Control Document, Moscow, 1998.

[31]   Cheng Chao-heh, Calculations for Positioning with the Global Navigation Satellite System, Ohio University, Ohio, U.S, 1998.

[32]   Kaplan Elliott D., Hegarty Christopher J., Understanding GPS Principles and Applications, Second Edition, 2006.

[33]   Welch Greg, Bishop Gary, An Introduction to the Kalman Filter, SIGGRAPH 2001 Course Note, University of North Carolina, Chapel Hill, U.S, 2001.

[34]   Gelb Arthur, Kasper Joseph F., Nash Raymond A., Price Charles F., and, Sutherland Arthur A., Applied Optimal Estimation, 2001.

[35]   Simon Dan, Optimal State Estimation, Kalman H Infinity, and Nonlinear Approaches, 2006.

[36]   Grewal Mohinder S., Andrews Asgus P., Kalman Filtering Theory and Practice Using MATLAB, 2001.

[37]   Haykin Simon, Kalman Filtering and Neural Networks, 2001.

[38]   Kalman R. E., A New Approach to Linear Filtering and Prediction Problems, ASME, 1960.

[39]   Faragher Ramsey, Understanding the Basis of the Kalman Filter Via a Simple and Intuitive Derivation, IEEE Signal Processing Magazine, 2012.

[40] Kleeman Lindsay, Understanding and Applying Kalman Filtering, Monash University, Clayton.

[41] Brown Robert Grover, Hwang Patrick Y. C., Introduction to Random Signals and Applied Kalman Filtering, Third Edition, 1985.

[42] Ramanandan Arvind, Chen Anning, Farrel Jay A., and Suvarna Sarath, Detection of Stationarity in an Inertial Navigation System, 23rd International Technical Meeting of the Satellite Division of The Institute of Navigation, Portland, 2010.

[43] Benzerrouk Hamza, Nebylov Alexander, Salhi Hassen, and Closas Pau, MEMS IMU/ZUP Based Cubature Kalman Filter applied to Pedestrian Navigation System, International Electronic Conference on Sensors and Applications, 2014.

[44] Xu Zhegyi, Wei Jianming, Zhang Bo, and Yang Weijun, A Robust Method to Detect Zero Velocity for Improved 3D Personal Navigation Using Inertial Sensors, 2015.

[45] Hsu D. Y., Comparison of four gravity models, Position Location and Navigation Symposium IEEE, 1996.

[46] Chatfield A. B., Benneth M. M., and Chen T., Effect of Gravity Model Inaccuracy on Navigation Performance, AIAA Journal, Vol. 13, No. 11, 1975.

[47] Kwon Jay Hyoun, Gravity Compensation Methods for Precision INS, The Ohio State University, 2004.

[48] Kong Xiaoying, Inertial Navigation System Algorithms for Low Cost IMU, The University of Sydney, 2000.

[49] Savage Paul G., Coarse Leveling ıf INS Attitude Under Dynamic Trajectory Conditions, 2015.

[50] Gelb A., Applied Optimal Estimation, The M.I.T Press, Cambridge, Massachusetts, 1974.

[51] Priestley, M. B., Spectral Analysis and Time Series, Volume 1, Academic Press, 1981.

[52] Jekeli C., Inertial Navigation Systems with Geodetic Applications, New York, U.S, 2000.

[53] Grewal M., Weill L., and Andrews A., Global Positioning Systems, Inertial Navigation, and Integration, John Wiley & Sons, Inc, 2007.

[54] Rogers Robert M., Applied Mathematics in Integrated Navigation Systems, Second Edition, AIAA, 2003.

[55] El-Diasty M, El-Rabbany A., and Pagiatakis S., An Accurate Nonlinear Stochastic Model for MEMS-Based Inertial Sensor Error with Wavelet Networks, Journal of Applied Geodesy Volume 1, 2007.

[56] Nassar S., Accurate INS/DGPS Positioning Using INS Data De-Noising and Autoregressive (AR) Modeling of Inertial Sensor Errors, Geomatica, 2005.

[57] Flenniken W., Wall J., and Bevly D. M., Characterization of Various IMU Error Sources and the Effect on Navigation Performance, Proceedings of ION GNSS, Long Beach, CA, 2005.

[58] Wall J., and Bevly D. M., Characterization of Inertial Sensor Measurements for Navigation Performance Analysis, Proceedings of the ION GNSS, 2006.

[59] El-Diasty Mohammaed, and Pagiatakis Spiros, Calibration and Stochastic Modelling of Inertial Navigation Sensor Errors, York University, Canada, 2008.

[60] MPU-6000 and MPU-6050 Product Specification Revision 3.4, InvenSense Inc., www.invensense.com, 2013.

[61] VN-200 GPS/INS High Performance Embedded Navigation, VectorNav, www.vectornav.com

[62] Mti 10-series and Mti 100-series User Manual, XSENS, www.xsens.com

APPENDIX A

GRAVITY MODEL

As explained in reference [16] Somigliana gravity model described below is used in this study. Any other gravity model such as J2-J4 gravity model can be used as well.

$$\underline{g_0^N}(L_{b/e}) = \begin{bmatrix} 0 \\ 0 \\ 1 \end{bmatrix} * (9.7803253359 \frac{(1+0.001931853\sin^2(L_{b/e}))}{\sqrt{1-e^2\sin^2(L_{b/e})}}) \qquad \text{A-7-1}$$

$$\underline{\gamma_0^N}(L_{b/e}) = \underline{g_0^N}(L_{b/e}) + (ssm(\underline{\omega_{IE}^N}))^2 C_E^N \underline{r_{ES}^E} \qquad \text{A-7-2}$$

$$\underline{r_{ES}^E} = \begin{bmatrix} R_E\cos(L_{b/e})\cos(\lambda_{b/e}) \\ R_E\cos(L_{b/e})\sin(\lambda_{b/e}) \\ (1-e^2)R_E\sin(L_{b/e}) \end{bmatrix}, \quad \left|\underline{r_{ES}^E}\right| = R_E\sqrt{\cos^2(L_{b/e})+(1-e^2)^2\sin^2(L_{b/e})} \qquad \text{A-7-3}$$

$$\underline{\gamma_{IB}^N}(L_{b/e}) = \frac{(\left|\underline{r_{ES}^E}\right|)^2}{(\left|\underline{r_{ES}^E}\right|+h_{b/e})^2}\underline{\gamma_0^N}(L_{b/e}) \qquad \text{A-7-4}$$

$$\underline{g^N}(L_{b/e},h_{b/e}) = \underline{\gamma_{IB}^N}(L_{b/e}) - (ssm(\underline{\omega_{IE}^N}))^2 C_E^N \underline{r_{EB}^E} \qquad \text{A-7-5}$$

$$\underline{r_{EB}^E} = \begin{bmatrix} R_E\cos(L_{b/e})\cos(\lambda_{b/e}) \\ R_E\cos(L_{b/e})\sin(\lambda_{b/e}) \\ ((1-e^2)R_E+h_{b/e})\sin(L_{b/e}) \end{bmatrix} \qquad \text{A-7-6}$$

APPENDIX B

STOCHASTIC PROCESSES

Various types of stochastic processes are well documented in Gelb [50], Priestley [51], and their application in inertial navigation is studied and reported in Jekeli [52], Grewal et al. [53], Rogers [54]. Also El-Diasty et al [55], Nassar [56], Flenniken et al [57], and Wall and Bevly [58] are key papers that describe the practical implementation for these stochastic processes. According to [calibration and stoch proc,56], the following terms should be defined

- Continous time signals are signals that are described by an analytical function of time
- Discrete time signals are signals that have values only at discrete instants of time. Sampling a contionus-time signal generates a discrete signal
- Stationary stochastic process is a process whose joint probability distribution does not change when shifted in time or space.
- Autocorrelation function of a discrete signal is the expected value of the product of a random signal with a time-shifted version of itself.

In this part, only three stochastic models are stated which are names as;

- Random constant
- Random walk
- Gauss-Markov

B.1 Random Constant (RC) Model

A random constant or bias can be described as an unpredictable random quantitiy with a constant value through the following differential equation is continuous time domain [52]

$$\dot{x} = 0 \tag{B-1}$$

In discrete time, the process is represented by the following equation:

$$x_k = x_{k-1} \tag{B-2}$$

B.2 Random Walk (RW) Model

A random walk (RW) process is a zero-mean Gaussian stochastic process with stationary independent increments i.e, in a RW process the difference $(x_k - x_{k-1})$ is a purely random sequence w_k. A RW can be described through the following differential equation in continuous time domain [52]

$$\dot{x} = w \tag{B-3}$$

In discrete time, process can be described through the following equation [53]

$$x_k = x_{k-1} + w_k \tag{B-4}$$

B.3 Gauss-Markov Model

Gauss-Markov (GM) random processes are stationary processes that have exponential autocorrelation functions. The GM process is important because it is able to represent a large number of physical processes with reasonable accuracy and has a relatively simple mathematical formulation [50]. For a random process x with zero mean, mean squared error σ^2, and correlation time T_c, the first-order GM model is described by the following continuos-time equation [50]

$$\dot{x} = -\frac{1}{T_c} x + w \tag{B-5}$$

The first-order GM process is discrete time can be written as [53]

$$x_k = e^{\frac{-\Delta t}{Tc}} x_{k-1} + w_k \tag{B-6}$$

APPENDIX C

TRAJECTORY GENERATION

In this study, the main purpose of trajectory generation process is generating inertial measurement unit stimulus data which are perfect accelerometer triad and perfect gyroscope triad measurement from defined both linear and rotational trajectory. In order to accomplish that aim, the reverse procedure of inetial navigation mechanization is used. In order to visualize and define trajectory in navigation reference frame, it's necessary to supply time series of body linear acceleration $a_{b/e}^b$ and body angular rotation around navigation reference frame $\omega_{b/n}^b$ data resolved in body axis together with initial geographic location, body linear velocity and orientation.

From equation (2.23) , it is straightforward to deduce gyroscope readings from given body rotation $\omega_{b/n}^b$.

$$\underline{\omega}_{b/n}^{(b)} = \underline{\omega}_{b/i}^{(b)} - \underline{\omega}_{n/e}^{(b)} - \underline{\omega}_{e/i}^{(b)}$$

C-1

$$\underline{\omega}_{b/i}^{(b)} = \underline{\omega}_{b/n}^{(b)} + C_b^{n^T} \underline{\omega}_{n/e}^{(n)} + C_b^{n^T} \underline{\omega}_{e/i}^{(n)}$$

$\underline{\omega}_{e/i}^{(n)}$ and $\underline{\omega}_{n/e}^{(n)}$ are given in expressions (2.10) and (2.21) respectively.

For accelerometer readings, the expression (2.48) is manipulated as follows

$$\underline{a}_{b/e}^{(n)} = \underline{f}_{b/i}^{(n)} + \underline{g}_b^{(n)} - \{ssm(\underline{\omega}_{n/e}^{(n)}) + 2ssm(\underline{\omega}_{e/i}^{(n)})\}\underline{v}_{b/e}^{(n)}$$

C-2

$$\underline{f}_{b/i}^{(b)} = C_b^{n^T}(\underline{a}_{b/e}^{(n)} - \underline{g}_b^{(n)} + \{ssm(\underline{\omega}_{n/e}^{(n)}) + 2ssm(\underline{\omega}_{e/i}^{(n)})\}\underline{v}_{b/e}^{(n)})$$

The similar approach given in the expression (2.41) is used between body and navigation frames to obtain $a_{b/e}^n$.

$$v_{b/e}^{(n)} = C_b^n v_{b/e}^{(b)} \tag{C-3}$$

The time derivative of the above expression:

$$a_{b/e}^{(n)} = \dot{C}_b^n v_{b/e}^{(b)} + C_b^n a_{b/e}^{(b)} \tag{C-4}$$

Where

$$\dot{C}_b^n = ssm(\omega_{b/n}^{(n)})C_b^n \tag{C-5}$$

Substitude (C-5) into the expression (C-4) results in the following expression

$$a_{b/e}^{(n)} = ssm(\omega_{b/n}^{(n)})\underbrace{C_b^n v_{b/e}^{(b)}}_{v_{b/e}^{(n)}} + C_b^n a_{b/e}^{(b)} \tag{C-6}$$

$$a_{b/e}^{(n)} = ssm(\omega_{b/n}^{(n)})v_{b/e}^{(n)} + C_b^n a_{b/e}^{(b)}$$

The inverse inertial navigation mechanization based trajectory generation can be recursively processed as given below.

1. Update $\omega_{n/e}^n$ and $\omega_{e/i}^n$ by using prior $L_{b/e}, \lambda_{b/e}, h_{b/e}$ and $\underline{v_{b/e}^n}$.

2. Update C_b^n via integrating expression (C-5) by using updated $\omega_{n/e}^n, \omega_{e/i}^n$ and given $\omega_{b/n}^b$.

3. Calculate $\omega_{b/i}^b$ via expression (C-1) by using updated $C_b^n, \omega_{n/e}^n, \omega_{e/i}^n$ and given $\omega_{b/n}^b$.

4. Calculate $a_{b/e}^n$ via expression (C-6) by using prior $\underline{v_{b/e}^n}$, updated C_b^n, given $\omega_{b/n}^b$ and $a_{b/e}^b$.

5. Update $v_{b/e}^n$ via integrating the updated $a_{b/e}^n$.

6. Update $L_{b/e}, \lambda_{b/e}, h_{b/e}$ via integrating the updated $v_{b/e}^n$.

7. Calculate $f_{b/i}^b$ via expression (C-2) by using updated $C_b^n, L_{b/e}, \lambda_{b/e}, h_{b/e}, v_{b/e}^n, \omega_{n/e}^n, \omega_{e/i}^n$ and $a_{b/e}^n$.

MC FIGURES

D.1 Automotive Grade
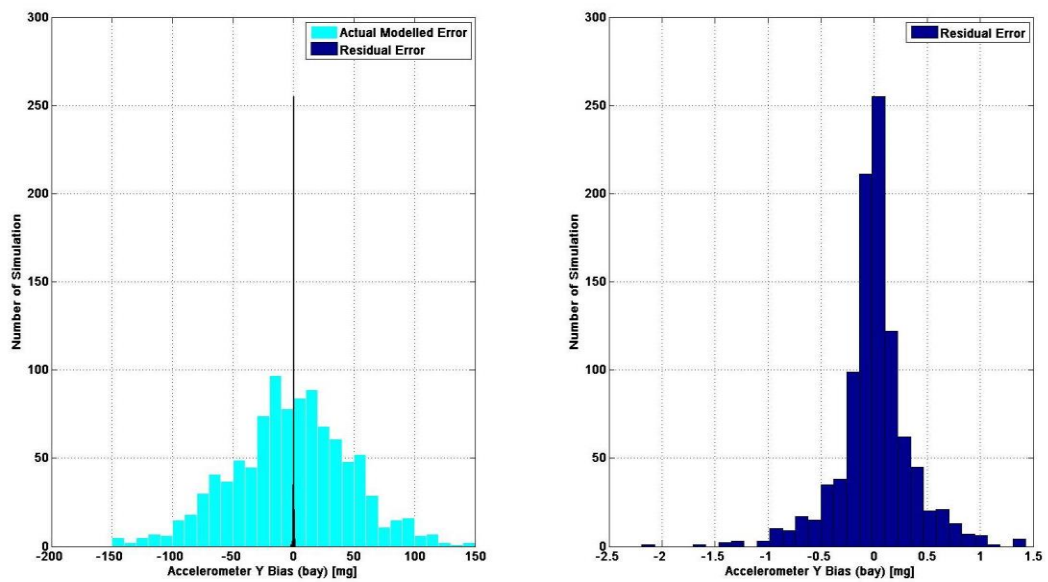
Figure D.7.1 Automotive Grade Y Accelerometer Modelled and Residual Bias Error
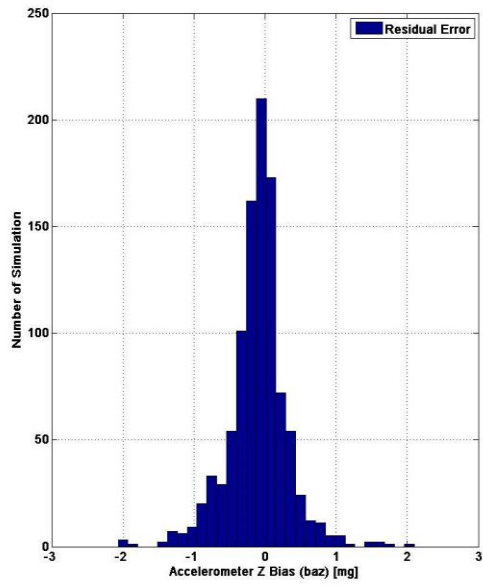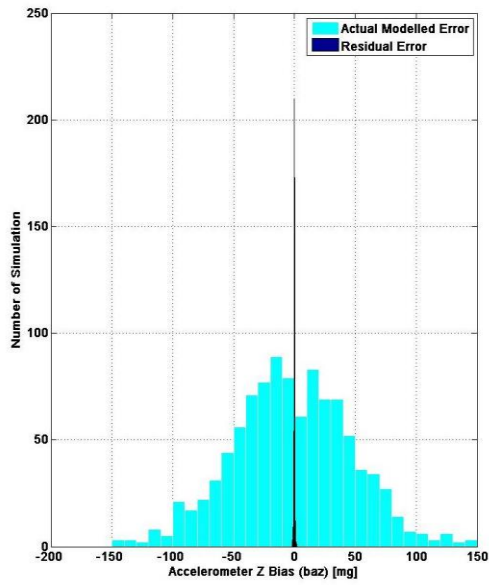
Figure D.7.2 Automotive Grade Z Accelerometer Modelled and Residual Bias Error
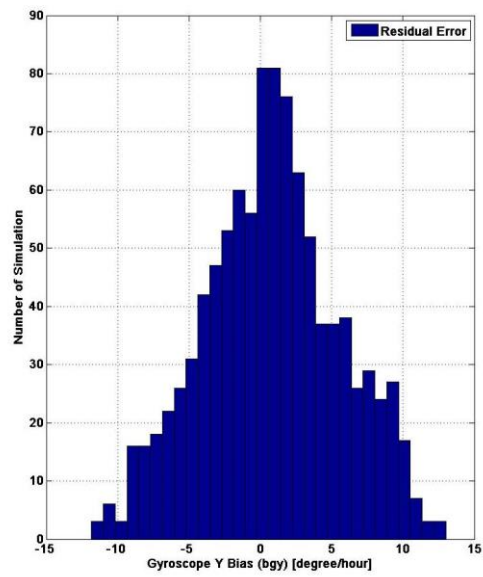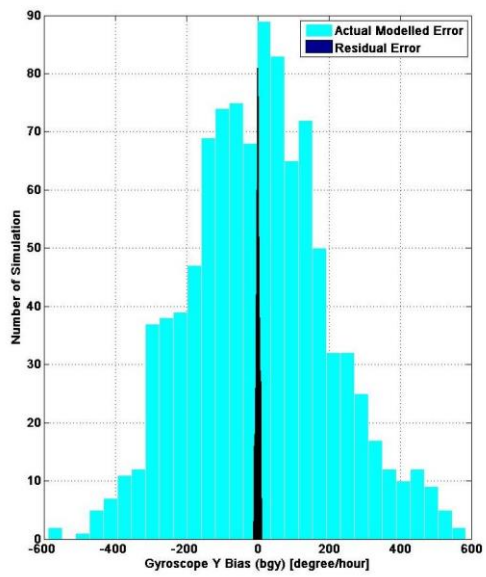
Figure D.7.3 Automotive Grade Y Gyroscope Modelled and Residual Bias Error
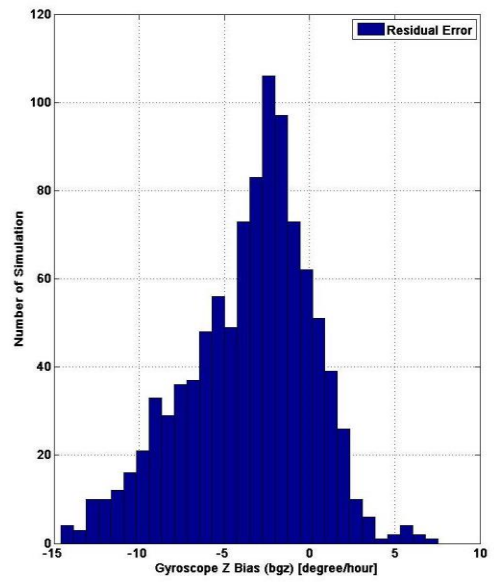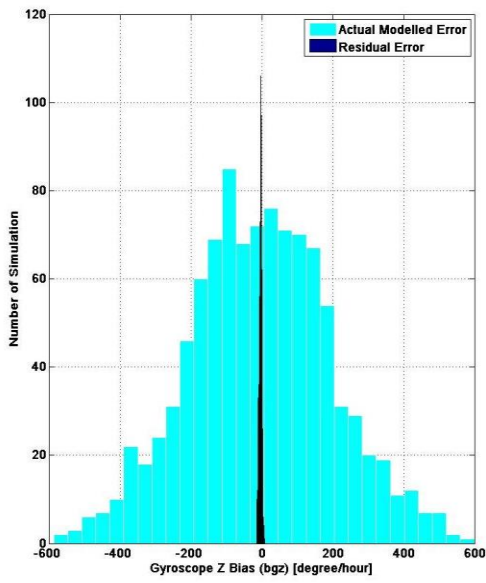
Figure D.7.4 Automotive Grade Z Gyroscope Modelled and Residual Bias Error
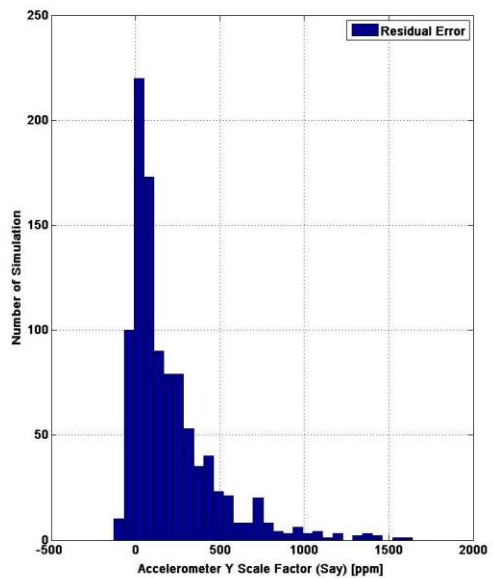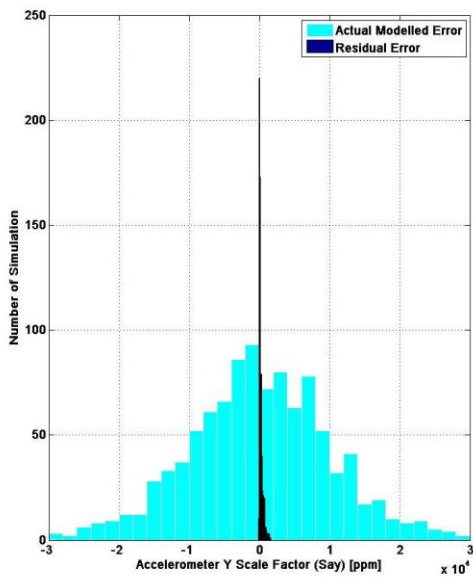
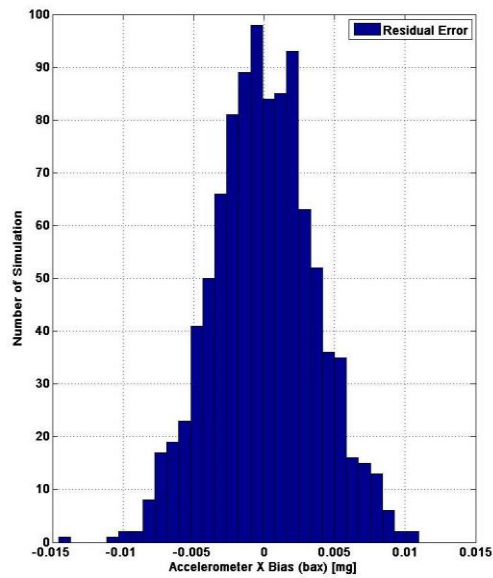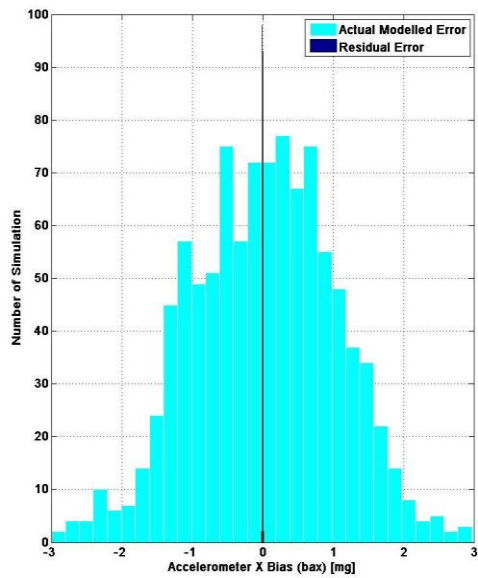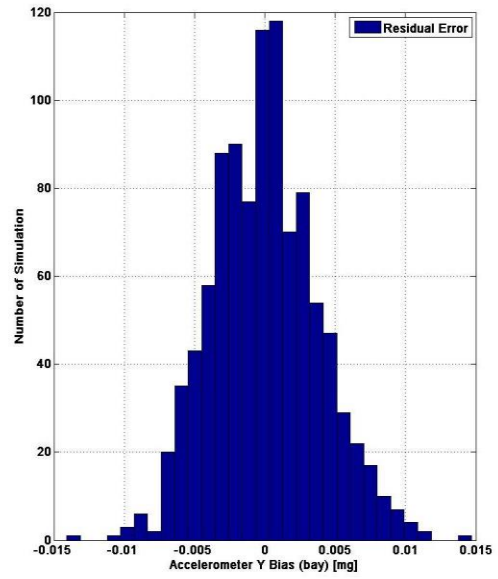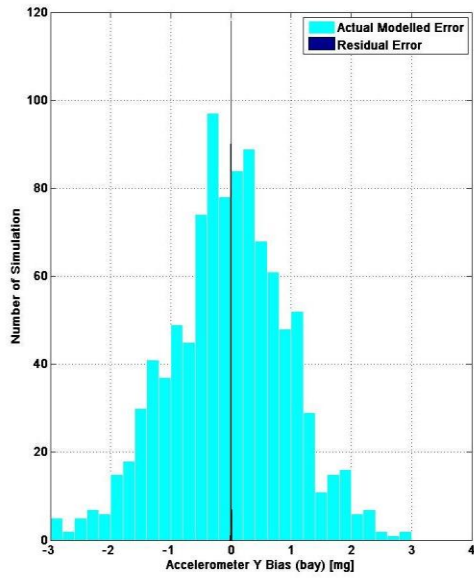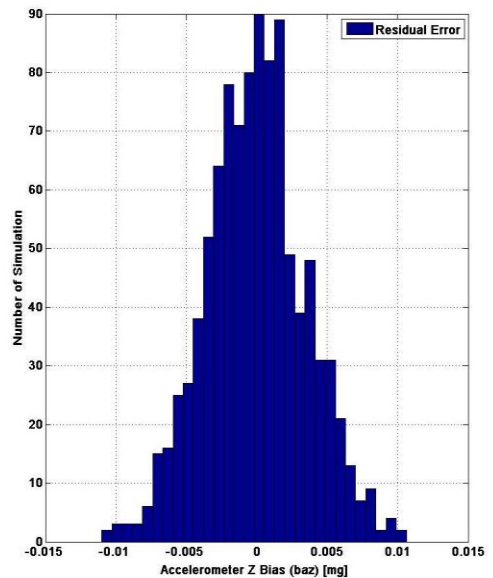**Figure D.7.5 Automotive Grade Y Accelerometer Modelled and Residual Scale Factor**
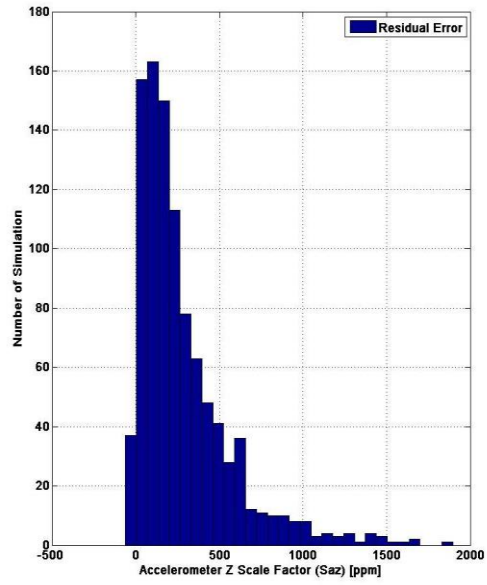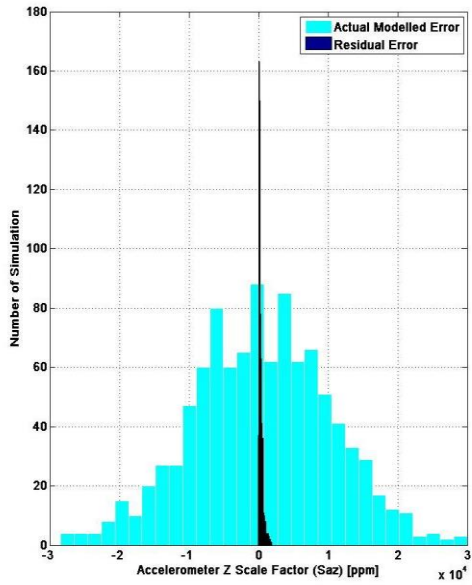
Figure D.7.6 Automotive Grade Z Accelerometer Modelled and Residual Scale Factor
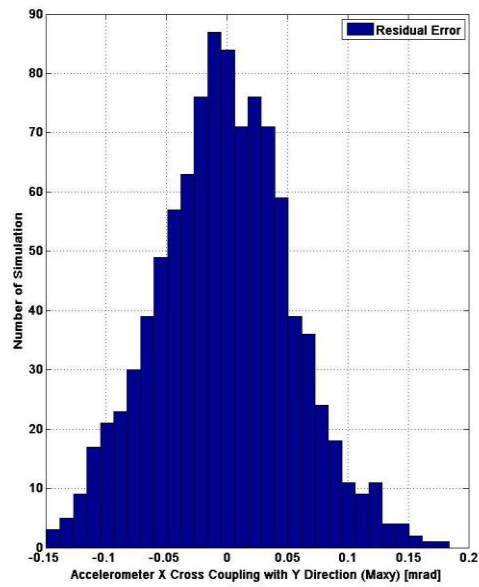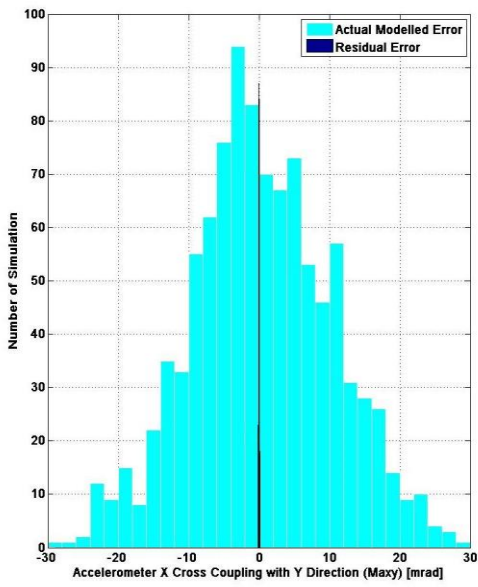
Figure D.7.7 Automotive Grade Accelerometer M$_{axy}$ Modelled and Residual Cross Coupling Error
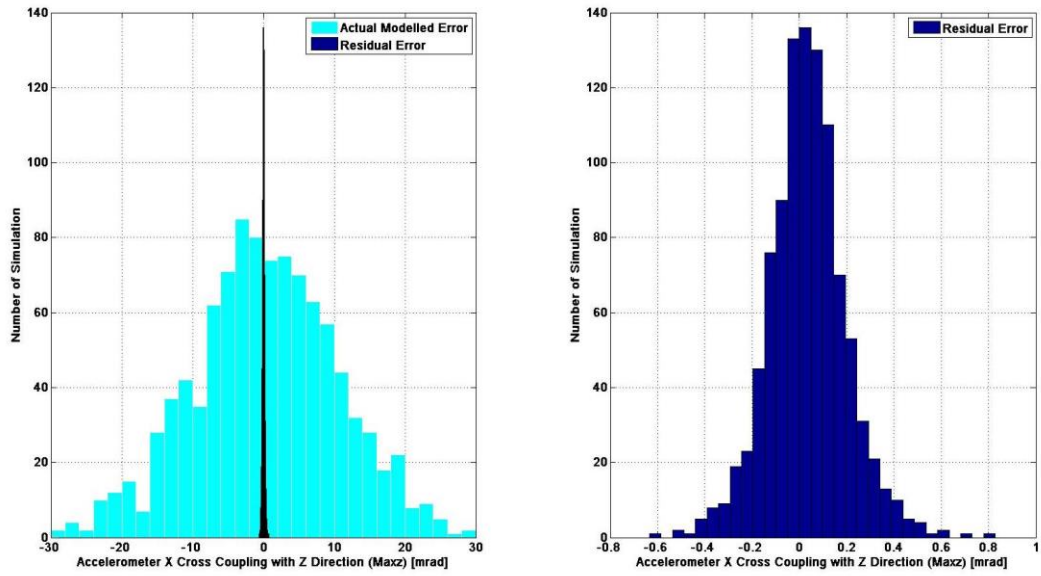
Figure D.7.8 Automotive Grade Accelerometer M$_{axz}$ Modelled and Residual Cross Coupling Error
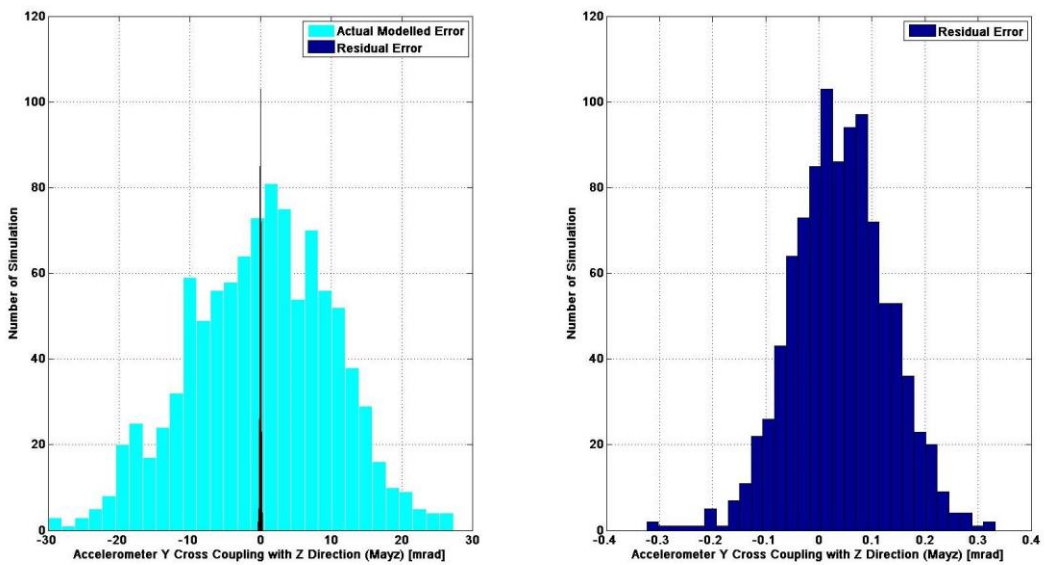
Figure D.7.9 Automotive Grade Accelerometer M$_{ayz}$ Modelled and Residual Cross Coupling Error
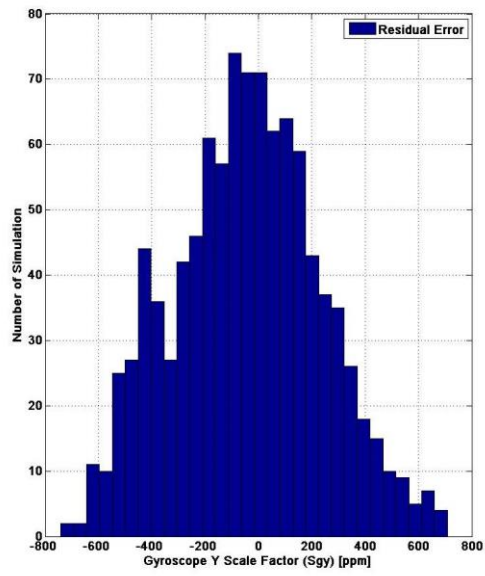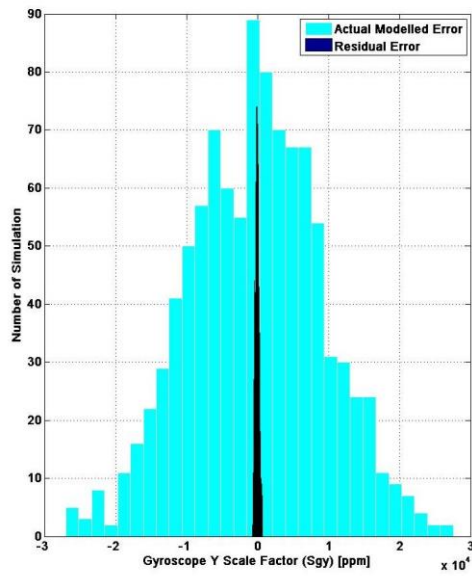
Figure D.7.10 Automotive Grade Y Gyroscope Modelled and Residual Scale Factor
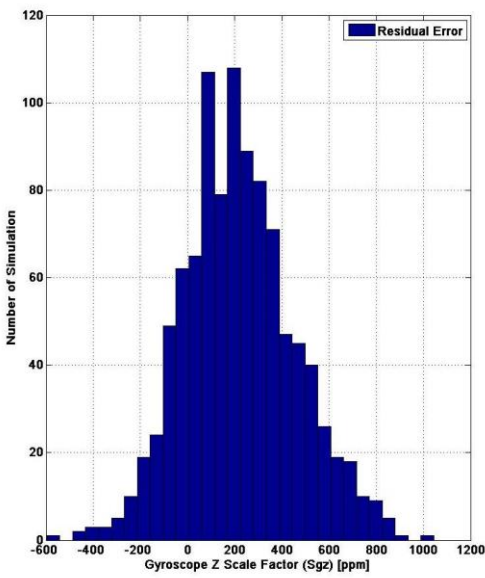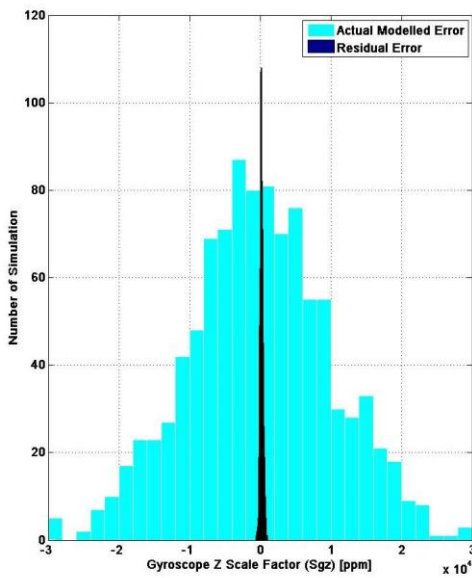
Figure D.7.11 Automotive Grade Z Gyroscope Modelled and Residual Scale Factor

118
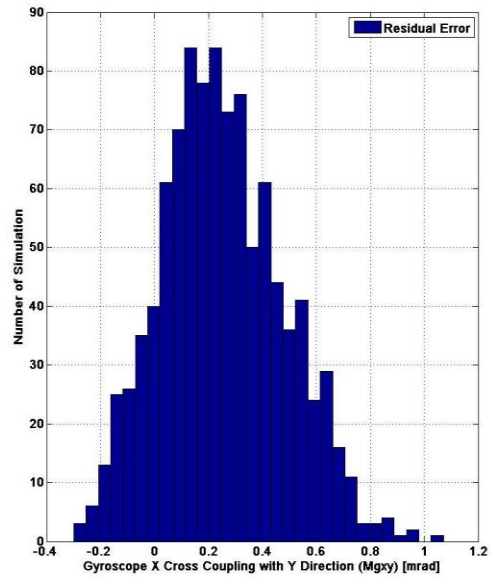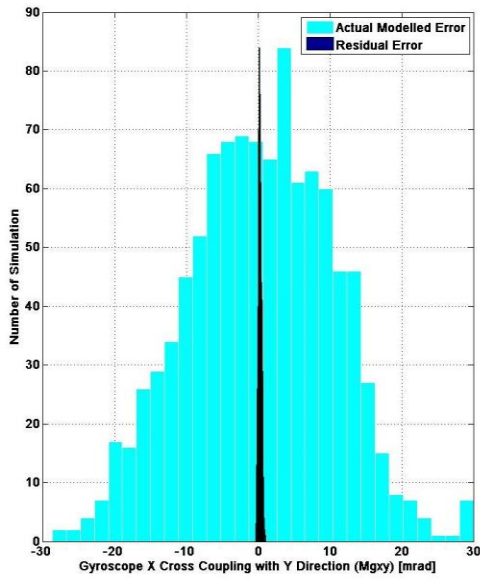
Figure D.7.12 Automotive Grade Gyroscope M$_{gxy}$ Modelled and Residual Cross Coupling Error
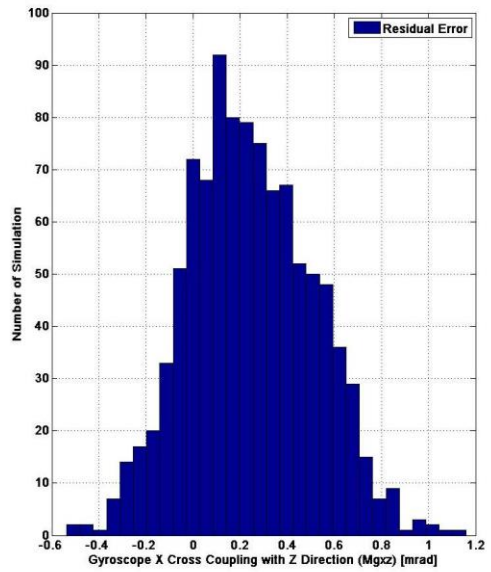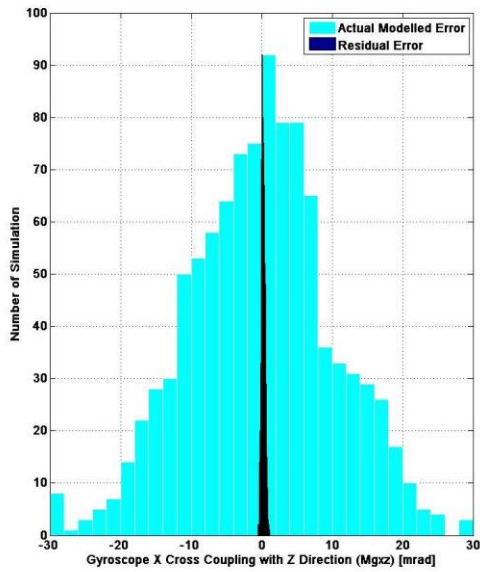
Figure D.7.13 Automotive Grade Gyroscope M$_{gxz}$ Modelled and Residual Cross Coupling Error
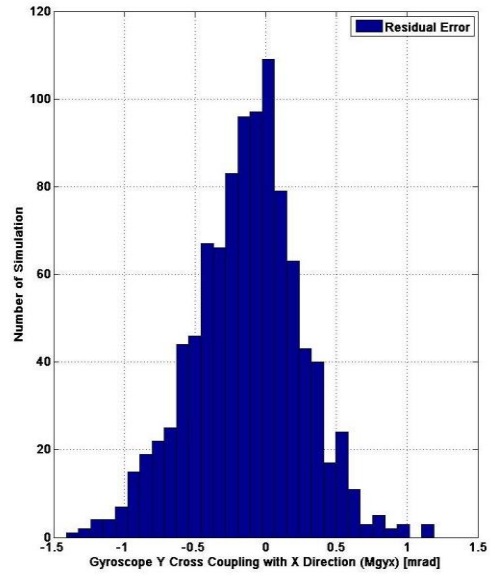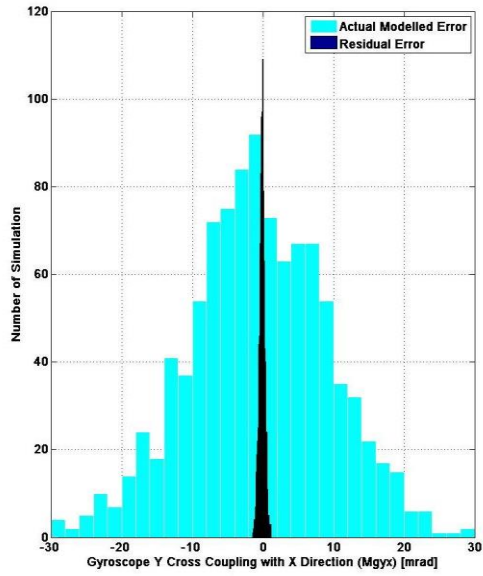
Figure D.7.14 Automotive Grade Gyroscope M$_{gyx}$ Modelled and Residual Cross Coupling Error
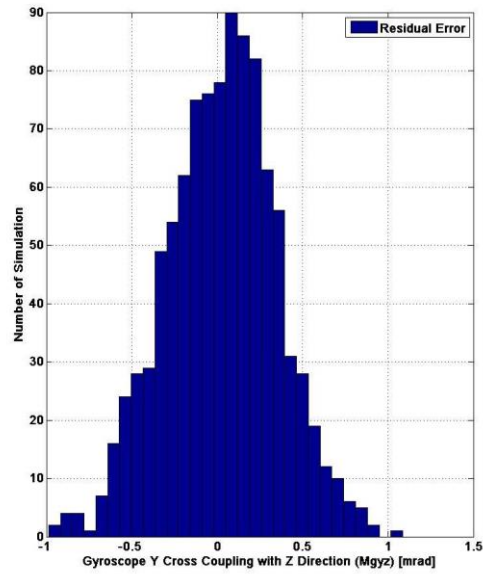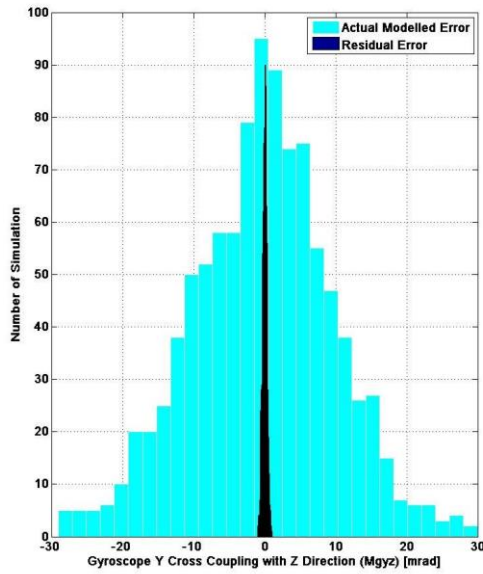
Figure D.7.15 Automotive Grade Gyroscope M$_{gyz}$ Modelled and Residual Cross Coupling Error
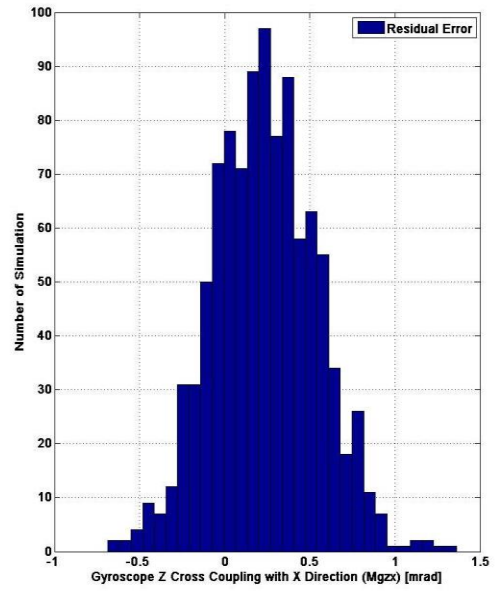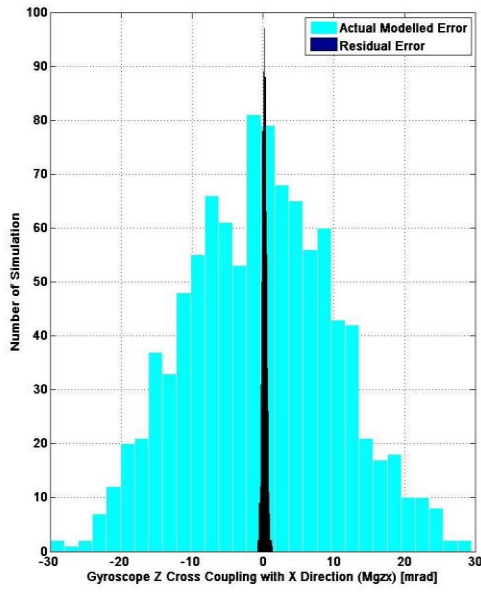
Figure D.7.16 Automotive Grade Gyroscope M$_{gzx}$ Modelled and Residual Cross Coupling Error
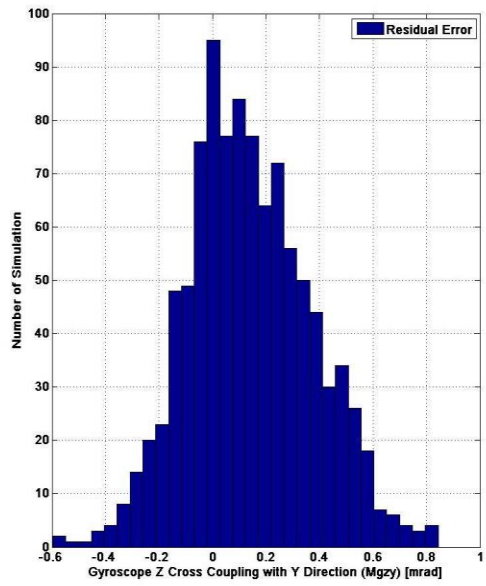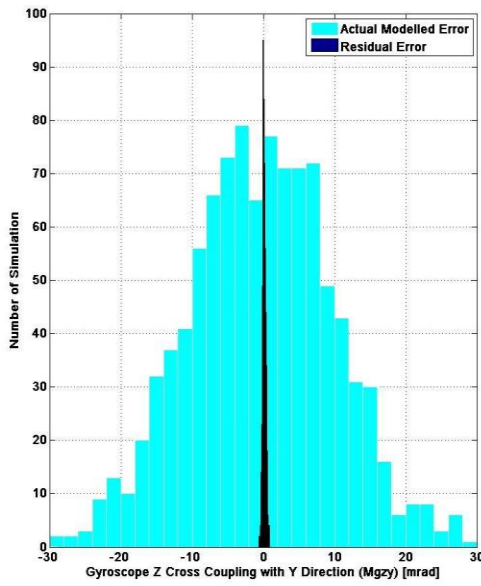
Figure D.7.17 Automotive Grade Gyroscope M$_{gzy}$ Modelled and Residual Cross Coupling Error

121
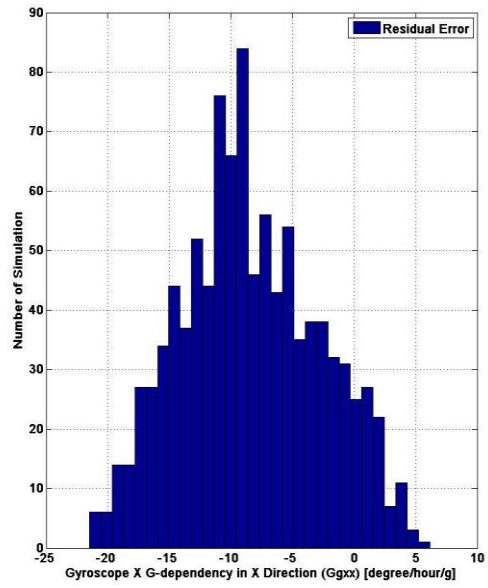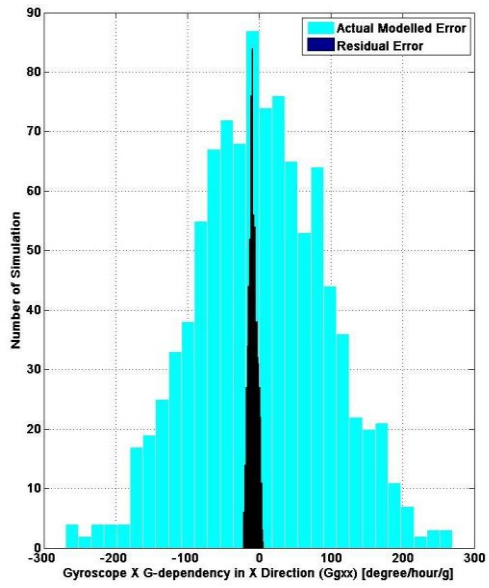
Figure D.7.18 Automotive Grade Gyroscope G$_{gxx}$ Modelled and Residual G-Dependent Bias Error
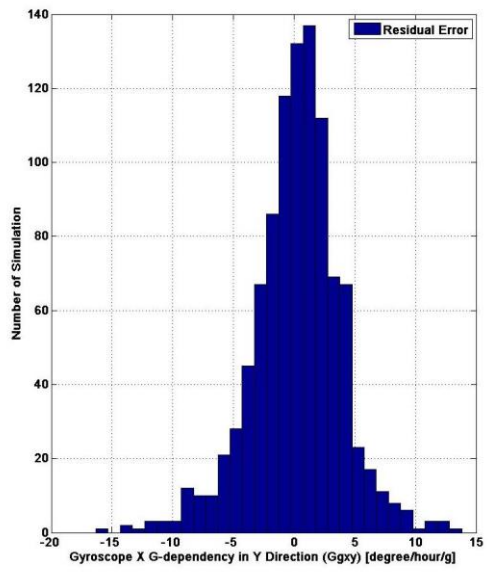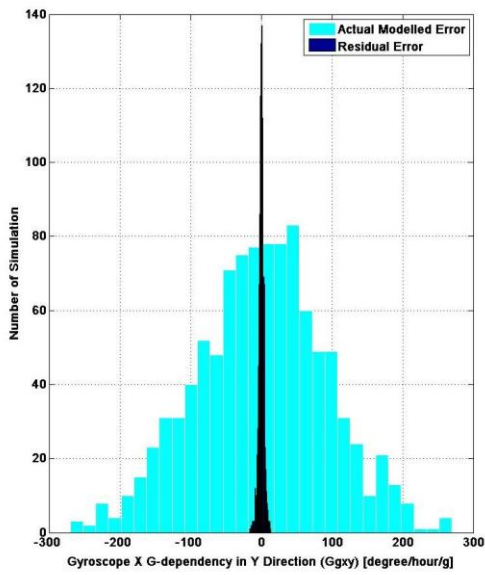
Figure D.7.19 Automotive Grade Gyroscope G$_{gxy}$ Modelled and Residual G-Dependent Bias Error
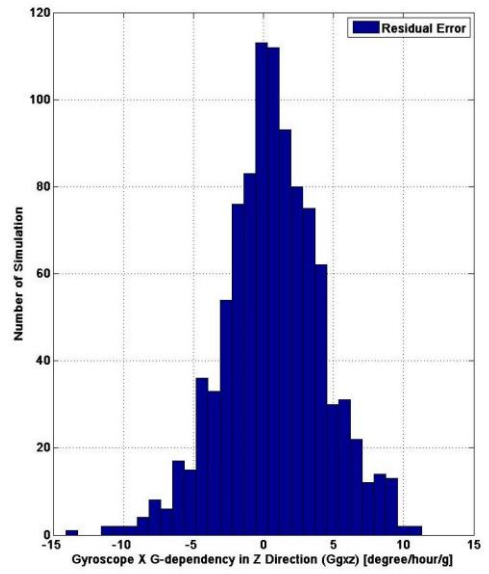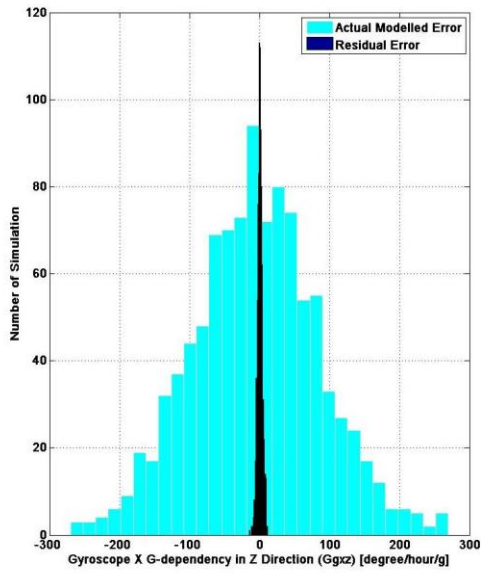
Figure D.7.20 Automotive Grade Gyroscope G_{gxz} Modelled and Residual G-Dependent Bias Error

Figure D.7.21 Automotive Grade Gyroscope G_{gyx} Modelled and Residual G-Dependent Bias Error

123
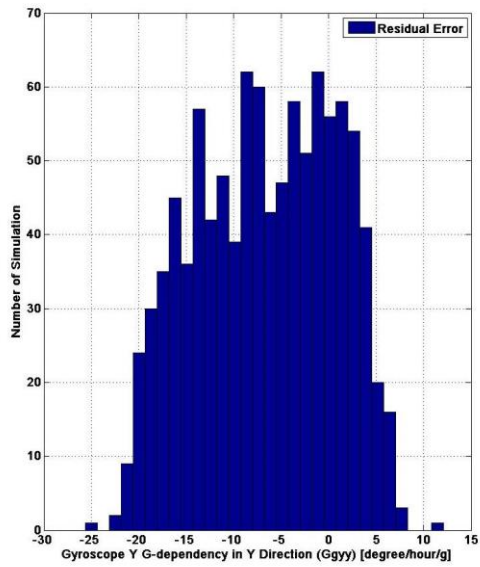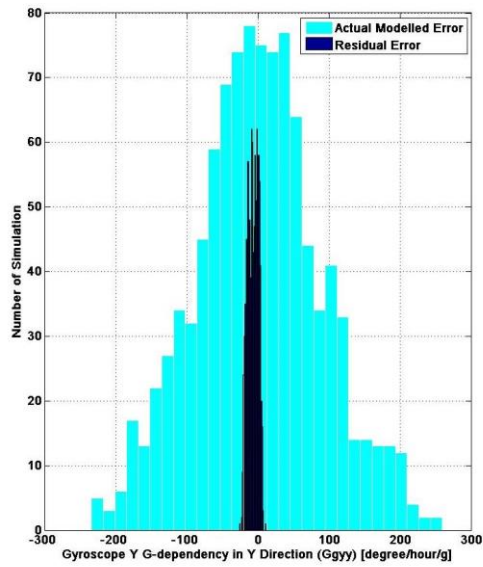
Figure D.7.22 Automotive Grade Gyroscope G$_{gyy}$ Modelled and Residual G-Dependent Bias Error
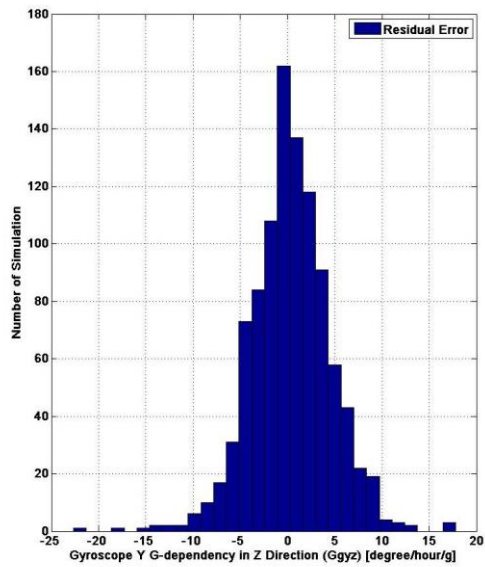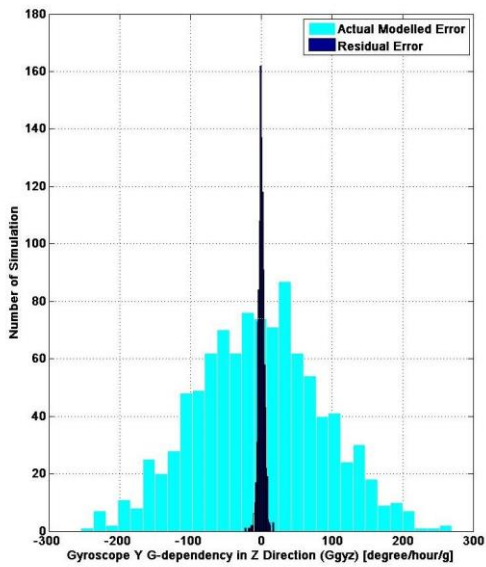
Figure D.7.23 Automotive Grade Gyroscope G$_{gyz}$ Modelled and Residual G-Dependent Bias Error
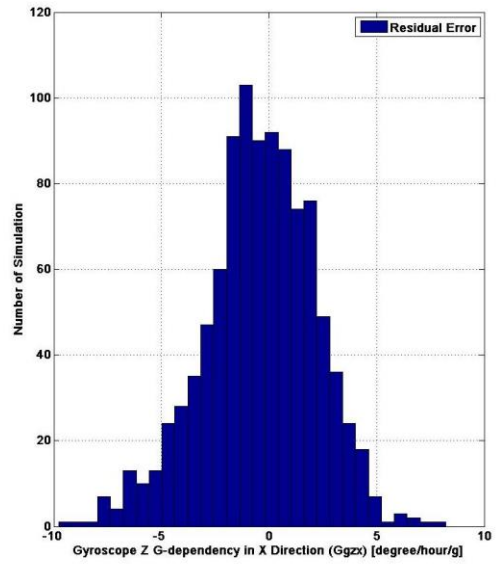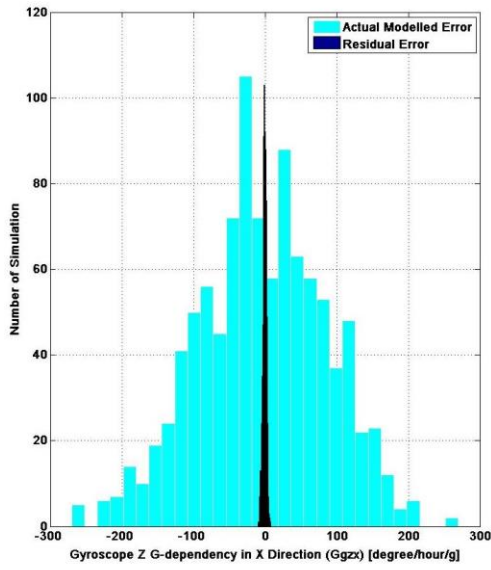
Figure D.7.24 Automotive Grade Gyroscope G$_{gzx}$ Modelled and Residual G-Dependent Bias Error
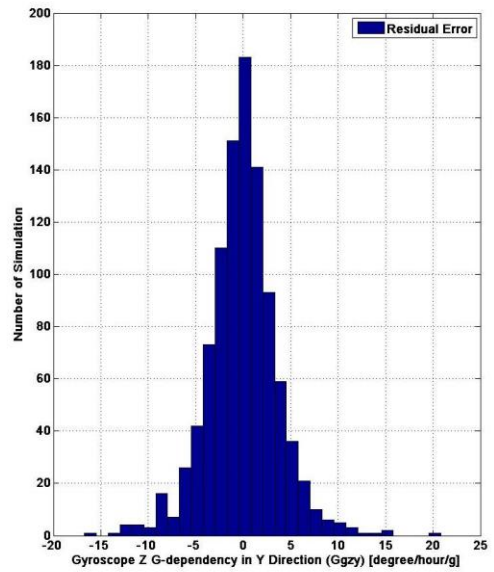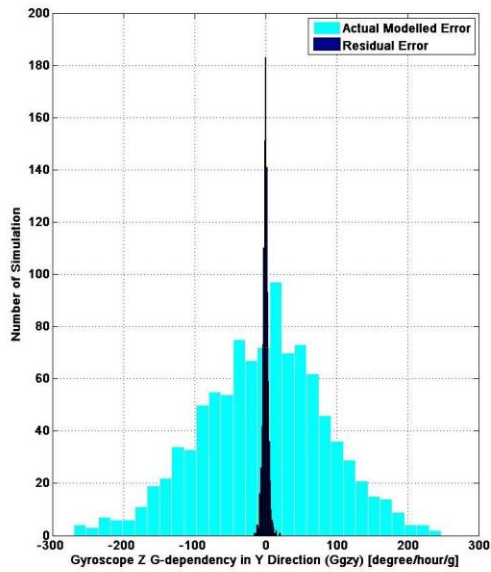
Figure D.7.25 Automotive Grade Gyroscope G$_{gzy}$ Modelled and Residual G-Dependent Bias Error

125
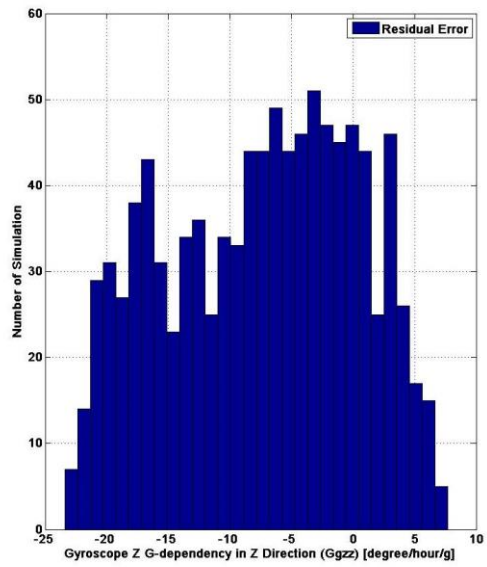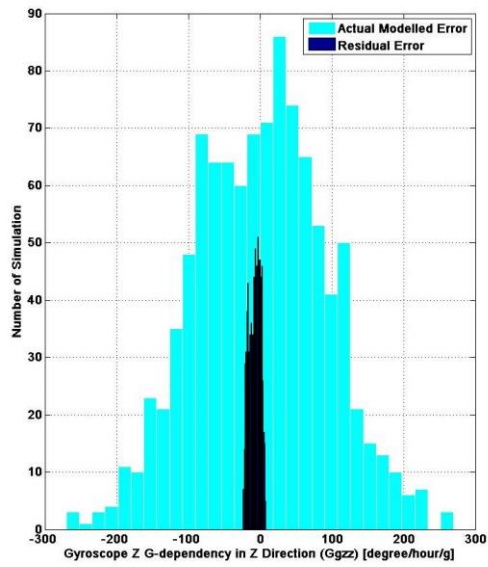
Figure D.7.26 Automotive Grade Gyroscope G$_{gzz}$ Modelled and Residual G-Dependent Bias Error
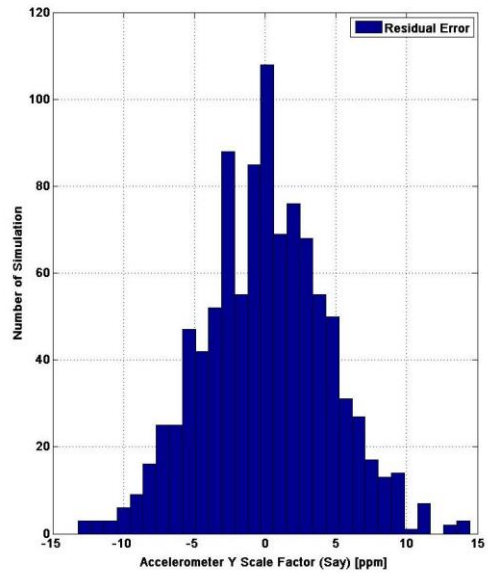
D.2 Tactical Grade

Figure D.7.27 Tactical Grade X Accelerometer Modelled and Residual Bias Error

Figure D.7.28 Tactical Grade Y Accelerometer Modelled and Residual Bias Error
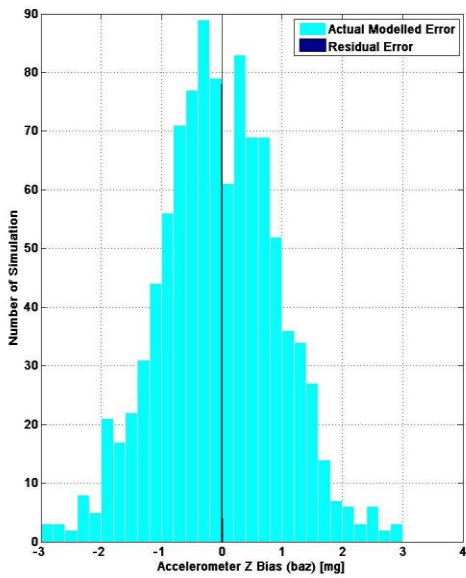
Figure D.7.29 Tactical Grade Z Accelerometer Modelled and Residual Bias Error

127
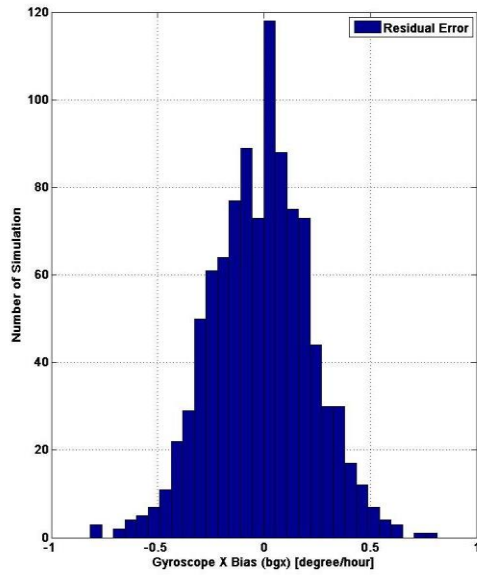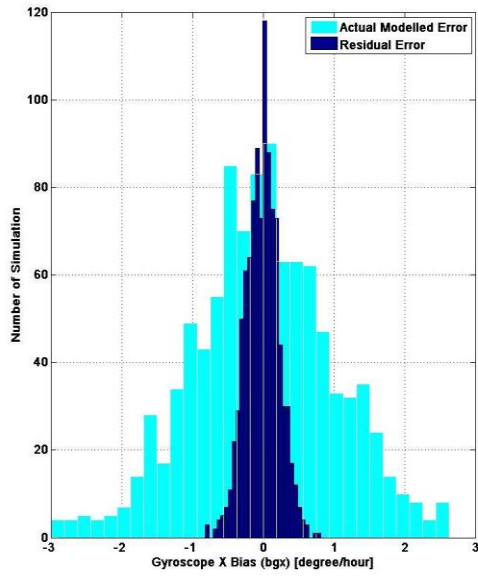
Figure D.7.30 Tactical Grade X Gyroscope Modelled and Residual Bias Error
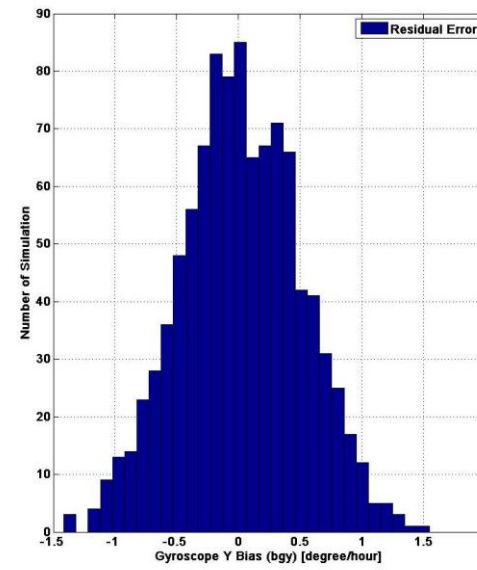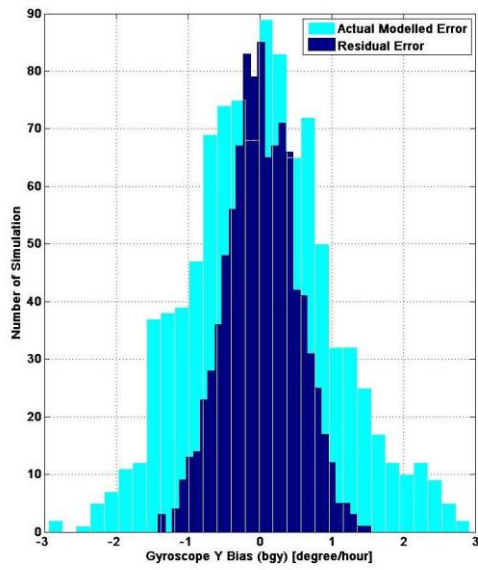
Figure D.7.31 Tactical Grade Y Gyroscope Modelled and Residual Bias Error

128
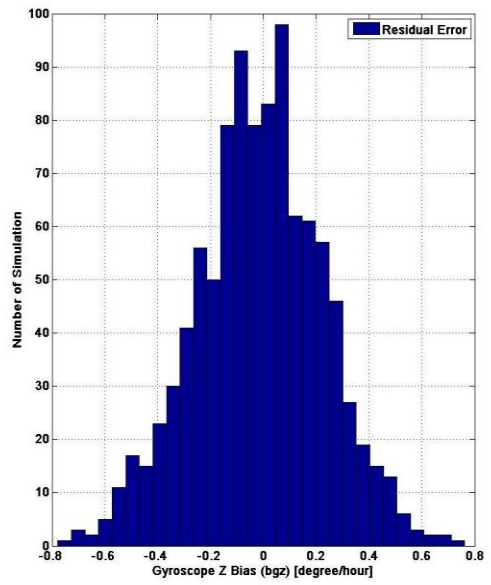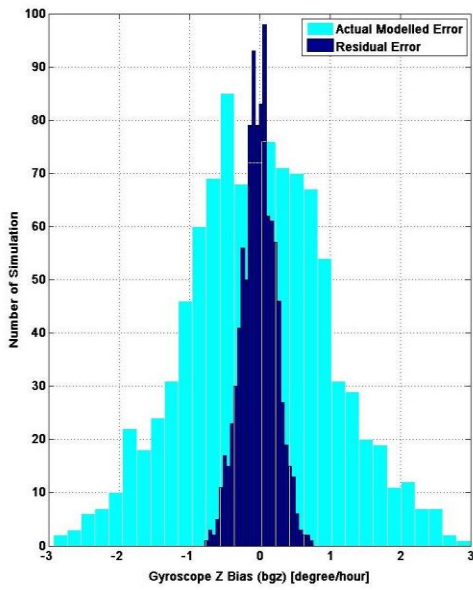
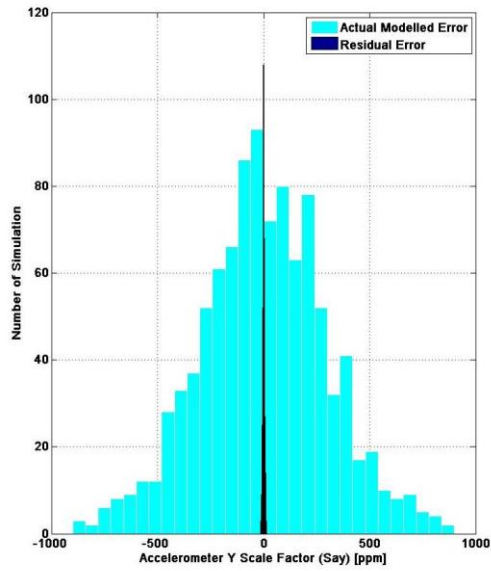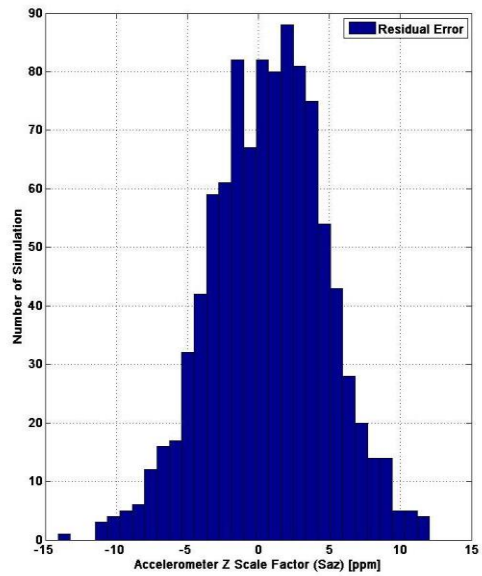**Figure D.7.32 Tactical Grade Z Gyroscope Modelled and Residual Bias Error**
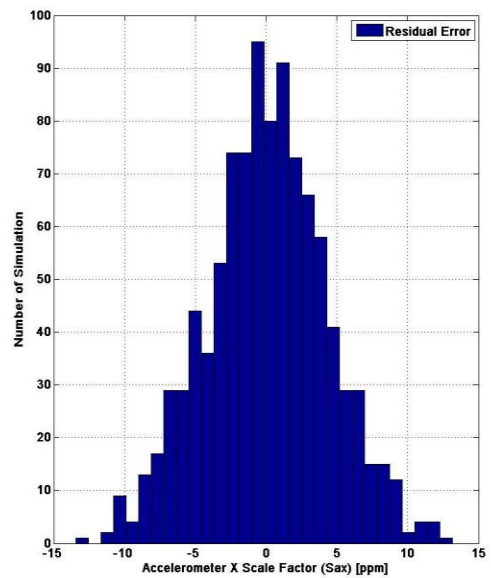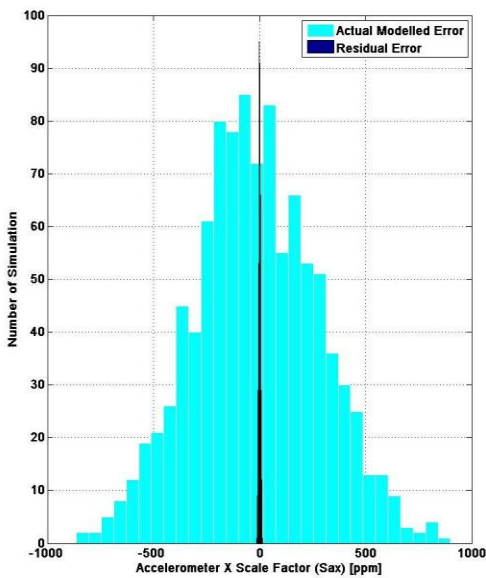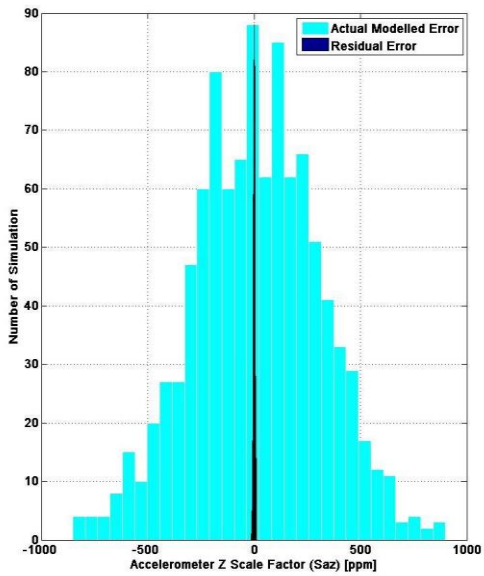

Figure D.7.33 Tactical Grade X Accelerometer Modelled and Residual Scale Factor

Figure D.7.34 Tactical Grade Y Accelerometer Modelled and Residual Scale Factor

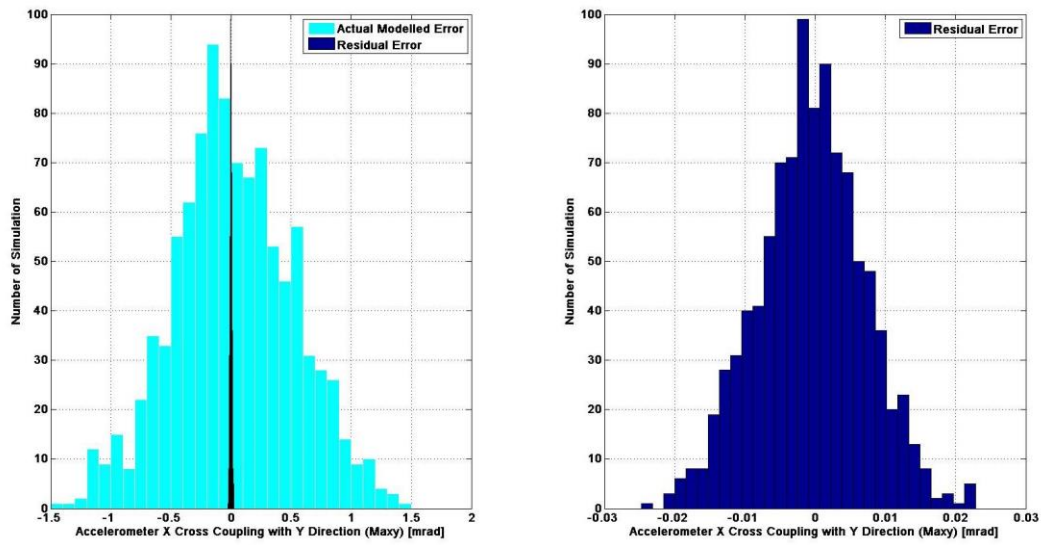**Figure D.7.35 Tactical Grade Z Accelerometer Modelled and Residual Scale Factor**

130

Figure D.7.36 Tactical Grade Accelerometer M$_{axy}$ Modelled and Residual Cross Coupling Error
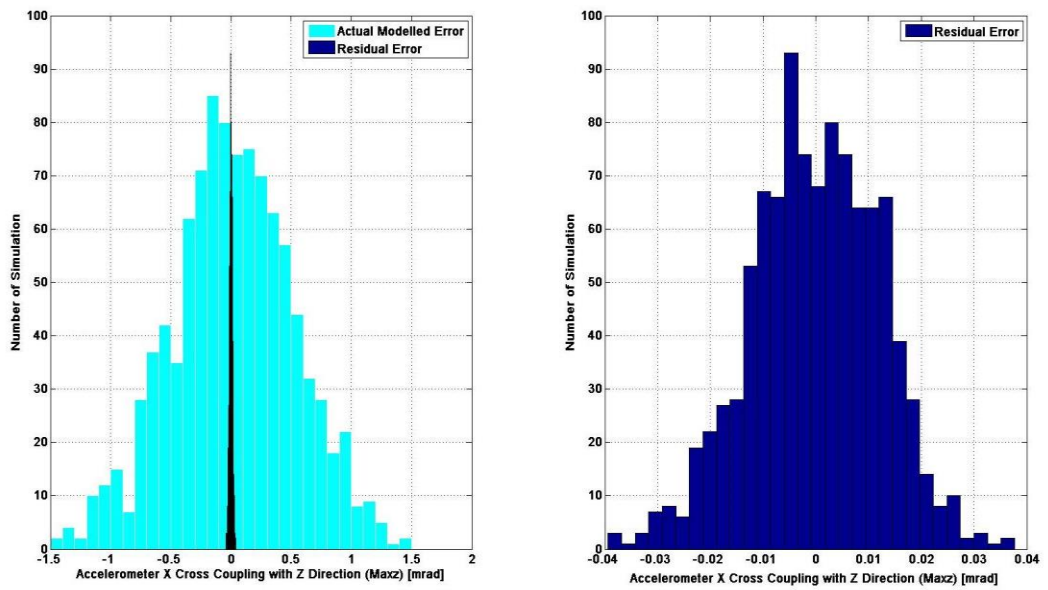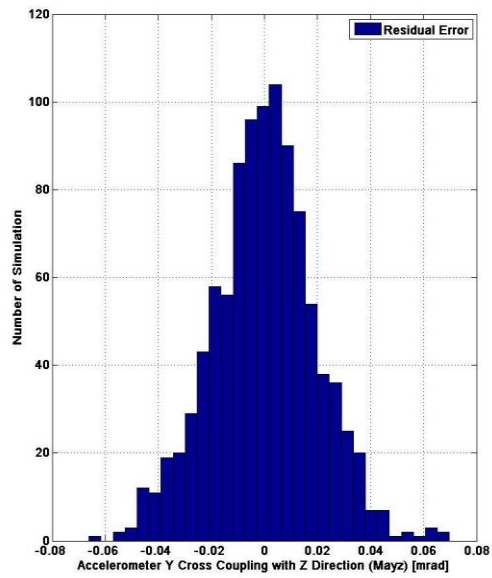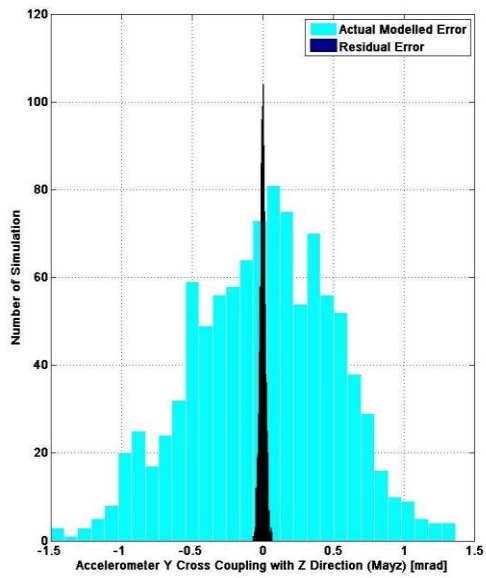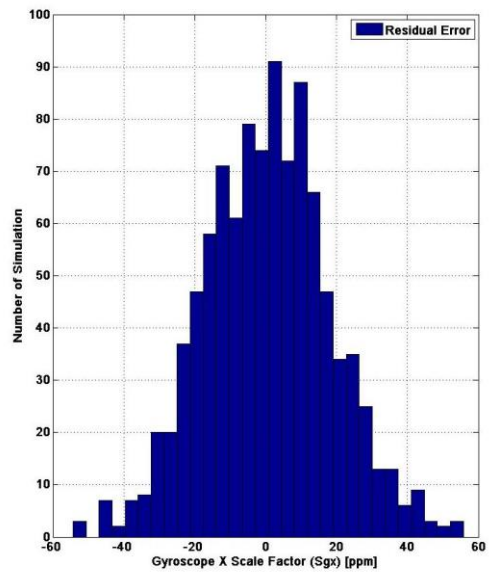

Figure D.7.37 Tactical Grade Accelerometer M$_{axz}$ Modelled and Residual Cross Coupling Error

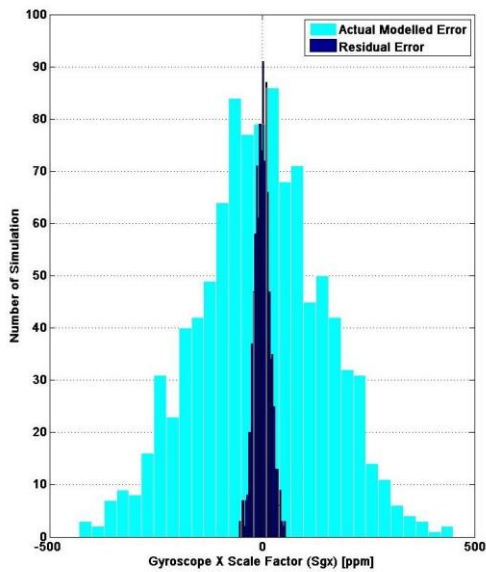**Figure D.7.38 Tactical Grade Accelerometer M_ayz Modelled and Residual Cross Coupling Error**

Figure D.7.39 Tactical Grade X Gyroscope Modelled and Residual Scale Factor
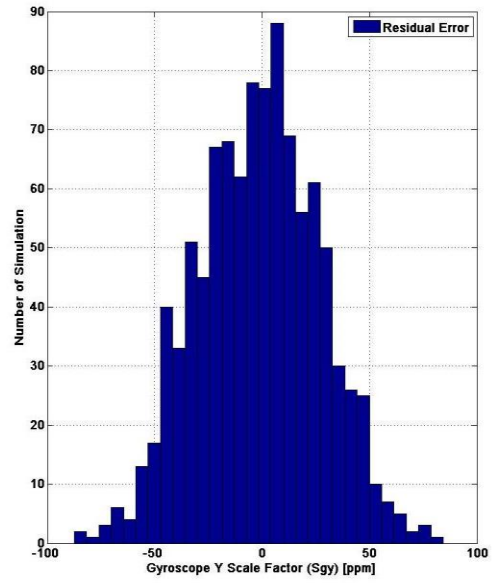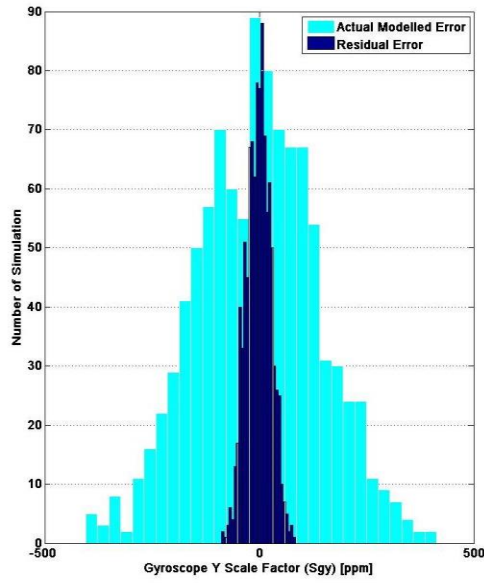
Figure D.7.40 Tactical Grade Y Gyroscope Modelled and Residual Scale Factor
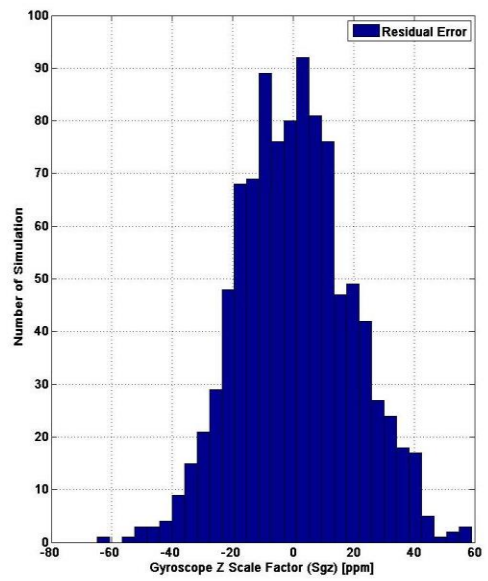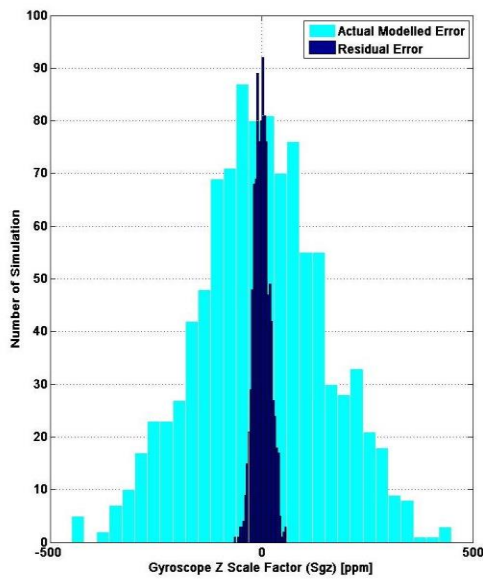
Figure D.7.41 Tactical Grade Z Gyroscope Modelled and Residual Scale Factor

Figure D.7.42 Tactical Grade Gyroscope M$_{gxy}$ Modelled and Residual Cross Coupling Error
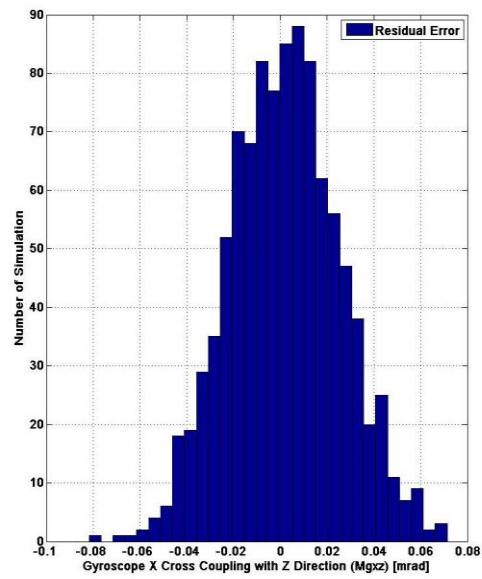
Figure D.7.43 Tactical Grade Gyroscope M$_{gxz}$ Modelled and Residual Cross Coupling Error

Figure D.7.44 Tactical Grade Gyroscope M$_{gyx}$ Modelled and Residual Cross Coupling Error

Figure D.7.45 Tactical Grade Gyroscope M$_{gyz}$ Modelled and Residual Cross Coupling Error

Figure D.7.46 Tactical Grade Gyroscope M$_{gzx}$ Modelled and Residual Cross Coupling Error

Figure D.7.47 Tactical Grade Gyroscope M$_{gzy}$ Modelled and Residual Cross Coupling Error
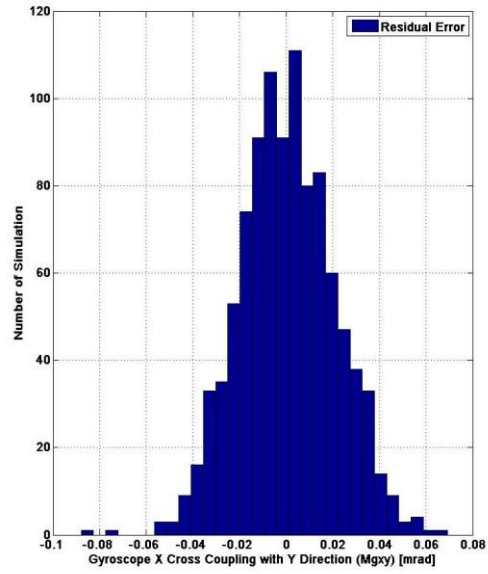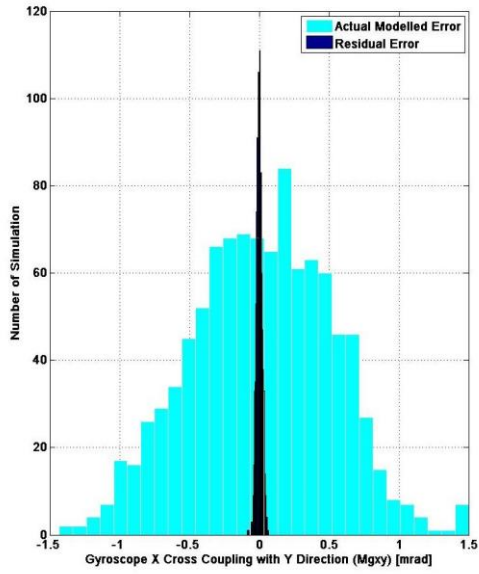
136

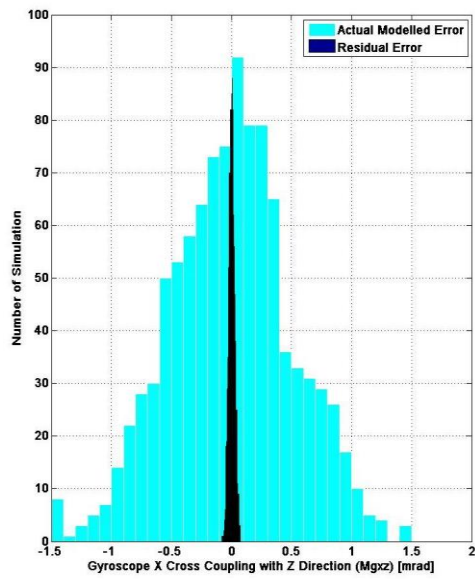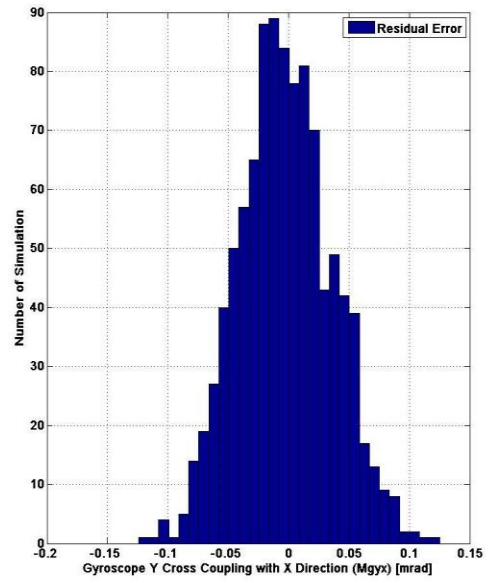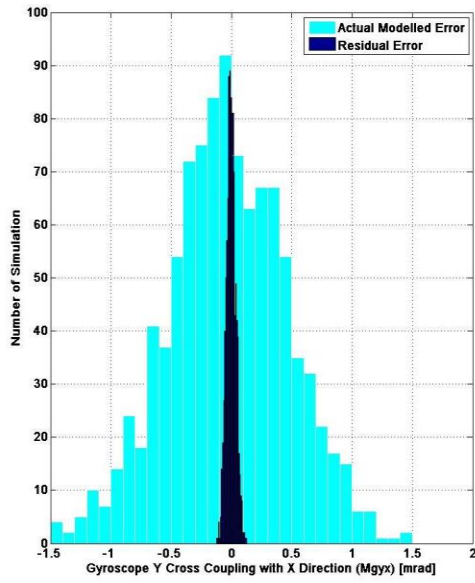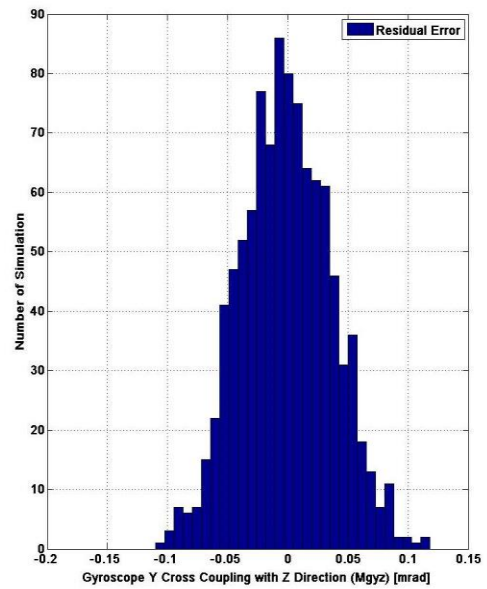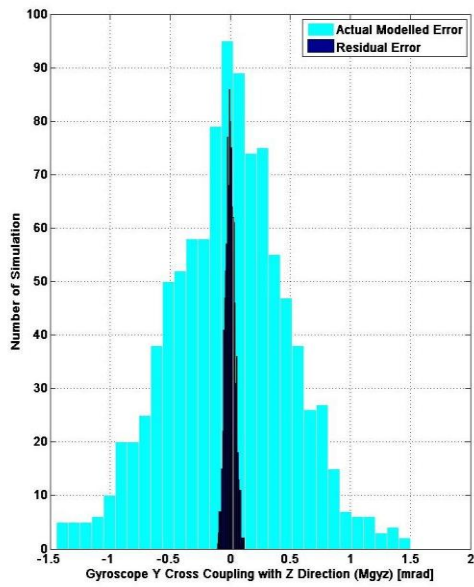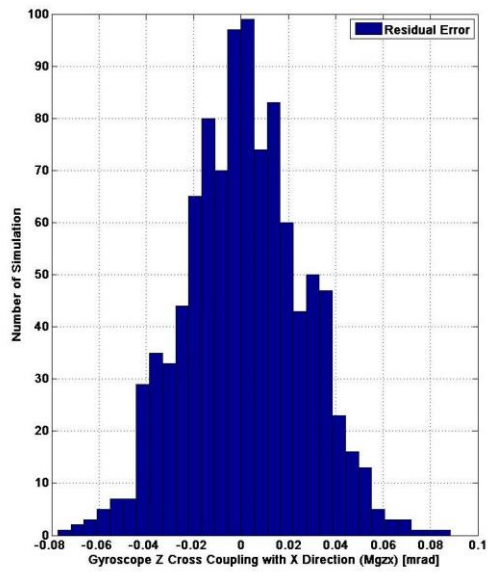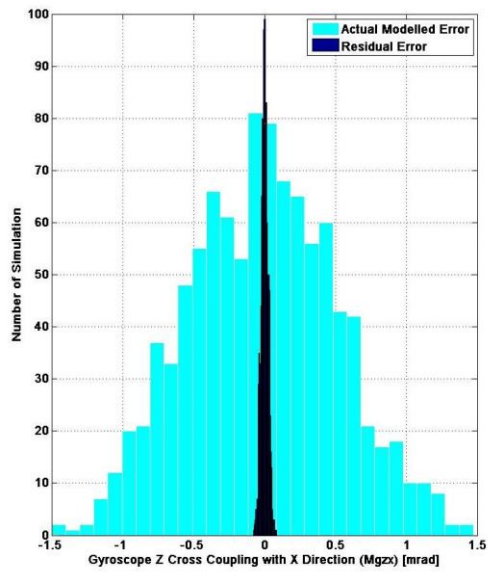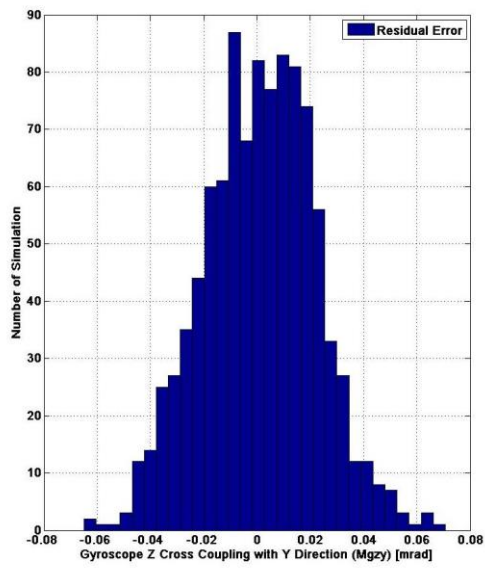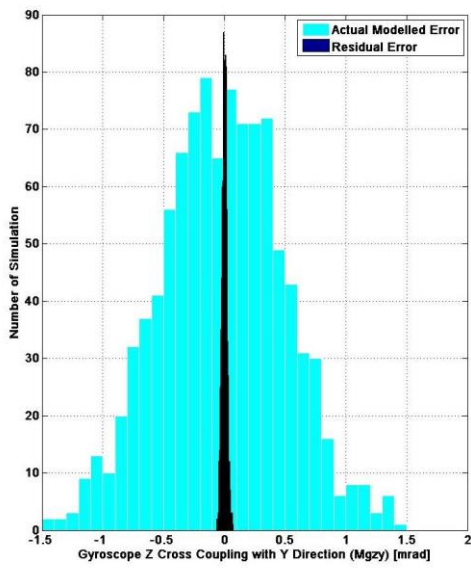# APPENDIX E

HARDWARE SPECIFICATIONS

E.1   Ardupilot MPU-6000

Technical specifications of gyroscopes built-in MPU-6000 given below.

Gyroscope Specifications

VDD = 2.375V-3.46V, VLOGIC (MPU-6050 only) = 1.8V±5% or VDD, T_A = 25°C

PARAMETER	CONDITIONS	MIN	TYP	MAX	UNITS	NOTES
GYROSCOPE SENSITIVITY						
Full-Scale Range	FS_SEL=0		±250		°/s	
	FS_SEL=1		±500		°/s	
	FS_SEL=2		±1000		°/s	
	FS_SEL=3		±2000		°/s	
Gyroscope ADC Word Length			16		bits	
Sensitivity Scale Factor	FS_SEL=0		131		LSB/(°/s)	
	FS_SEL=1		65.5		LSB/(°/s)	
	FS_SEL=2		32.8		LSB/(°/s)	
	FS_SEL=3		16.4		LSB/(°/s)	
Sensitivity Scale Factor Tolerance	25°C	-3		+3	%	
Sensitivity Scale Factor Variation Over Temperature			±2		%	
Nonlinearity	Best fit straight line; 25°C		0.2		%	
Cross-Axis Sensitivity			±2		%	
GYROSCOPE ZERO-RATE OUTPUT (ZRO)						
Initial ZRO Tolerance	25°C		±20		°/s	
ZRO Variation Over Temperature	-40°C to +85°C		±20		°/s	
Power-Supply Sensitivity (1-10Hz)	Sine wave, 100mVpp; VDD=2.5V		0.2		°/s	
Power-Supply Sensitivity (10 - 250Hz)	Sine wave, 100mVpp; VDD=2.5V		0.2		°/s	
Power-Supply Sensitivity (250Hz - 100kHz)	Sine wave, 100mVpp; VDD=2.5V		4		°/s	
Linear Acceleration Sensitivity	Static		0.1		°/s/g	
SELF-TEST RESPONSE						
Relative	Change from factory trim	-14		14	%	1
GYROSCOPE NOISE PERFORMANCE	FS_SEL=0					
Total RMS Noise	DLPFCFG=2 (100Hz)		0.05		°/s-rms	
Low-frequency RMS noise	Bandwidth 1Hz to10Hz		0.033		°/s-rms	
Rate Noise Spectral Density	At 10Hz		0.005		°/s/ √Hz	
GYROSCOPE MECHANICAL FREQUENCIES						
X-Axis		30	33	36	kHz	
Y-Axis		27	30	33	kHz	
Z-Axis		24	27	30	kHz	
LOW PASS FILTER RESPONSE						
	Programmable Range	5		256	Hz	
OUTPUT DATA RATE						
	Programmable	4		8,000	Hz	
GYROSCOPE START-UP TIME	DLPFCFG=0					
ZRO Settling (from power-on)	to ±1°/s of Final		30		ms	

1. Please refer to the following document for further information on Self-Test: *MPU-6000/MPU-6050 Register Map and Descriptions*

Technical specifications of accelerometer built-in MPU-6000 given below.

Accelerometer Specifications

VDD = 2.375V-3.46V, VLOGIC (MPU-6050 only) = 1.8V±5% or VDD, T_A = 25°C

PARAMETER	CONDITIONS	MIN	TYP	MAX	UNITS	NOTES
ACCELEROMETER SENSITIVITY						
Full-Scale Range	AFS_SEL=0		±2		g	
	AFS_SEL=1		±4		g	
	AFS_SEL=2		±8		g	
	AFS_SEL=3		±16		g	
ADC Word Length	Output in two's complement format		16		bits	
Sensitivity Scale Factor	AFS_SEL=0		16,384		LSB/g	
	AFS_SEL=1		8,192		LSB/g	
	AFS_SEL=2		4,096		LSB/g	
	AFS_SEL=3		2,048		LSB/g	
Initial Calibration Tolerance			±3		%	
Sensitivity Change vs. Temperature	AFS_SEL=0, -40°C to +85°C		±0.02		%/°C	
Nonlinearity	Best Fit Straight Line		0.5		%	
Cross-Axis Sensitivity			±2		%	
ZERO-G OUTPUT						
Initial Calibration Tolerance	X and Y axes		±50		mg	1
	Z axis		±80		mg	
Zero-G Level Change vs. Temperature	X and Y axes, 0°C to +70°C		±35			
	Z axis, 0°C to +70°C		±60		mg	
SELF TEST RESPONSE						
Relative	Change from factory trim	-14		14	%	2
NOISE PERFORMANCE						
Power Spectral Density	@10Hz, AFS_SEL=0 & ODR=1kHz		400		µg/√Hz	
LOW PASS FILTER RESPONSE						
	Programmable Range	5		260	Hz	
OUTPUT DATA RATE						
	Programmable Range	4		1,000	Hz	
INTELLIGENCE FUNCTION INCREMENT			32		mg/LSB	

1. Typical zero-g initial calibration tolerance value after MSL3 preconditioning
2. Please refer to the following document for further information on Self-Test: *MPU-6000/MPU-6050 Register Map and Descriptions*

138

E.2   VN-200

Technical specifications of VN-200 given below.

TECHNICAL SPECIFICATIONS

Navigation

Horizontal Position Accuracy:	2.5 m RMS
Horizontal Position Accuracy (w/SBAS):	2.0 m RMS
Vertical Position Accuracy:	5.0 m RMS
Vertical Position Accuracy (w/Barometer):	2.5 m RMS
Velocity Accuracy:	±0.05 m/s
Dynamic Accuracy (Heading, True Inertial):	0.3 ° RMS
Dynamic Accuracy (Pitch/Roll):	0.1 ° RMS
Static Accuracy (Heading, Magnetic)[1]:	2.0 ° RMS
Static Accuracy (Pitch/Roll):	0.5 ° RMS
Angular Resolution:	< 0.05 °
Repeatability:	< 0.1 °
Max Output Rate (IMU Data)[2]:	1 kHz
Max Output Rate (Navigation Data):	400 Hz

Gyro

Range:	±2000 °/s
In-Run Bias Stability:	< 10 °/hr
Linearity:	< 0.1 % FS
Noise Density:	0.0035 °/s /√Hz
Bandwidth:	256 Hz
Alignment Error:	±0.05 °

Accelerometer

Range:	±16 g
In-Run Bias Stability:	<0.04 mg
Linearity:	< 0.5 % FS
Noise Density:	0.14 mg/√Hz
Bandwidth:	260 Hz
Alignment Error:	±0.05 °

Magnetometer

Range:	±2.5 Gauss
Linearity:	< 0.1 %
Noise Density:	140 µGauss/√Hz
Bandwidth:	200 Hz
Alignment Error:	±0.05 °

GPS

Receiver Type:	50 Channels, L1 GPS C/A Code
Solution Update Rate:	5 Hz
Time-to-First-Fix (Cold/Warm Start):	36 s
Time-to-First-Fix (Hot Start):	< 1 s
Altitude Limit:	50,000 m
Velocity Limit:	500 m/s

Pressure Sensor

Range:	10 to 1200 mbar
Resolution:	0.042 mbar
Accuracy:	±1.5 mbar
Error Band:	±2.5 mbar
Bandwidth:	200 Hz

Environment

Operating Temp:	-40°C to +85°C
Storage Temp:	-40°C to +85°C

Electrical:

	SMD	Rugged
Input Voltage:	3.2 V to 5.5 V	3.3 V to 17 V
Current Draw[3]:	105 mA @ 3.3 V	80 mA @ 5 V
Max Power Consumption[3]:	445 mW	500 mW
Digital Interface:	Serial TTL, SPI	Serial TTL, RS-232

Physical:

	SMD	Rugged
Size:	24 x 22 x 3 mm	36 x 33 x 9.5 mm
Weight:	4 g	16 g
Connector:	30-pin LGA	10-pin Harwin
GPS Antenna Connector:	U.FL	MMCX

[1] With proper magnetic declination, suitable magnetic environment and valid hard/soft iron calibration.
[2] Default 800 Hz.
[3] Not including active antenna power consumption.

Figure E.1 VN-200 Technical Specifications

E.3   Mti-710G

Technical specifications of gyroscopes built-in Mti-710G given below.

Gyroscopes

The main difference between the MTi 10-series and the MTi 100-series is the type of gyroscopes used. The two different specifications are listed below. A full range of 1000 º/s is available upon request.

Gyroscopes in MTi 10-series: MTi-10, MTi-20, MTi-30
Gyroscopes in MTi 100-series: MTi-100, MTi-200, MTi-300, MTi-G-700, MTi-G-710

Gyroscope specification		MTi 10-series		MTi 100-series	
Rate of turn		Typical	Max	Typical	Max
Standard full range	[deg/s]	450	-	450	-
Bias repeatability (1yr)	[deg/s]	0.2	0.5	0.2	0.5
In-run bias stability	[deg/h]	18	-	10	-
Bandwidth (-3dB)	[Hz]	415	N/A	415	N/A
Noise density	[deg/s/√Hz]	0.03	0.05	0.01	0.015
g-sensitivity (calibrated)	[deg/s/g]	0.006	0.02	0.003	0.015
Non-orthogonality	[deg]	0.05	-	0.05	-
Non-linearity	[% FS]	0.03	0.1	0.01	-
A/D resolution	[bits]	16	N/A	16	N/A

Technical specifications of accelerometers and magnetometer built-in Mtil-710G given below.

Accelerometers and magnetometer

The MTi 10-series and MTi 100-series use the same accelerometers and magnetometer. The output of the magnetometer is in arbitrary units (a.u.), one a.u. is the magnetic field strength during calibration at Xsens' calibration lab. This is approximately 40 uT. An accelerometer range of 15g is available as well.

Accelerometers/magnetometer: all products: MTi-10, MTi-20, MTi-30, MTi-100, MTi-200, MTi-300, MTi-G-700, MTi-G-710

Accelerometers/magnetometers specification			MTi 10-series and MTi 100-series	
Acceleration			Typical	Max
	Standard full range	[m/s2]	50	-
	Bias repeatability (1 yr)	[m/s2]	0.03	0.05
	In-run bias stability	[µg]	40	-
	Bandwidth (-3dB)	[Hz]	375	N/A
	Noise density	[µg/√Hz]	80	150
	Non-orthogonality	[deg]	0.05	0.05
	Non-linearity	[% FS]	0.03	0.5
	A/D resolution	[bits]	16	N/A
Magnetic field				
	Full range[11]	[µT]	-	80
	Noise density	[µGauss/√Hz]	200	-
	Non-linearity	[% FS]	0.1	-
	A/D resolution	[bits]	12	N/A